Department of Precision and Microsystems Engineering

Optical Leak Test Method For Assessing The Wafer Bond Quality

Ashwinraj Prabhakharan

Report no : 2023.080
Coach : Prof.Dr.P.G.Steeneken, Dr. Joost van Beek, Gerard Rietjens, Richard Pleeging
Professor : Prof.Dr.P.G.Steeneken
Specialisation : Dynamics of Micro and Nanosystems
Type of report : MSc Thesis Report
Date : 28-09-2023

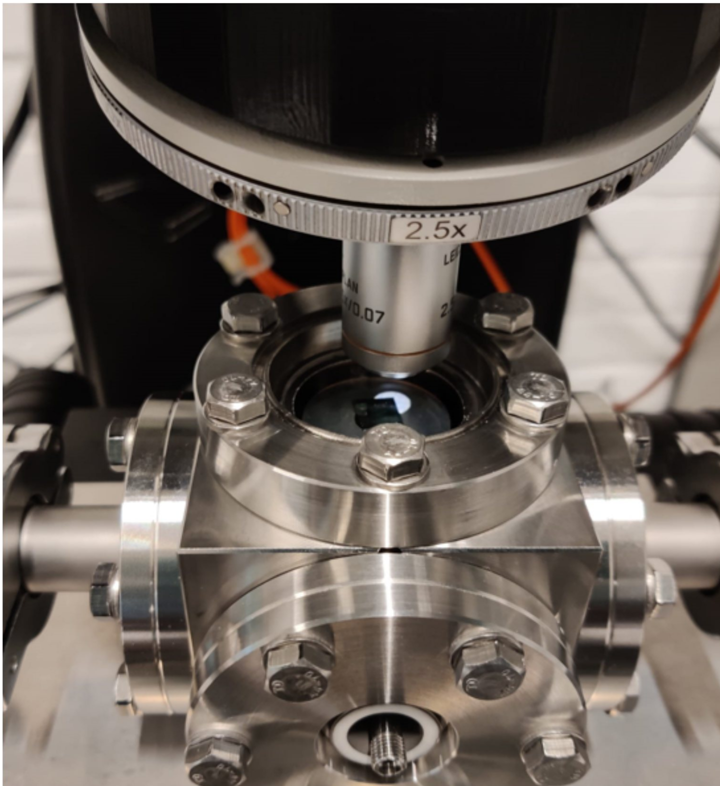

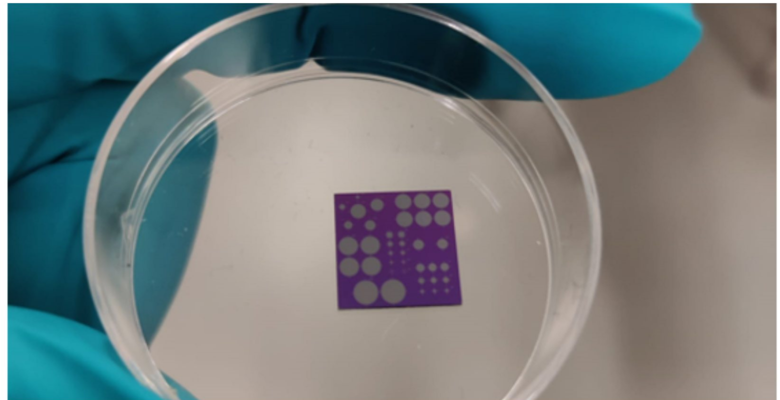

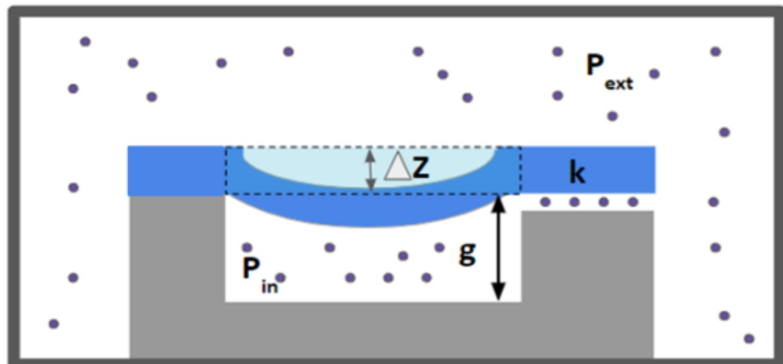

TU Delft
Delft University of Technology

Challenge the future

Thesis Report

Optical Leak Test Method for Hermiticity Testing of Wafer Bonds

by

Ashwinraj Prabhakharan

to obtain the degree of Master of Science
at the Delft University of Technology,
to be defended publicly on Thursday September 28, 2023 at 12:30.

Student number:	5352533	
Project duration:	July 1, 2022 – September 28, 2023	
Thesis committee:	Prof. Dr. P.G. Steeneken ,	PME TU Delft, Supervisor
	Ir.Richard Pleeging,	Philips, Supervisor
	Dr. Richard Norte,	PME TU Delft

This thesis is confidential and cannot be made public until September 2024.

Preface

This thesis represents my one year of work for the MSc project titled ”Optical leak test method for assessing the wafer bond quality”. This work is done in the dynamics of the microsystems engineering (DMN) group of the PME department in collaboration with Philips MEMS and Micro Devices group. During this year, I developed a method using an optical interferometer setup to accurately measure the leak rate of gas permeating through silicon-silicon fusion bonded wafers, which eventually helps to assess the bond quality as part of the in-line testing process. Many people have helped me during my thesis, without whom this project would not have been possible.

I would like to express my gratitude to my supervisors, Peter Steeneken from TU Delft, Joost van Beek, Gerard Rietjens, and Richard Pleeging from Philips, for their invaluable assistance and support throughout this research project. Peter and Joost were the initial people who offered this interesting idea to me. Despite his busy schedule, Peter constantly allocated time to assist me in various aspects of the project. Additionally, his enthusiasm and positivity served as a catalyst for maintaining my motivation at maximum. The early meetings with Joost proved to be beneficial in formulating strategic action plans for the project. Gerard played a pivotal role in the fabrication of the test samples. Until the final phase of the project, he provided significant assistance in the fabrication of new samples, contributing to the acquisition of significant findings. Richard, an alumnus of TU Delft, provided valuable insights into the project from the company's perspective and meticulously scrutinized each section of my report to address intricate aspects. I extend my thanks to the Lab support team of the PME department for their invaluable assistance in training me with lab equipment available in the optics lab and providing me necessary components that enabled the smooth construction and operation of my experimental setup.

Finally, I would like to express my heartfelt gratitude to my parents in India, for their unconditional emotional support and love throughout this journey. Their encouragement has been invaluable, providing me with the strength and motivation to pursue my studies and research.

Ashwinraj Prabhakharan
Delft, September 2023

Abstract

Hermeticity is a measure of how well a package is leak-tight. Many Micro-Electro-Mechanical Systems (MEMS) sensors, actuators, and microelectronic devices need a defined cavity environment for optimal performance, hence measuring the package leak rate is critical for lifetime prediction. MEMS devices are generally packaged through the wafer-bonding technique. The MEMS device is produced on a wafer with a cavity and bonded to a cap wafer to seal the cavity. Reducing the cap wafer thickness allows it to deflect due to the cavity interior-exterior pressure differential. Consequently, if leakage occurs, the deflection will change. By measuring these deflections, it is possible to quantify leak rates.

In order to use it as an in-line testing process, this research aims to determine the accuracy of the deflection method for determining the leak rates. To achieve this, our approach involved designing and leak testing test structures (or devices) using an experimental setup that can vary pressure, supply desired species inside a vacuum chamber, and measure deflection using an interferometer to determine leak rates. Deflections are converted to leak rates using a formulated analytical expression, which is subsequently utilized to determine the error involved in measuring leak rates.

Using the experimental setup, the test devices were effectively characterized for sensitivity using pressure-induced deflection measurements, with experimental sensitivity values closely matching the theory. Further, air leak testing was performed on devices interconnected with nanometer-gap size leak channels to gain first-hand knowledge of leakage. Experimental leak rates matched well with analytical models, proving that flow through devices having leak channels can be characterized. Ultimately, the setup enabled successful helium leak testing of devices without any defined leak channels.

The helium leak-tested samples were circular membranes of diameters: 2000, 1600, 1400, 1300, and 1100 µm with a thickness of 40 µm bonded to a cavity depth of 3.24 µm. Uncertainty analysis associated with leak rate measurement revealed that when considering a certain cavity depth and membrane thickness, the membrane with the largest diameter would exhibit the least amount of uncertainty. This was also observed through experiments, for the diameter of 2000 µm, a clear linear trend of deflection reduction due to the helium leakage was observed during a two-week period of deflection measurements. Whereas, for the diameter of 1100 µm, it was not possible to observe the same linear trend of deflection reduction, indicating that even more no.of.days is required to determine an accurate leak rate.

In the end, a short analysis was made using the cavity design having the 2000 µm membrane, which had the least uncertainty in measuring the leak rate. This analysis aimed to ascertain the designed test structure's usefulness in measuring leak rates of the MEMS packages. Based on the analysis, it was concluded that large-volume wafer-bonded MEMS packages (> 1 mm3) with an acceptable cavity pressure increase of 10 mbar could be tested using the deflection method and our proposed test structure design to guarantee their lifetime.

Contents

Preface i

Abstract ii

1 Introduction 1

2 Literature Review 3
- 2.1 Silicon Fusion Bonding . . . 3
- 2.2 Types of Leak . . . 5
- 2.3 Hermiticity Test Methods . . . 8
- 2.4 Studies Conducted Using Hermiticity Test Methods . . . 12
- 2.5 Discussion . . . 16
- 2.6 Research Question . . . 18
- 2.7 Planning for design, fabrication and experiments . . . 18

3 Test Structure Design 20
- 3.1 Test Structure . . . 20
- 3.2 Selection of Test Structure . . . 22
- 3.3 Size Dependent Analysis . . . 24
- 3.4 Prediction of Plastic deformation . . . 26
- 3.5 Collapsing of membrane . . . 32

4 Experimental Method 33
- 4.1 Digital Holographic Microscope . . . 33
- 4.2 Steps for deflection measurement . . . 35
- 4.3 Errors in deflection measurement . . . 45
- 4.4 Experimental Setup . . . 55
- 4.5 Experimental Procedure . . . 56
- 4.6 Fabrication of test samples . . . 57
- 4.7 Uncertainty in fabricated test samples . . . 60
- 4.8 Estimation of uncertainty in measuring leak rate . . . 64

5 Results and Discussion 66
- 5.1 Pressure-Deflection Characterization . . . 66
- 5.2 Plastic Deformation . . . 69
- 5.3 Leak testing of cavities with channels . . . 73
- 5.4 Leak testing of sealed-off cavities . . . 82

6 Conclusion 89

7 Recommendation 91

References 96

A Uncertainty in measured diameters of membranes 100

B Pressure-deflection measurements for random error estimation 101

C Source code for actual deflection calculation 103

D Reliability checking of pressure controller and readout 108

E Measurement of deflections for outgassing and air leakage 111

List of Figures

1.1 Illustration of wafer-level packaging [4] 2

2.1 Steps involved in the fusion bonding process [5] 3
2.2 Illustration of voids or gap formation at the bond interface due to surface waviness and roughness 4
2.3 Schematic representation of void or gap formed due to A) rough and wavy contacting surfaces B) particle at the bond interface [6] 6
2.4 Steps in helium leak test [13] 8
2.5 Schematic representation of transmittance measurement used in FTIR [17] 9
2.6 Illustration of cap deflection due to leak 10
2.7 Frequency response as a function of pressure difference [23] 11
2.8 Schematic representation of resonator embedded inside the cavity [3] 11
2.9 Schematic representation of the implantable device [25] 12
2.10 Structure of adhesive bonded test vehicle[29] 13
2.11 Representation of encapsulated Pirani tube [30] 14
2.12 Package with laterally extended silicon nitride sealing-layer[31] 14
2.13 Optical image of graphene suspended device after sealing[22] 14
2.14 Schematics of the interferometer setup used for measuring resonance frequency [22] 15
2.15 Plot of leak rates obtained using different hermeticity test methods 17
2.16 Illustration showing the leak pathways through which gas can leak 17

3.1 Illustration of leaking bonded wafers along with indicated critical parameters. Downward deflection is considered as positive 20
3.2 2D Axisymmetric model created in the simulations for membrane having a radius of 350 μm 26
3.3 E<ijk> along the <100>-, <110>- and <111>-crystallographic directions for three Si samples measured by Vanhellemont et al.[38] 28
3.4 Quad mesh for the geometrical model having a radius of 350μm 29
3.5 Distribution of von-mises stress (in Mpa) when the membrane diameter is 1900 μm 30
3.6 Temperature dependence of maximum and flow stress in silicon [39] 31
3.7 Plot of maximum von-mises stress as a function of membrane diameter (comparison of maximum von-mises stress with yield strength) 31
3.8 Illustration of a collapsing membrane with substrate base when deflection > gap height . . . 32

4.1 Basic optical configuration of DHM in reflection geometry to measure height profiles [48] . 33
4.2 Lyncée Tec DHM 34
4.3 Main window of Koala 35
4.4 Menu bar of Koala 35
4.5 Koala status bar 36
4.6 Open configuration menu 36
4.7 Hologram image of a membrane having a diameter of 2000μm 36
4.8 Intensity image when the focus is very less 37
4.9 Intensity image with a maximum focus 37
4.10 Principle of phase measurement in DHM 38
4.11 Reference Planes XYZ of the DHM and of the sample 39
4.12 Phase window, when the sample is not coplanar with the reference plane of microscope . . 39
4.13 Phase window, when the sample is coplanar with the reference plane of microscope 40
4.14 Phase window with phase offset defined 40
4.15 Wrapped phase image and corresponding 1D profile 41
4.16 Unwrapped phase image and corresponding 1D profile 41

4.17 3D profile of deflected sample having a diameter of 2000 μm . . . 42
4.18 Working scheme of the MATLAB code to extract the actual deflection . . . 42
4.19 Selected region of interest for deflected surface . . . 43
4.20 Comparison of measured and fitted deflected surface . . . 43
4.21 Selected region of interest for flat surface . . . 44
4.22 Comparison of measured and fitted flat surface . . . 44
4.23 Fringe pattern in hologram . . . 45
4.24 Low histogram contrast . . . 45
4.25 (A) Intensity image (B) Phase image, when the hologram histogram contrast is at minimum 46
4.26 Deflection profile due to low-intensity contrast . . . 46
4.27 Hologram histogram contrast at 100 . . . 46
4.28 (A) Intensity image (B) Phase image, when the hologram histogram contrast is 100 . . . 47
4.29 Deflection profile, when the hologram histogram contrast is 100 . . . 47
4.30 Hologram histogram contrast at 450 . . . 47
4.31 (A) Intensity image (B) Phase image, when the hologram histogram contrast is 450 . . . 48
4.32 Deflection profile, when the hologram histogram contrast is 450 . . . 48
4.33 (A) Phase image when the drawn tilt correction segment is small (B) Deflection profile for the corresponding phase image . . . 49
4.34 (A) Phase image when only one tilt correction segment is drawn (B) Deflection profile for the corresponding phase image . . . 49
4.35 (A) Phase image when 2 orthogonal segments are drawn around the flat surface (B) Deflection profile for the corresponding phase image . . . 50
4.36 (A) Phase image when 4 orthogonal segments are drawn around the (B) Deflection profile for the corresponding phase image . . . 50
4.37 Phase image of 900 μm diameter of membrane with ROI of 800x800 pixels . . . 51
4.38 3D profile of membrane with unwrapping issue at the edges . . . 51
4.39 Approximation of flat surface with unwrapping issue . . . 52
4.40 Phase image of 900 μm diameter of membrane with ROI of 400x400 pixels . . . 52
4.41 3D profile of membrane with flat surfaces along the edges . . . 53
4.42 Approximation of flat surface with smaller ROI . . . 53
4.43 3D profile of membrane having flipped surfaces along the edges . . . 54
4.44 Approximation of flat surface with edge detection issue . . . 54
4.45 Illustration of hermiticity test setup . . . 55
4.46 Experimental setup with labels indicating the major components . . . 55
4.47 Sample setting window . . . 56
4.48 Illustration of the wafer bonded cavities with defined leak channel . . . 57
4.49 Process flow for fabricating silicon membranes with sealed cavity . . . 58
4.50 Process flow for fabricating silicon membranes with cavities having leak channels . . . 58
4.51 Mask layout design for membranes and cavities (Dimensions in μm) . . . 59
4.52 Mask layout design for leak channels (Width dimensions in μm) . . . 59
4.53 (A) Automated cavity depths measurements were performed along the line on the wafer (B) Markers drawn for measuring the bottom of the cavity and flat surface . . . 60
4.54 Variations in cavity depth among the measured 17 dies (wafer with deep cavity depth) . . . 60
4.55 Thickness measurement of a membrane from test cavity-1 . . . 61
4.56 Thickness measurement of a membrane from test cavity-2 . . . 61
4.57 SEM images of leak channel having wedges along the walls . . . 62
4.58 SEM images of leak channel having a rough bottom surface . . . 62
4.59 Diameter images made using the Keyeence digital microscope for diameters: 2000, 1600, and 1400 μm . . . 63
4.60 Diameter images made using the Keyeence digital microscope for diameters: 1300, 1100, and 900 μm . . . 63

5.1 Measured and fit pressure-deflection curve for 2000 μm drum . . . 66
5.2 Deflection profile of 500μm membrane for external pressure varying from 1000 mbar to 100 mbar . . . 67
5.3 Improperly obtained pressure-deflection curve for 500μm membrane . . . 67

5.4 Deflection profile of 700μm membrane for external pressure varying from 1000 mbar to 100 mbar . . . 68
5.5 Measured and fit pressure-deflection curve for 700 μm drum . . . 68
5.6 Comparison of experimental and analytical pressure-deflection sensitivity using eq.5.2 The used parameters for the analytical equation are: E<100> = 128 Gpa, γ=0.28 and thickness = 40 μm . . . 69
5.7 Pressure-deflection curve of the membrane having diameter 2000 μm . . . 69
5.8 Pressure-deflection curve of the membrane having diameter 1300 μm . . . 69
5.9 Pressure-deflection curve of the membrane having diameter 700 μm . . . 70
5.10 Deflection profile of 2000 μm diameter membrane before and after leakage . . . 70
5.11 Deflection profile of 1600 μm diameter membrane before and after leakage . . . 71
5.12 Deflection profile of 1400 μm diameter membrane before and after leakage . . . 71
5.13 Deflection profile of 1100 μm diameter membrane before and after leakage . . . 71
5.14 Deflection profile of 900 μm diameter membrane before and after leakage . . . 72
5.15 Hole generation on the membrane to open the cavity to atmospheric pressure . . . 73
5.16 Reduction of membrane deflection due to immediate ingress of air molecules into the leak channel . . . 74
5.17 Evacuation of vacuum chamber . . . 74
5.18 Venting of the vacuum chamber and measurement of reducing deflection . . . 74
5.19 Numbers allotted for all membranes in die and red cross indicates the membranes indicates where holes are created
Dimensions of the leak channels can be verified from Fig.4.51 and 4.52 . . . 75
5.20 Deflection measurements of 2000 μm diameter membrane . . . 76
5.21 Deflection measurements of 1400 μm diameter membranes . . . 76
5.22 Deflection measurements of 1600 μm diameter membranes . . . 77
5.23 Illustration of molecules striking the surfaces of the channel and exhibiting the specular reflection [57] . . . 78
5.24 Leak rate calculated from the continuum, slip, free-molecular equations and leak rate calculated from deflection measurements are plotted against the pressure-difference, which is calculated based on deflection measurements obtained for leak channel size of W:100μm x L:200 μm x H:34nm . . . 79
5.25 Leak rate calculated from the continuum, slip, free-molecular equations and leak rate calculated from deflection measurements are plotted against the pressure-difference, which is calculated based on deflection measurements obtained for leak channel size of W:1μm x L:200 μm x H:34nm . . . 80
5.26 Leak rate calculated from the continuum, slip, free-molecular equations and leak rate calculated from deflection measurements are plotted against the pressure-difference, which is calculated based on deflection measurements obtained for leak channel size of W:0.5μm x L:200 μm x H:34nm . . . 81
5.27 Leak rate calculated from the continuum, slip, free-molecular equations and leak rate calculated from deflection measurements are plotted against the pressure-difference, which is calculated based on deflection measurements obtained for leak channel size of (A) W:1μm x L:862.74 μm x H:34nm (B) W:1μm x L:945.58 μm x H:34nm . . . 81
5.28 Keyeence microscope image of the tested die and the measured diameters in the die are indicated by blue cross mark . . . 83
5.29 Deflection measurements of 2000 μm and 1600 μm diameter membrane under helium gas pressure . . . 83
5.30 Deflection measurements of 1400 μm and 1300 μm membrane under helium gas pressure . 83
5.31 Deflection measurements of 1100 μm membrane under helium gas pressure . . . 84
5.32 Linear fitting of deflection data points for 2000 μm and 1600 μm diameter membranes . . . 84
5.33 Linear fitting of deflection data points for 1400 μm and 1300 μm membrane . . . 85
5.34 Linear fitting of deflection data points for 1100 μm membrane . . . 85
5.35 (A) Plot of leak rate against diameter (B) Plot of leak rate against diameter^2 . . . 86

7.1 Existing process flow . . . 94
7.2 Mask layout of membranes fabricated using existing process flow . . . 94

7.3 FIB-SEM image of membrane cross section 94
7.4 Pressure-deflection curve of the membrane having dimension of 2000 x 1500 (in um) 95
7.5 Pressure-deflection curve of the membrane having dimension of 1900 x 1400 (in um) 95
7.6 Pressure-deflection curve of the membrane having dimension of 1950 x 1450 (in um) 95

C.1 Oxide thickness at point-1 105
C.2 Oxide thickness at point-2 105

D.1 Experimental setup attached with manometer for testing the accuracy of pressure controller 109

List of Tables

2.1 Effects of contamination on bonding quality 4

3.1 Values of α for different aspect ratios 23
3.2 Deflection rate expressions for circular-square-rectangular plates in the dZ/dN form 23
3.3 Design parameters 24
3.4 Calculated area (A) for considered diameters 24
3.5 Calculated value of stiffness (in N/µm) for different diameter and thickness values 25
3.6 Deflection (Z) of the membrane (in µm) at atmospheric pressure of 1 atm 25
3.7 dN_{in}/dZ for gap height - 10um 25
3.8 dN_{in}/dZ for gap height - 100um 25
3.9 dN_{in}/dZ for gap height - 250um 25
3.10 dN_{in}/dZ for gap height - 450um 25
3.11 Material properties at each annealing temperature 28
3.12 Deflection of membranes (in nm) at 1 atm external pressure - Thickness 40 µm 32

4.1 DHM objective lens details 34
4.2 Components used in Fig.4.46 55
4.3 Estimation of uncertainty in leak rate (mol/sec) for membrane with a thickness of 40 µm and cavity with gap height of 3.24 µm 65

5.1 Calculated helium leak rates for membranes and uncertainty involved in measuring leak rates 85
5.2 Time required to measure leak rate of MEMS package with package volume of 0.01 mm^3, with the requirement of 0.1 mbar change over the lifetime of 10 years 87
5.3 Time required to measure leak rate of MEMS package with package volume of 0.01 mm^3, with the requirement of 10 mbar change over the lifetime of 10 years 88
5.4 Time required to measure leak rate of MEMS package with package volume of 1 mm^3, with the requirement of 10 mbar change over the lifetime of 10 years 88
5.5 Time required to measure leak rate of MEMS package with package volume of 2 mm^3, with the requirement of 10 mbar change over the lifetime of 10 years 88

7.1 Time required to measure the leak rate of 1×10^{-20} by considering device design with a membrane diameter of 3000 µm and a thickness of 40 µm. 91
7.2 Time required to measure the leak rate of 1×10^{-20} by considering device design with a membrane diameter of 3000 µm and a thickness of 10 µm 92
7.3 Time required to measure the leak rate of 1×10^{-20} by considering device design with a membrane diameter of 1000 µm and a thickness of 10 µm 92
7.4 Time required to measure the leak rate of 1×10^{-20} by considering device design with a membrane diameter of 100 µm and a thickness of 1 µm 93

A.1 Uncertainty in measured diameters 100

B.1 Pressure-deflection measurements obtained from day-1 to day-8 for membrane diameter: **2000 µm** 101
B.2 Pressure-deflection measurements obtained from day-1 to day-8 for membrane **diameter: 1600 µm** 101
B.3 Pressure-deflection measurements obtained from day-1 to day-8 for membrane **diameter: 1400 µm** 102
B.4 Pressure-deflection measurements obtained from day-1 to day-8 for membrane **diameter: 1300 µm** 102

B.5 Pressure-deflection measurements obtained from day-1 to day-8 for membrane **diameter: 1100 µm** . . . 102

D.1 Comparison of readout from pressure regulator and manometer . . . 109
D.2 Uncertainty in pressure values . . . 110

E.1 Deflection of membranes - 2000 µm . . . 111
E.2 Deflection of membranes - 1600 µm . . . 111
E.3 Deflection of membranes (in nm) under atmospheric pressure - for 1400 µm . . . 111
E.4 Deflection of membranes (in nm) under atmospheric pressure - for 1300 µm . . . 111
E.5 Deflection of membranes (in nm) under atmospheric pressure - for 1100 µm . . . 111

1

Introduction

Leak detection of small semiconductors, integrated circuits (IC), and microelectronic packages started in the 1960s when it was observed that corrosion of devices occurred when the moisture level inside the package cavity exceeded 5000 ppm [1]. The helium leak test was first used to determine the leak rate of the packages. The test involves placing the package in a pressurized helium gas for a specific time, then measuring the number of gas molecules leaking out of the package in a vacuum chamber using a helium mass spectrometer.

In those days, the typical cavity volume was 0.1 cm^3 and the helium leak rate of 2.25x10^{-14} mol.sec^{-1} ensured that no more than 5000 ppm moisture would ingress into the cavity over the expected lifetime of 8 years [2]. Mass spectrometry at that time permitted the detection of leak rates between 1x10^{-11} and 1x10^{-13} mol.sec^{-1}. To allow the usage of this test method, it was agreed that the maximum permissible leak rate of the package should be beyond the detectable range of the helium mass spectrometer [2]. This was the beginning of a series of concerns regarding the determination of the package leak rates.

The main objective of a traditional IC, semiconductor, or microelectronic package is to keep moisture out of the package. Reducing water content reduces the mobility of corrosive contaminants and thereby increases the mean time to failure. In this regard, micro-electro-mechanical systems (MEMS) packages must not only prevent moisture ingress but also prevent interaction with the external environment to enable the MEMS to act as a potential sensor or actuator. MEMS sensors or actuators typically have moving parts that can be extremely sensitive to the environmental gas pressure during operation. For instance, the sensitivity or quality (Q) factor of MEMS gyroscopes decreases as the pressure in the package increases. Another example is MEMS infrared sensors, which must operate in a pressure $<10^{-3}$ mbar to be thermally isolated from the outside environment and maintain adequate sensitivity. For these reasons, MEMS devices often need to be packaged in a vacuum for proper operation.

MEMS devices are generally wafer-level bonded to ensure as hermetic a package as possible. A typical MEMS package has a volume of 0.1 mm^3, a sealed cavity pressure of 10^{-2} atm, a lifetime of 5 years, and an acceptable pressure increase over this lifetime of 10%. Using the definition of the leak rate of L, as represented by eq.1.1 [3], the maximum acceptable leak rate of this package is 6.34x10^{-16} atm.cm^3.sec^{-1} (2.82 x 10^{-20} mol.sec^{-1}). This leak rate is several orders of magnitude lower than the minimum detectable leak rate of the traditional hermiticity test method.

$$L = \frac{\Delta PV}{t} \tag{1.1}$$

Where Δ P is the maximum acceptable change in cavity pressure over the device lifetime, V is the volume of the cavity and t is the device lifetime.

In the concept of wafer-level packaging, MEMS devices are first fabricated on a silicon wafer, and the MEMS wafer is then bonded to a cap wafer that has cavities to create a sealed enclosure. Finally, dicing the bonded wafer yields many packaged chips which are then subjected to final-level packaging with the plastic-molding process. An illustration of the steps involved in wafer-level packaging is shown in Fig.1.1.

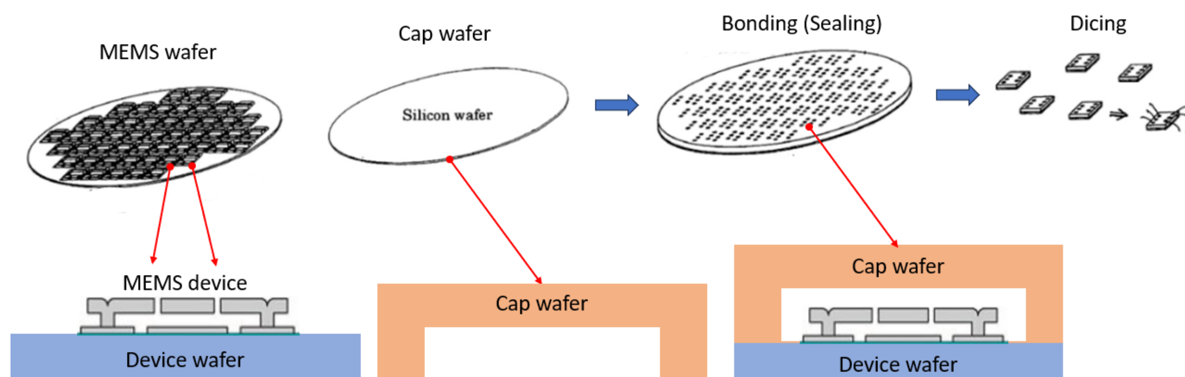

Figure 1.1: Illustration of wafer-level packaging [4]

By reducing the thickness of the cap wafer, the cap can be made to deflect due to the difference in pressure between inside the cavity and the outside atmosphere. This deflection response can be utilized for assessing the hermicity of a wafer-bonded cavity. If a cavity is hermetically sealed, the cap deflects to the inside of the cavity, or else becomes flat indicating zero pressure difference due to leak. To apply this phenomenon for quantitative measurement of the leak rate, a controlled structure is needed for the capping layer and cavity that exhibits a measurable deflection.

From the application point of view, the controlled structure could be used as a process control monitor (PCM) test structure on bonded wafers to test the bonding yield. The bonding yield is defined as a fraction of sealing caps that are successfully bonded to the MEMS wafer and that seal the cavity without detectable leakage. Therefore, knowledge of the MEMS package leakage rate is important for package development, package reliability analysis, and device lifetime prediction.

Hence, the goal of this thesis is to develop a hermiticity testing procedure that will enable accurate measurement of the leak rate of the designed test structures, which in turn, could be used as a suitable in-line test method during the wafer bonding process.

Collaboration with Philips MEMS Foundry

The Proof-of-Concept for the hermiticity testing is developed at the Optics lab, which is part of the precision and microsystems engineering (PME) department at Delft University of Technology. This concept is developed for the Philips and the wafer-bonded test samples used for this project are fabricated at Philips MEMS Foundry. Philips MEMS Foundry is located at the High Tech Campus in Eindhoven, the Netherlands. The concerned division specializes in the process development and manufacturing of custom MEMS and electronic and optical micro-assemblies for their customers. Within this division, this project is focused on the wafer-bonding group. There are different bonding techniques available for wafer-level packaging which include fusion bonding, anodic bonding, solder bonding, eutectic bonding, thermo-compression bonding, direct metal-to-metal bonding, ultrasonic bonding, low-temperature melting glass bonding, and adhesive bonding. Among these techniques, the fusion bonding technique is predominantly used at Philips MEMS foundry to create sealed-off cavities for devices like pressure sensors, microfluidics for gas sensing, accelerometers, etc. Hence, in this project, the hermicity testing is targeted on cavities made using the fusion bonding technique.

2
Literature Review

This chapter begins with a concise overview of silicon fusion bonding, followed by an elaboration of several test techniques utilized for assessing hermeticity. Subsequently, a comparative analysis of these methods will be shown, leading to a final determination of the preferred test method. The concluding section of this chapter presents a research question for this project, accompanied by a project proposal that establishes the subsequent steps that need to be undertaken in order to address the research problem.

2.1. Silicon Fusion Bonding

Fusion bonding is referred to as silicon-to-silicon bonding without any additional intermediate layers. In general, there are two types of fusion bonding, one is hydrophilic fusion bonding and another one is hydrophobic fusion bonding.

Most silicon wafers used for fusion bonding are covered with either native oxide (with a thickness of about 2nm) or purposely grown thermal oxide (as necessary for SOI substrates or for parts in microsystems that have to be electrically isolated). These oxides are typically covered with a monolayer or two layers of water molecules adsorbed on OH groups associated with the oxide, this causes the surface of the silicon wafer (hydrophilic). Alternatively, this silicon surface may be dealt with diluted HF leading to the removal of native oxide layers and a direct hydrogen coverage of the silicon surfaces which renders the surface hydrophobic. Ultimately, surfaces of hydrophilic silicon wafers contain OH groups bonded to Si, and surfaces of hydrophobic silicon wafers contain H bonded to Si.

There are 3 basic steps involved in the fusion bonding process preparation of wafers, bonding, and heat treatment as shown in Fig.2.1. Within these steps, there are variations with respect to hydrophilic bonding and hydrophobic bonding.

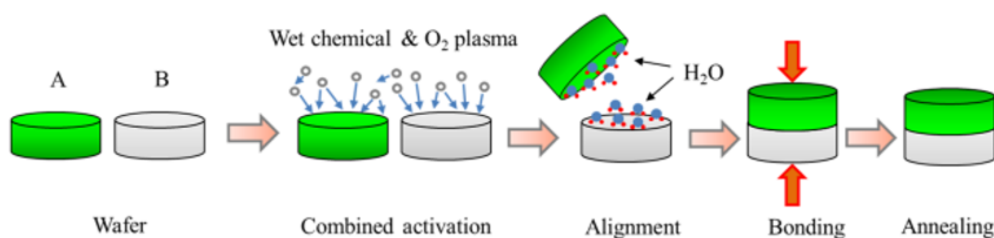

Figure 2.1: Steps involved in the fusion bonding process [5]

A) The preparation step must essentially satisfy the requirements of flat and smooth surface, cleanness, and reactivity:

A.1) Flat and smooth surface: Since the interaction forces at the interface act only a few nanometers, the direct contact of whole surfaces of two wafers is required for wafer bonding. More precisely, only if 2 surfaces are in contact with each other in a range less than $\sim$ 1nm does a bond take place. Silicon wafers with obvious surface waviness and roughness will result in a small area of contact, thus yielding voids or gaps in the bond interface even failing to bond. Fig.2.2 illustrates this.

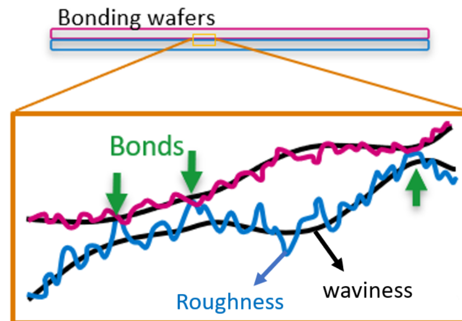

Figure 2.2: Illustration of voids or gap formation at the bond interface due to surface waviness and roughness

A.2) Cleanliness: The surfaces of two mirror-polished silicon wafers require careful cleaning to prevent any particle, organic, and ionic contamination. The effect of these three types of contamination in terms of bonding is summarized in Table.2.1.

Table 2.1: Effects of contamination on bonding quality

Contamination types	Consequences
External particles	Act as spacers and produce a separation
Organic materials (Hydrocarbons from air)	The quality of adhesion becomes degraded. It might lead to the generation of thermally induced voids during the annealing process
Metallic residues	No significant influence in degrading the bond quality, but on electrical properties of the semiconductor material.

To remove these contaminations, a standard hydrogen peroxide wet cleaning procedure (mixture of NH_4OH, H_2O_2, and DI water) is used. This step removes charged particles and organic materials. Following that a mixture of HCL, H_2O_2, and DI water is implemented to clean metallic residues. The alternative procedure is to use a H_2SO_4:H_2O_2 (piranha clean) mixture to remove organic and metallic type contamination.

Upon cleaning, there is often the important choice of whether the direct bonding should be performed with a hydrophobic or hydrophilic surface. The wafers may be thermally oxidized or just contain a native oxide which is made hydrophilic by a proper surface treatment. The surface oxide may also be removed by a dip in hydrofluoric acid (HF) which leads to hydrophobic hydrogen coverage of the silicon surfaces.

A.3) Activation for reactivity: The goal of activation is two-fold to maximize the available free surface energy, which is very important for bonding. This involves terminating the wafer surface with the dangling bonds which would be very reactive in the case when the wafers need to be exposed to cleanroom air before the direct bonding step can be performed.

For hydrophobic silicon surfaces, the dangling bonds are terminated by hydrogen and fluorine, whereas for hydrophilic surfaces it is terminated by oxygen-hydrogen (OH) groups (silanol groups). The free surface energy of this OH-terminated surface is approximately 5 times higher due to hydrogen bonds. Thus, in general, it is more difficult to initiate a direct bond with hydrophobic than with hydrophilic silicon wafers.

The activation for the hydrophilic surface can be performed by chemical activation. It can be achieved by treating with ammonium hydroxide/oxygen plasma/nitric acid surface treatment. Using these methods, the high density of OH groups could be increased on the bonding surfaces.

B) Bonding: The two mirror-polished and prepared surfaces are brought into contact at room temperature in a vacuum. The bonding is initiated at a center point by slightly pressing the wafer together locally. The bonded area then spreads over the whole wafer.

C) Heat treatment: After the room temperature bonding, the adhesion between two wafers is determined by van der Waals interactions or hydrogen bridge bonds and one or two orders of magnitude lower than covalent bonding. For practical applications, a strong covalent between the wafer surfaces is needed that has a higher bond energy, this step is accomplished by the annealing process. In general, annealing is performed as high as 1100 degrees C to create a strong bond energy between the surfaces.

For hydrophobically bonded wafers during heating, the reaction consists of sequential hydrogen desorption and silicon-silicon covalent bond formation according to Eq.2.1.

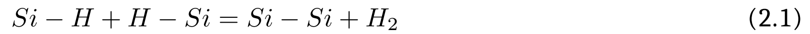

$$Si - H + H - Si = Si - Si + H_2 \tag{2.1}$$

At temperatures up to about 500 degrees C, the hydrogen does not diffuse into silicon but rather diffuses along the bonding interface.

In the case of hydrophilic wafer bonding, the end result is again the generation of molecular hydrogen but with the intermediate steps involved. Initially, there exists molecular water at the interface in terms of monolayers of water adsorbed on hydrophilic oxides. Molecular water will also partly come from the reaction 2.2, which starts to form strong covalent bonds across the bonding interface at temperatures above 120 deg C.

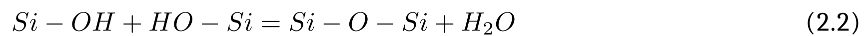

$$Si - OH + HO - Si = Si - O - Si + H_2O \tag{2.2}$$

With the further increase in temperature, molecular water will oxidize the surrounding crystalline silicon and form molecular hydrogen via the following reaction 2.3.

$$Si + 2H_2O = SiO_2 + 2H_2 \tag{2.3}$$

In general hydrogen molecules resulting from reaction 2.3 dissolve with the oxide present at the interface. However, sometimes, increased generation of hydrogen molecules cannot be cannot appreciably be dissolved in the oxide, rather it generates a gas pressure at the interface. This pressure may lead to the formation of interface bubbles or the weakening of the interface bonding. For this reason, annealing is usually performed as high as 1100 degrees C to avoid such formation of interfacial bubbles.

2.2. Types of Leak

Before finding an effective hermiticity test method, understanding the possible leak types through the bond interface is essential.

2.2.1. Flow through leak channel

Quality of the bonding is dependent on the active contact area between 2 wafer surfaces. In the case of direct or anodic bonding, only if 2 wafer surfaces are in a contact with each other in a range less than $\sim$ 1nm a bond will take place. If the two wafer surfaces possess any waviness and roughness, then it leads to a small area of contact, thus yielding unbounded gaps in the bond interface [6].

Similarly, when foreign particles such as dust or debris are present on the material surface, wafers tend to deform around these particles and leave behind voids or bubbles at the bonding interface [6]. A schematic representation of unbounded gap or void formation is shown in Fig.2.3.

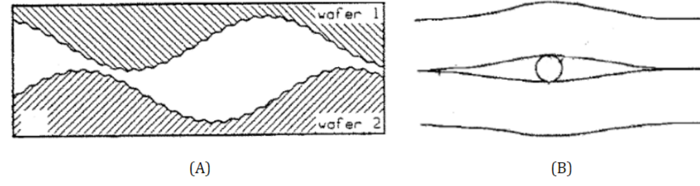

Figure 2.3: Schematic representation of void or gap formed due to A) rough and wavy contacting surfaces B) particle at the bond interface [6]

The presence of voids or unbounded gaps between the contacting surfaces is commonly perceived as a connected leak channel extending from the outside surface of the package to the internal cavity. Gas flow through these leak channels can be in a continuum flow regime/ slip regime/ transition regime or free molecular regime depending on the dimensions of the channel and the characteristics of the gas. The Knudsen number (K_n) is used to differentiate between the types of flow regimes. This dimensionless number is equal to the ratio of the mean free path for gas molecules (λ) to the characteristic dimension, through which the gas is flowing, which is the distance between surfaces having the most influence on the gas molecules [7]. For a tubular microchannel, the characteristic dimension refers to the diameter of the channel 'd'. So, for a tubular channel K_n is given by:

$$K_n = \frac{\lambda}{d} \tag{2.4}$$

The mean free path (λ) is the average distance a gas molecule travels between successive collisions and is defined as:

$$\lambda = \frac{1}{\sqrt{2}\pi\sigma^2 n} \tag{2.5}$$

Where σ is the diameter of the gas molecule and n is the number density. The value of λ is inversely proportional to the pressure. Thus, as leak channel size gets smaller and /or pressure decreases, K_n will increase.

When λ is greater than the dimensions of the leak channel (i.e., high K_n), intermolecular collisions become less frequent, and the gas molecules collide predominantly with the surfaces of the channel walls. When K_n>10, the gas flow is considered to be in the free-molecular regime and the vast majority of molecular interaction is with the structural surface. Consequently, the surface characteristics influence gas flow significantly in this regime. The gas flow rate in the free molecular regime for a channel having length (L) » diameter (d) is given in Eq.2.6 [8].

$$Q_m = \frac{2}{3}\pi\frac{r^3}{l}\nu_m(p_1 - p_2) \tag{2.6}$$

Where Q_m is the molecular leak rate, r is the radius of the leak channel, l is the length of the leak channel, ν_m is the mean molecular speed of the gas given in Eq.2.7, p_1 is the high pressure and p_2 is a low pressure.

$$\nu_m = \sqrt{\frac{8R_0T}{\pi M}} \tag{2.7}$$

Where R_0 is the universal gas constant, T is the temperature and M is the molecular mass of the gas.

With small K_n < 0.1, viscosity effects dominate due to greater inter-molecular collisions. The continuum regime describes the behavior of gas when $0<K_n<0.001$. The gas flow rate in the continuum regime for a channel having L»d ([8]) is given by:

$$Q_v = \frac{\pi r^4}{8\eta l}p_m(p_1 - p_2) \tag{2.8}$$

Where Q_v is the viscous leak rate, η is the viscosity of the gas and p_m is the arithmetic mean of p_1 and p_2.

As K_n increases to $0.001<K_n<0.1$, the gas is considered to be in the slip regime and the gas velocity along the solid surfaces is no longer zero. As K_n further increases to $0.1<K_n<10$, the gas is considered to be in the transition regime, and the gas molecules interact more with the wall surface and less with each other. Eq.2.9 shows the gas flow rate in the transitional regime [8] for a channel having L»d.

$$Q_t = Q_v \frac{1 + 2.507(r/\lambda)}{1 + 3.095(r/\lambda)} Q_m \tag{2.9}$$

Where Q_t is the transitional leak rate. The mean free path of the gas (λ) in an expanded form is given by:

$$\lambda = \frac{k_B T}{\sqrt{2}\pi d^2 p_m} \tag{2.10}$$

Where k_B is the Boltzmann's constant and d is the molecular diameter of the gas.

2.2.2. Permeation through silicon oxide or silicon

Through gas-dependent measurements, SiO_2 films were known to be permeable to gases such as He, Ne, Ar, Kr, and D_2 [9]. The main reason for permeation is attributed to the fact these oxide films have an unorganized lattice structure that has many larger holes in the crystal structure, which makes it possible for gases to permeate [10]. On the other hand, it was observed that silicon also has intrinsic porosity to allow the gas molecules to diffuse in the free space between the molecular chains based on the helium permeation experiment [11].

Permeation occurs in several steps as follows [10]:

1. Impact of gas atoms or molecules on the surface.
2. Adsorption
3. Possible dissociation upon adsorption
4. Solution of the gas in the wall material at the incoming surface to some equilibrium solubility value.

The first 4 steps describe the sorption of gas molecules onto the material which can be described by the term solubility. The last step in permeation is:

5. Movement of the gas atoms from this saturated surface layer through the interior as atoms or ions, under a concentration gradient, to the outgoing surface. This constitutes the diffusion mechanism . Thus the permeation is the product of solubility and diffusion as described in the equation below:

$$P = SD \tag{2.11}$$

Where P is the permeability coefficient in mol/sec.cm.atm, S is the solubility in mol/cm^3.atm, D is the diffusion coefficient in cm^2/Sec.

The total material amount of material,q, permeating a membrane is given by [10]:

$$q = \frac{PAt(p_1 - p_2)}{d} \tag{2.12}$$

Here P is the permeability coefficient,A is the area of the membrane exposed,t is the time, p_1 is the gas pressure on the higher pressure side, p_2 is the gas pressure on the low-pressure side, and d is the thickness of the membrane along the gas molecules travels.

2.2.3. Outgassing

In high vacuum conditions, when hermetic bonding has been optimized, it is essential to consider the amount of gas coming from the internal device and package material layers. Outgassing can occur during the annealing step of the bonding process. These residual gases are forced out from material surface layers by the elevated temperature and cannot be easily reabsorbed by the materials at lower temperatures so these gases contribute to an increase in cavity pressure. Outgassing can also occur at room temperature

throughout the device's lifetime as gases are released continuously from the bulk material or surface layers of internal materials. When this type of outgassing exists, the internal cavity pressure will slowly increase over the device's lifetime. In the case of ultra-high vacuum packaging, outgassing can be the dominant 'leak' source and even a small amount of outgassing can be detrimental to the device's performance leading to premature failure. The gas type which is found to outgas during the fusion bonding process is H_2 and H_2O [12], it is also explained via the equations.2.2 and eq.2.3 in section.2.1.

2.3. Hermiticity Test Methods

Different hermiticity test methods for MEMS packages are discussed in this section. The ways of measurement are divided into two categories, one based on the amount of gas concentration in the cavity and another one based on monitoring the cavity pressure.

2.3.1. Helium Leak Test

In this method, the test package is stored in a vacuum chamber and exposed to helium (He) gas for some time, referred to as 'bombing'. Pressurized helium enters the package if there is a leakage. Later the chamber is vented and connected to the He mass spectrometer. Hermiticity is assessed by measuring the He leaking out of the package and it is quantified as a 'measured leak rate'. A schematic illustration of the test method along with the steps involved is shown in Fig.2.4.

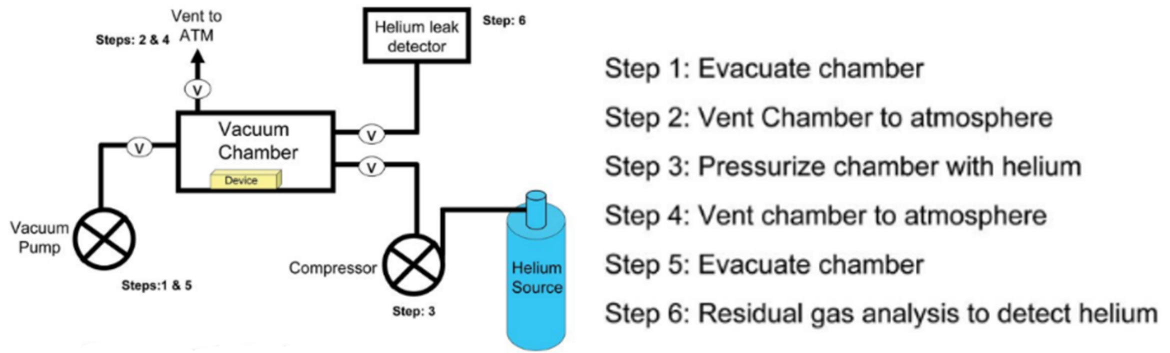

Figure 2.4: Steps in helium leak test [13]

The measured leak rate 'R' is the helium leak rate of the package under specific test conditions employed. Before comparing the leak rate of packages, R is converted to the standard leak rate 'L'. L is the quantity of dry air at 25°C flowing through a leak or multiple leak paths per second when the high-pressure side is 1 atm. R and L are related by the standard Howl-Mann equation [14], as shown in Eq. 2.13.

$$R = \alpha L \left(1 - e^{\beta L}\right) e^{\gamma L} \tag{2.13}$$

with

$$\alpha = \frac{P_E}{P_0}\left(\frac{M_A}{M}\right)^{\frac{1}{2}}, \beta = -\left[\frac{t_1}{VP_0}\left(\frac{M_A}{M}\right)^{\frac{1}{2}}\right], \gamma = -\left[\frac{t_2}{VP_0}\left(\frac{M_A}{M}\right)^{\frac{1}{2}}\right]$$

Where P_E is the pressure of exposure and P_0 is the atmospheric pressure. M_A and M are the molecular weight of air and tracer gas in grams respectively. t_1 is the time of exposure to P_E; t_2 is the dwell time between the release of pressure and leak detection and V is the internal volume of the device package cavity.

2.3.2. Radioisotope Leak Detection

The Kr^{85} radioisotope emits γ radiation with 0.5 MeV during its radioactive decay. This radiation easily penetrates most semiconductor package walls and can be monitored outside the package [15].

The method involves a test sample being pressurized in an inert gas N_2 along with a weak concentration of Kr^{85}. The sample is then transferred from the bombing to the scintillator counter chamber to register the gamma count rate (R^*) emitted from the sealed cavity. The relation used for obtaining standard leak rate (L) [15], is given in Eq.2.14.

$$L = \frac{R^* P_0}{P_E^* SKT} \tag{2.14}$$

Where P_0 is standard atmospheric pressure (atm). $P_E{}^*$ is the pressurization value of the gas mixture (atm), and K is the overall counting efficiency of the detector for a particular package type at a particular location within the crystal detector well (count-rate/μCi). S is the specific activity of the Kr^{85}-N_2 gas mixture (μ Ci/atm.cm^3) and T denotes the pressurization time with krypton (sec).

2.3.3. Fourier Transform Infrared Spectroscopy (FTIR)

FTIR method is based on gas molecule absorption of infrared radiation (IR). The technique involves bombing of the sample in a high IR-absorbing tracer gas such as N_2O /SF_6 /OCS /HCL /H_2 (in the order of preference) [16]. Later, it is analyzed using IR transmission measurements to determine the partial pressure of the gas inside the package.

Beer-Lambert law [17] (Eq.2.15), facilitates the relationship between the measured transmittance (T) and internal partial pressure (P_{in}).

$$A = \epsilon c l = -logT = \log \frac{I_0}{I} \tag{2.15}$$

Where A is the absorbance, c is the molar concentration (mol.L^{-1}), ϵ is the molar absorption coefficient (L.mol^{-1}.cm^{-1}), and l is the optical path length (cm). I and I_0 are the incident and transmitted intensities, respectively.

With Eq.2.15, the partial pressure could be calculated using ideal gas law as presented in Eq.2.16.

$$-\log T = \frac{\epsilon l P_{in}}{RT} \tag{2.16}$$

Schematic representation of the FTIR method is shown in Fig.2.5.

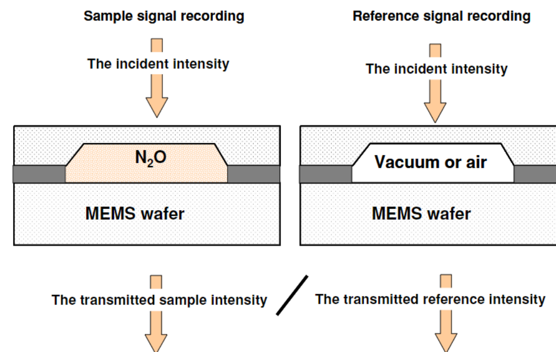

Figure 2.5: Schematic representation of transmittance measurement used in FTIR [17]

2.3.4. Raman Spectroscopy

Raman spectroscopy is an optical technique, in which a monochromatic light source interacts with phonons or other molecular vibrations of an unknown molecule. The light source is usually a laser source and can be in the visible, ultraviolet, or infrared range [18]. After transmitting light through the cavity containing gas, a large number of molecules will undergo Rayleigh scattering (scattered light wavelength close to the incident light) and a small number of molecules will undergo stokes Raman scattering and anti-stokes Raman scattering [19]. Scattered light from the sample is collected by a lens and passed through a monochromator, which filters the wavelength based on Rayleigh scattering and the rest passes through to the detector.

In the present technique, test samples are bombed with an external gas and subjected to quantitative measurement of Raman scattering intensity ($I_{scat.}$). This $I_{scat.}$ is proportional to no.of.gas molecules (N) given by the Eq.2.17 [20].

$$I_{scat.} = I_0 N V \frac{\pi^2}{\epsilon_0 \lambda^4} \frac{d\sigma}{d\Omega} \tag{2.17}$$

Where I_0 is the incident laser intensity, N is the density of the scattering species in the probed volume V_p, λ is the excitation laser wavelength and $\frac{d\sigma}{d\Omega}$ is the scattering cross-section which depends on the particular experimental conditions such as collecting geometry, state of incident polarization and the studied species. By using the ideal gas law ($P_{in}V=Nk_BT$), the internal partial pressure of the gas can be calculated, and eventually the leak rate as well.

2.3.5. Infrared (IR) Transmission Through Copper Test Pattern

An in-situ test method uses a copper layer within the package to monitor internal pressure [21]. In this method, the optical transmission of copper over time is measured as the material oxidizes. This technique relies on the package being transparent to IR wavelengths. This testing is suitable for on-wafer testing but is a one-time testing technique. Once the copper test pattern is oxidized, the test cannot be repeated.

2.3.6. Cap Deflection Test

This test relies on the package cap being flexible enough to deflect according to the pressure difference between the inside and outside of the package. The sample under test is placed in a chamber where pressure can be varied according to the maximum permissible pressure of the package or the limit of the chamber by infusing an external gas [7].

If the sample is non-hermetic, then the pressure inside the package and deflection of the cap changes over time. By monitoring the deflection, it is possible to estimate the leak rate. When the internal pressure is less than the external pressure, the cap would be in a downward deflected state. With the increase in internal pressure, the cap tends to bend upward. A simple visualization is presented in Fig.2.6.

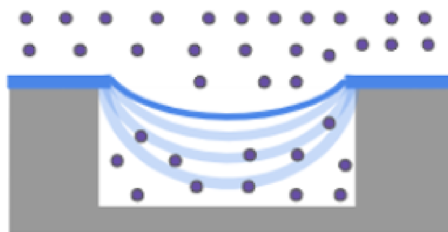

Figure 2.6: Illustration of cap deflection due to leak

2.3.7. Resonance Test

Leak rate of various gases across the membrane which is fusion bonded to a cavity can also be found using a mechanical resonance test. When a pressure difference is present across the membrane (ΔP=P_{in}-P_{out}), the membrane deflects (x_s), tension is induced in the material and thereby causes a change in resonance frequency (f_{res}). Relation between f_{res} and x_s, due to ΔP is given in the Eq.2.18 [22].

$$f_{res} = \frac{1}{2\pi}\sqrt{\frac{k_1 + 3k_3x_s^2}{m}} \tag{2.18}$$

Where k_1 is the linear spring constant and k_3 is the third order spring constant, m is the modal mass.

Fig.2.7 shows a sample frequency response of a device. If the pressure inside is higher, the membrane deflects upward, gets stretched, tension increases, and frequency increases (from point B to right). If the pressure outside and inside the cavity are equal, the membrane is flat, and its tension and frequency attain minima. Finally, if the pressure outside is larger, the membrane deflects downward, which causes the membrane to stretch, resulting in higher tension in the membrane and resonance frequency (from point A to left).

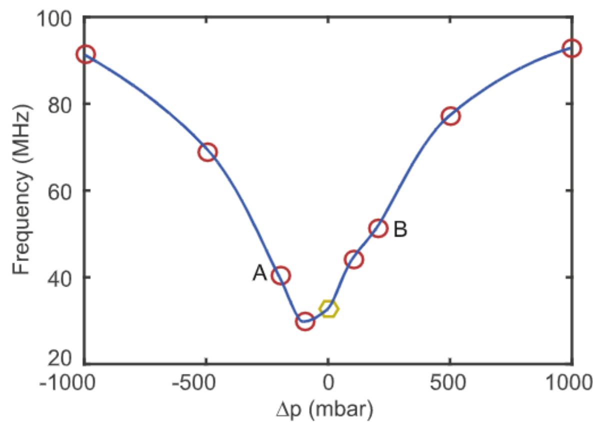

Figure 2.7: Frequency response as a function of pressure difference [23]

2.3.8. Q-factor Monitoring (In-Situ)

Many in-situ test structures have been designed for use as pressure sensors to monitor leak rates in small MEMS packages. When the device contains a free-standing structure (as shown in Fig.2.8), the Q-factor can be measured as a function of internal pressure before and after packaging.

As internal pressure increases, energy dissipation through air molecule collision increases resulting in an increase in damping and a corresponding decrease in the Q-factor of embedded resonator [24]. This test can be conducted at any stage throughout the device's lifetime for long-term monitoring.

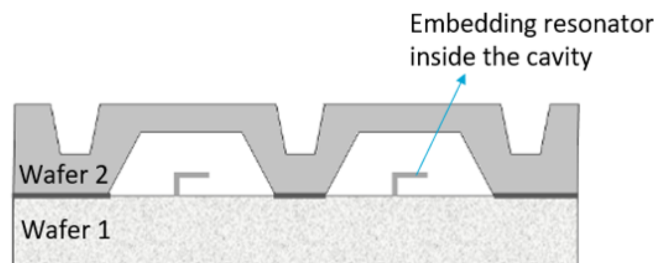

Figure 2.8: Schematic representation of resonator embedded inside the cavity [3]

2.3.9. Micro-Pirani Gauge (In-Situ)

Several test structures that exploit the relationship between thermal impedance and pressure have been designed to monitor hermiticity. For the high vacuum measurement of the package, a MEMS Pirani gauge is often used as the pressure sensor. The operation principle of the Pirani is that the temperature-dependent resistance of the gauge is dependent on the ambient pressure. Electric resistance is increased, when a metal structure is heated. Depending on the amount of surrounding gas, this heat will be conducted away from the structure such that temperature, hence resistance will decrease.

The thermal impedance TI, which is defined by the Eq.2.19 is dependent on pressure [14]. From the calibrated measurement of TI versus pressure, the pressure inside the package is known if the thermal impedance is known.

$$TI = \frac{\Delta T_{avg}}{\Delta P_E} \tag{2.19}$$

where ΔT_{avg} is the change of the average temperature across the Pirani gauge; ΔP_E is the change of the electrical power.

2.4. Studies Conducted Using Hermiticity Test Methods

2.4.1. Testing of Wafer-Level Packages

This subsection covers hermiticity test studies conducted on different wafer-bonded packaged devices.

Eutectic bonding for packaging

In eutectic bonding, wafers are bonded with an intermediate metal layer that can produce a eutectic system. These eutectic metals are alloys that transform directly from solid to liquid or vice-versa at a specific composition and temperature without passing a two-phase equilibrium.

Souriau, Jean-Charles, et al.[25] used the krypton leak method for testing a cardiac implantable device, which integrated a MEMS accelerometer and an application-specific integrated circuit (ASIC) chip on a silicon substrate. The device was packaged using AuSi as the eutectic alloy composition, as shown in Fig.2.9. The reliability test was conducted by bombing the test sample (cavity volume: 4 mm^3) under 6 bar pressure for 6 days using krypton gas. The measured leak rate was approximately 10^{-17} $mol.sec^{-1}$.

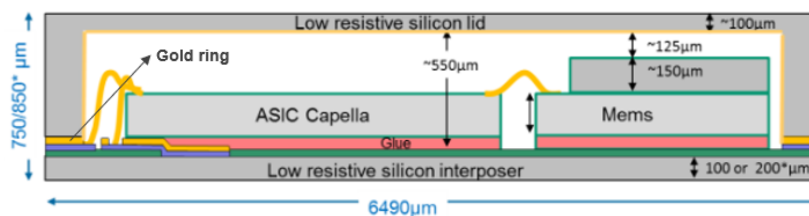

Figure 2.9: Schematic representation of the implantable device [25]

When wafer level packages became small (typically 0.3 mm^3), in-situ evaluations were established to detect sensitive leak rates. Van Der Wel, P. J., et al.[26] used mechanical resonance of the RF-MEMS top electrode for testing the RF MEMS switch package, which was assembled using an AuSn bonding process. 3 types of leak rate tests were performed: storage in an autoclave for 1920hr with a water vapor pressure of 2 bar, high-temperature storage (HTS) for 2400 hrs at 121 ^{o} C, and bombing test using 10 bar of N_2 for 1000 hrs. The majority of the test samples do not show any change in Q-factor indicating an average leak rate of 10^{-20} $mol.sec^{-1}$ with 0.9mbar as internal pressure.

Cap-deflection method was used by Elger, Gordon, et al. [27] for assessing the wafer-level packaging of optoelectronic devices. Encapsulation was done using a silicon wafer with Au as an intermediate layer. This resulted in the micro-cavity formation with an internal volume of 0.27 mm^3. Silicon cap deflection was monitored during the He leaks into the package using an optical interferometer. With the 6 bar bombing pressure and 8 hours time difference between two successive scans, a leak rate resolution of 10^{-14} $mol.sec^{-1}$ was obtained.

Gueissaz, F [28] applied the IR transmission test for the hermiticity assessment of the magnetostatic MEMS switch package. The MEMS switch was manufactured on a borosilicate glass wafer and wafer-level packaged by a second wafer with AuSn as a eutectic alloy ring. It was shown that IR transmission in copper films increases with the degree of oxidation [28]. Therefore, a 30 nm thick copper layer was embedded inside the packaged cavity (volume: 0.0018 mm^3) and bombed with oxygen gas maintained at a temperature between 125 and 150° C. The resulted leak rate was about 10^{-20} $mol.sec^{-1}$.

Adhesive bonding for packaging

Adhesive wafer bonding deploys polymer adhesive as the intermediate layer to bear the forces involved to hold the surfaces together.

Veyrie, David, et al. [29] presented the FTIR spectroscopy method to deduce the cavity's leak rate from pressure variations. The method was performed on silicon-silicon micro-cavity test vehicles (volume: 20 mm^3), bonded with a BenzocycloButene (BCB) organic sealing ring (as shown in Fig.2.10). In order to carry out the FTIR test, samples were bombed with N_2O (with excellent IR absorption properties for mid-IR radiations), and the subsequent measurements led to leak rate calculation of 10^{-12} $mol.sec^{-1}$.

Figure 2.10: Structure of adhesive bonded test vehicle[29]

Lellouchi, Djemel, et al.[17] used the same method for testing the adhesive-bonded wafer packages of internal volume 3mm^3. Samples were pressurized to 5 bars for 96 hrs with N_2O gas. Evaluation of gas concentration inside the cavity by the mid-IR (400-4000 cm^{-1}) transmission measurement led to leak rate detection of 10^{-14} $mol.sec^{-1}$.

2.4.2. Thin-film packaging for MEMS devices

An alternative to the wafer-bonding concept for MEMS packaging is the thin-film deposition technique. In the thin-film approach, the encapsulation process is done on the same wafer where the MEMS devices are fabricated by depositing extra thin-film processing steps.

Santagata, F., et al. [30] developed a new tube-shaped Pirani gauge for in-situ testing of MEMS package. The gauge was buried inside the silicon substrate, which was encapsulated inside a thin-film micro-cavity (volume: $2x10^{-4}$ mm^3) made with SiN. The schematic representation is shown in Fig.2.11. Pressure and leak rates were measured over 4 months in time. The results indicated a pressure detection limit of 10^{-3} mbar along with a leak rate estimation of 10^{-22} $mol.sec^{-1}$.

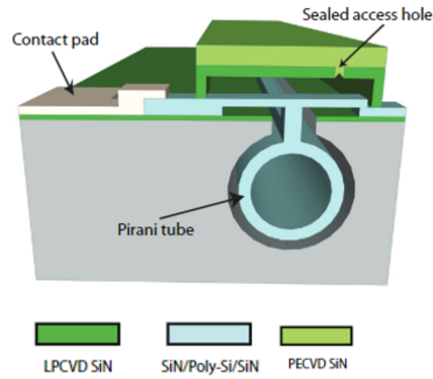

Figure 2.11: Representation of encapsulated Pirani tube [30]

2.4.3. Method of sealing the bond interface

Hermiticity assessment was not restricted to testing MEMS packages alone. Zekry, Joseph EE, et al. [31] used the deflection method for the evaluation of novel 0-level thin film vacuum packages for (RF-) MEMS. The package featured a cavity (volume: $3x10^{-4}$ mm^3) enclosed with a dielectric cap made of a nanoporous alumina membrane and a sealing layer of PECVD silicon nitride, as shown in Fig.2.12. Test samples were initially bombed in a He gas chamber for 2-3 days under the 3 bar pressure and the subsequent leak rate was calculated ($\sim 10^{-21}$ $mol.sec^{-1}$) using optical interferometer measurements. Rigorous testing observed that leakage through the bond interface reduces with increasing the width of the sealing ring.

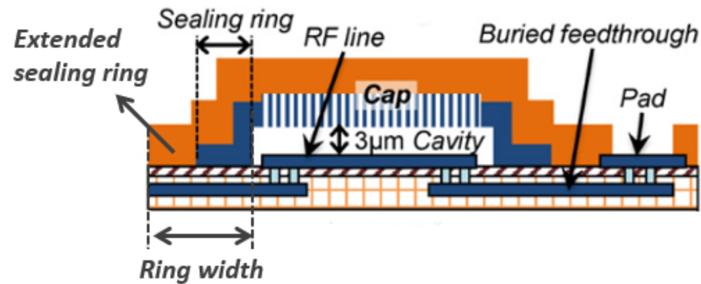

Figure 2.12: Package with laterally extended silicon nitride sealing-layer[31]

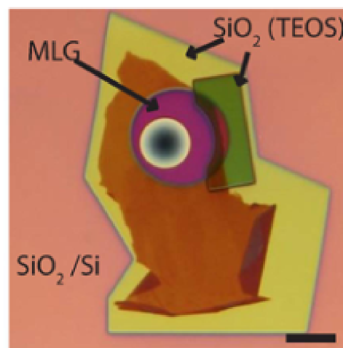

Figure 2.13: Optical image of graphene suspended device after sealing[22]

In another experiment, Lee, Martin, et al.[22] used the resonance frequency test and demonstrated a sealing method that consists of depositing SiO_2 (Tetraethyl Orthosilicate) along the edge of multilayer- graphene flakes suspended on a silicon cavity. The optical image of the device is shown in Fig.2.13. By sealing, leakage along the graphene-SiO_2 was blocked and observed to result in a reduction in the permeation rate of N_2 by a factor of 10^4. In this experiment, the suspended graphene flake was used as the differential pressure sensor. When a pressure difference is present across the suspended graphene, tension is induced in the material that causes a change in resonance frequency. To measure the resonance frequency, a complicated laser interferometric setup as shown in Fig.2.14 was used.

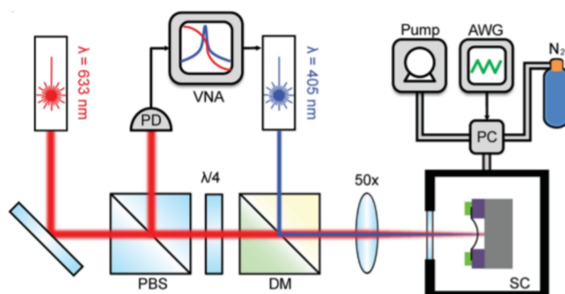

Figure 2.14: Schematics of the interferometer setup used for measuring resonance frequency [22]

Here, a modulated blue laser diode (λ = 405 nm) is used to optothermally actuate the graphene membrane. The motion of the graphene membrane is detected using a red He−Ne laser with wavelength, λ = 633 nm. The motion of the suspended graphene modulates the reflected red laser intensity via its position-dependent absorption of the standing light wave. This modulated light is collected at the photodiode (PD) and read by the vector network analyzer (VNA). This VNA finally probes the mechanical frequency response of the membrane.

2.4.4. Electrolytic Corrosion Of CMOS device

Stroehle, D [32] studied the degradation of aluminum interconnection lines of ICs due to electrolytic corrosion. The test vehicles (cavity volume: 20 mm^3) were standard CMOS devices in CER-DIP (Ceramic Dual In-line Package) and were first subjected to accelerated helium leak testing. Upon determining the leak rate, a moisture resistance test was performed to measure the increase in supply current.

The devices were stored in a helium gas chamber under the pressure of 20 atm, with exposure time between 4 and 12 hrs and dwell time of 0.5 hrs. Leak rates obtained from spectrometer measurements were between $\sim 10^{-11}$ and 10^{-13} mol. sec^{-1}.

2.4.5. Porous graphene for molecular sieving

Koenig, Steven P., et al. [33] used deflection and resonance tests to measure the transport of a range of gases through pores etched on graphene membranes. Graphene membranes were clamped to silicon-oxide micro-cavities (volume:10^{-9} mm^3) by surface forces.

Before etching the pores, a test was conducted to identify any leak from the graphene-suspended micro-cavities. For which, the samples were bombed in a chamber with a charging gas (H_2, CO_2, Ar, N_2, $CH_4$and SF_6) at 2 bar pressure for 4-12 days. Removed samples were monitored for leak rate by measuring the deflection of the membrane using an atomic force microscope (AFM). There was an average leak rate of 10^{-21} mol.sec^{-1}, which showed that gas species could able to enter the cavity through the substrate by slow diffusion.

2.5. Discussion

After an extensive review of several hermiticity test techniques, the potential limitations or issues associated with each approach have been considered and presented below:

1. Helium leak test: Helium spectrometer has a limited leak rate detection, which is approximately 10^{-13} mol/sec.

2. Radisotope leak detection: Since radioactive gas is used, therefore chamber becomes radioactive with time.

3. FTIR: Even a small concentration of high IR-absorbance gas outside the cavity affects the transmittance measurements.

4. IR transmission: The test sample cannot be reused, once the embedded layer completely oxidizes.

5. Raman spectroscopy: A small quantity of tracer gas outside the cavity can cause a weak scattering effect, which may lead to ambiguous leak rate measurement.

6. Cap deflection test: Improved deflection response is dependent on the geometrical parameters of the cavity, which can be limited by the fabrication process.

7. Resonance: A complex measurement setup is required to convert the change in deflection to a change in resonance frequency.

8. Q-factor (In-situ): When the cavity size is small, the fabrication of additional sensors becomes complicated.

9. Micro-pirani (In-situ): When the cavity size is small, the fabrication of additional sensor becomes complicated which is the same as above.

Based on the limitations listed above, it has been observed that techniques relying on direct measurement of gas concentration are not very much applicable for hermiticity testing when compared to methods that monitor pressure changes. As stated in the introduction chapter, for a MEMS package having a cavity volume of 0.1 mm ^{3} and with a requirement of sealed cavity pressure of 10^{-2} atm, a lifetime of 5 years, and an acceptable pressure increase over this lifetime of 10%, results in the maximum acceptable leak rate of this package of 6.34x10^{-16} atm.cm^{3}.sec^{-1} (2.82 x 10^{-20} mol.sec^{-1}). This means that the standard helium leak method based on spectrometer measurements is not usable due to its limited leak rate detection. Then, in the context of the radioisotope method, it is always important to establish appropriate handling protocols when conducting tests with gases such as Krypton. This precautionary measure is necessary to prevent any potential hazards caused due to the radioactive properties of the gas. This makes the radioisotope method not user-friendly. Finally, when FTIR and Raman spectroscopy methods are considered, if any target gas molecules exist in the external environment in addition to those within the cavity, leak rate measurements will be ambiguous.

Furthermore, according to many studies that employed different hermeticity test methods (as discussed in section 2.4), it was observed that pressure-based techniques are capable of assessing smaller cavity sizes with lower leak rates. This observation can be seen in the comparative chart in Figure 2.15, which presents the leak rates acquired from various hermeticity investigations done on MEMS packages employing stated methods.

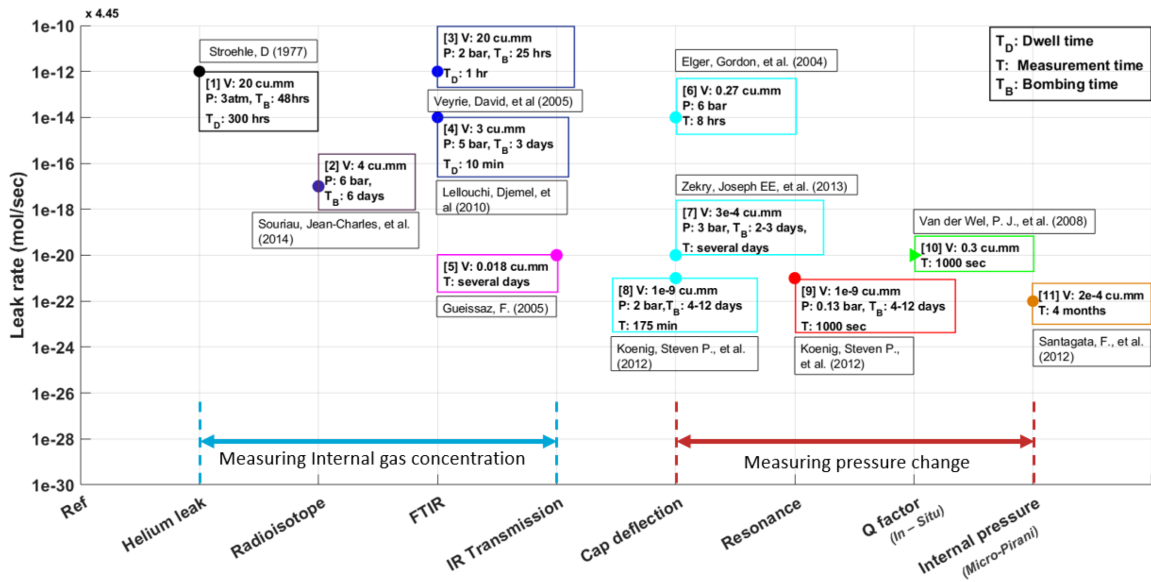

Figure 2.15: Plot of leak rates obtained using different hermeticity test methods

Now, among the pressure-based techniques, in-situ-based testing methods, such as the utilization of micro-sensors to measure the Q-factor and thermal impedance, pose significant challenges for in-line testing. This is primarily due to the intricate fabrication process required to integrate these sensors inside the cavity. Ultimately, while comparing the cap-deflection and resonance techniques, it becomes evident that the arrangement of the leak-test setup for the deflection method is the simplest. It only requires bombing the sample in a vacuum chamber and subsequent determination of the leak rate using deflection measurement. Hence, the cap-deflection method is regarded as the appropriate method for assessing hermiticity.

Besides the selection of test method, during the course of this literature review, it was observed that the hermicity methods were not only used to measure the leak rates exhibited by the MEMS packages but also to develop an understanding of how leakage works through these bonded or sealed cavities. Zekry, Joseph EE, et al. [31] and Lee, Martin, et al.[22] studied a sealing concept where a sealing material is deposited along the bond interface of test samples to observe the reduced leak rate. The problem with the sealing concept study is that once the bond interface has a sealing layer applied, these test samples cannot be used for repetitive testing. In such cases, it is essential to create a new set of samples each time. Therefore, an alternative approach is required to develop an understanding of the leakage mechanism.

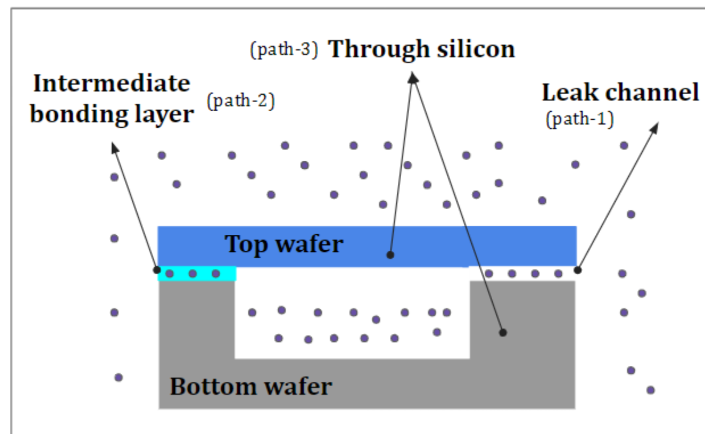

Figure 2.16: Illustration showing the leak pathways through which gas can leak

As depicted in Fig.2.16 the three potential leak pathways along which gas leakage can occur in bonded

wafers are the leak channels between the contacting surfaces and the permeation through the intermediate bonding layer which is oxide and the permeation through the silicon membrane or substrate. In the case of leak channels, the gas flow rate is proportional to the diameter and length of the channels, while in the case of diffusion through an intermediate bonding layer, it is proportional to the cross-sectional area and thickness of the layer (refer to section 2.2).

Since the gas flow rate is a function of the physical dimensions of leak pathways, in our case, it is decided to deliberately introduce leak pathways of various sizes to test the influence of these dimensions on the leak rates.

2.6. Research Question

With the aim of using the cap-deflection method to evaluate the leak rates of bonded wafers utilizing the deliberately introduced leak paths, the research question that is addressed in this project is:

How to accurately measure the leak rate of bonded wafers using the cap-deflection method such that it can be adapted as a suitable in-line testing technique.

2.7. Planning for design, fabrication and experiments

We divided the entire research into 3 stages to address the research problem: The theoretical modeling and design stage discussed in Chapter 3, the measurement method, fabrication, and uncertainty analysis stage discussed in Chapter 4, and the experimental stage discussed in Chapter 5.

Stage - 1: Theoretical modeling and design

The first stage is aimed to design the best test structure which is nothing but the best dimensions of cavity and membrane which can be fusion bonded to provide the highest sensitivity in measuring as much small leak rate possible. Here, the highest sensitivity means the higher deflection response of the membrane for a given pressure difference.

The design process will start with establishing a relationship between test structure parameters (cavity gap height, membrane diameter, and thickness) and leak rate. Then it expands to a comparative study between different membrane shapes (circle, square, and rectangle) to identify which membrane exhibits the highest leak-rate measuring capability. Further, it extends to a numerical study to understand the order leak rates which could be measured with respect to different design parameters for the test structure. Finally, the best structure design will be recommended based on an analysis with respect to certain design rules. The considered design rules are: (1) membranes not to undergo plastic deformation under high annealing temperatures during fusion bonding, and (2) membranes not to collapse with the surface of the cavity due to its deflection. This analysis provides the suitable diameter of the membrane for a given thickness and a suitable gap height for the chosen membrane dimensions.

Stage - 2: Fabrication, measurement method, and uncertainty analysis

In the second stage, we fabricate the test structures. Here the fabrication is not only for one test structure design (i.e., the cavity with the best design) but also includes different dimensions for a given thickness of membrane and cap height of height. The reason behind having different dimensions for fabrication is to have safety in the design choice, Suppose if one diameter fails due to plastic deformation then other membranes could be used for the leak test measurements.

We fabricate two types of test structures: one with cavities having defined leak paths and another with cavities having no defined leak paths. For samples with defined pathways, to start with, it is decided to have leak channels between the silicon-bonded cavities with different dimensions.

With the fabricated samples, deflections are decided to be measured using the digital hologram microscope (DHM-Lynceetec). Before going to the experimental stage an error analysis will be carried out. In this sub-stage, multiple fabricated samples will be subjected to measurements of cavity gap height, membrane diameter, membrane thickness, and leak channels to check the dimensions and topography of surfaces obtained after the fabrication process. The error analysis will further extend to errors in deflection measurements, which will be studied using the DHM. Based on this error analysis on deflection measurements, an estimation would be made of uncertainty in measuring leak rate, this will provide with how much accuracy leak rate could be measured, which would be an important part of this project work.

Stage - 3: Experiment

In the experimental stage, the test samples will be first subjected to a pressure-deflection sensitivity characterization experiment. In this experiment, the deflection of membranes will be measured by varying external pressures by placing the samples in a vacuum chamber setup connected to a pressure controller, and these deflection values will compared with the analytical models to get a first validation of whether the membranes exhibit deflection as per the design or not. This pressure-related experiment will also help to identify whether any membranes have undergone plastic deformation. By varying the pressure, if any membrane does not deflect, this would indicate that the membrane has undergone plastic deformation. Through this, we will get to know which diameter membrane is plastically deformed for a specified thickness.

Following this, the first leak testing experiment will be conducted. In order to understand how leakage changes the deflection of the membrane, this first experiment will conducted on samples having the defined leak channels. The leak testing will be conducted using the same vacuum chamber setup in the presence of air. If air molecules are shown to be non-penetrable, then other desired gases will be used. Since they have deliberate leak channels, it is expected that these samples would show a higher leak rate and thereby enable us to see how best the leak testing could be conducted. The leak rate measured from this experiment will be compared against the analytical expressions that model the flow of gases through channels.

The final experimental stage involves the testing of samples with no defined leak channels. In this case, the samples would be first tested for the presence of air leakage or outgassing by testing the deflection of membranes for multiple days in the air. If no significant change is observed, then these samples will be observed for change in deflection in the vacuum chamber under the presence of a desired gas species. In our case, the chosen desired gas species is helium due to its smallest kinetic diameter. Since the samples do not have any known leak paths, the measurements will be taken for multiple days to avoid any inaccuracies in obtaining a leak rate. If the sample is found to have a change in deflections, then the deflection values will be used to calculate the leak rates, and using this data a comparison will be made with the literature to check, along which path the leakage could have occurred. With this step, the final step of the project will be reached and subsequently, the thesis report can be written and finalized.

3
Test Structure Design

In this chapter, theoretical modeling and design of test structure for hermiticity testing is discussed. First, an analytical relation is established to indicate the influence of critical parameters of test cavities on leak rate. Thereafter, an appropriate test structure type is selected based on the analytical relation provided for leak rate. Finally, a suitable test structure design is recommended for hermeticity testing experiments based on analytical calculations and computational simulations with consideration of different design parameters.

3.1. Test Structure

In this section, an equation is derived to understand the influence of test structure parameters on leak rate. The test structure is basically a membrane bonded to a cavity. The key parameters of the test structure are the area (A) of the membrane, stiffness of the membrane (K), and gap height of the cavity (g). All these key parameters are illustratively shown using a leaking wafer-bonded cavity in Fig.3.1.

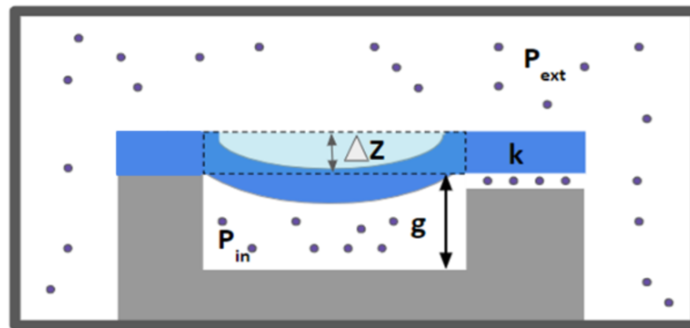

Figure 3.1: Illustration of leaking bonded wafers along with indicated critical parameters. Downward deflection is considered as positive

Let N_{in} be no.of. molecules inside the cavity and the bonded membrane is flexible such that the volume inside the cavity depends on the deflection of the membrane: $\mathbf{V_{in} = V_0 - A\, c_1\, Z}$ (with V_0 - an internal volume of the cavity and A c_1 Z - the volume of deflected membrane). Here V_0 = Ag, c_1 - A constant which depends on the shape of the deformed membrane and Z - maximum deflection of the membrane.

Leakage inside the cavity is governed by the differential eq.(3.1).

$$\frac{dN_{in}}{dt} = \frac{\Delta P}{F} \tag{3.1}$$

Where $\frac{dN}{dt}$ is the leak rate or molecular flux, F is the flow resistance, and ΔP = $\mathbf{P}_{ext}$-$\mathbf{P}_{in}$ is the pressure difference across the membrane. Here, F is a function of the diameter and length (if the flow occurs through a leak channel) or represents permeability (if the flow occurs through silicon or oxide layer).

Using the leak rate eq.3.1 and ideal gas law, equation for deflection over time due to the leak inside the cavity can be derived as follows:

$$P_{in}V_{in} = N_{in}RT \tag{3.2}$$

Where R is the molar gas constant, and T is the temperature. On substituting the expansion V_{in} and ΔP in the eq.3.2 becomes:

$$(P_{ext} - \Delta P)A(g - c_1 Z) = N_{in}RT \tag{3.3}$$

$$P_{ext}Ag - P_{ext}Ac_1 Z - \Delta PAg + \Delta PAc_1 Z = N_{in}RT \tag{3.4}$$

In the above equation P_{ext}, A, g, R, and T are considered constant. Differentiating the above eq.3.4 leads to:

$$(-P_{ext}Ac_1 + \Delta PAc_1)\frac{dZ}{dt} + (-Ag + Ac_1 Z)\frac{d\Delta P}{dt} = \frac{dN_{in}}{dt}RT \tag{3.5}$$

Deflection of the membrane (Z) depends on the stiffness of the membrane (K) and ΔP. By assuming a linear relation between Z and ΔP:

$$KZ = A\Delta P \tag{3.6}$$

The above equation in differential form:

$$\frac{d\Delta P}{dt} = \frac{K}{A}\frac{dZ}{dt} \tag{3.7}$$

On substituting eq.3.7 in eq.3.5, we get a generalized expression relating deflection rate and leak rate:

$$(-\frac{dZ}{dt})(\frac{K}{A})(Ag + \frac{P_{ext}A^2 c_1}{K} - 2Ac_1 Z) = \frac{dN_{in}}{dt}RT \tag{3.8}$$

$$(-\frac{dZ}{dt}) = (\frac{dN_{in}}{dt})(\frac{RT}{V_{eff}})(\frac{A}{K}) \tag{3.9}$$

Where V_{eff} is the effective volume = $V_{eff,o}$-2 Ac_1Z ; $V_{eff,o}$ = Ag + $\frac{P_{ext}A^2c_1}{K}$.

From the relation between deflection rate and leak rate, it is observed that for sensitive detection of a leak, we need to maximize the value of (A/K) and minimize V_{eff} i.e., to use the membrane with a large (A) and low stiffness (K) and cavity with low effective volume (V_{eff}).

on substituting eq.3.1 in eq.3.9, we get:

$$(-\frac{dZ}{dt})(\frac{K}{A})V_{eff} = \frac{\Delta P}{F}RT \tag{3.10}$$

Again by substituting expression for ΔP from eq.3.6 in eq.3.10, we get:

$$(-\frac{dZ}{dt})(\frac{1}{Z}) = \frac{RT}{V_{eff}F} \tag{3.11}$$

By assuming a constant effective volume V_{eff}, an approximation can be made for deflection over time (Z(t)) due to leak. Integration of eq.3.11 gives the exponential decay function, as shown in eq.3.12.

$$Z(t) = Z_0 \;\; exp(-\frac{RT}{FV_{eff}}t) \tag{3.12}$$

3.2. Selection of Test Structure

In this section, a numerical analysis is done to compare the ability of different types of membranes to measure leak rates. Through this analysis, a suitable type of membrane would be selected and used up for further test structure design.

Three membrane shapes are considered for this analysis, which are circle, square, and rectangle. To compare the leak rates, eq.(3.9) needs to be adapted for the considered membrane shapes. This is done by using their pressure-deflection analytical expression.

For a simple analysis, the deflecting membrane is considered to be made of isotropic material. For an isotropic material, the static deflection surface w(x,y) is generally calculated by solving the Kirchoff-Love isotropic plate equation [34]:

$$\frac{\partial^4 w}{dx^4} + 2\frac{\partial^4 w}{dx^2 dy^2} + \frac{\partial^4 w}{dy^4} = \frac{\Delta P}{D} \tag{3.13}$$

Where D is the isotropic flexural rigidity, which is given by

$$D = \frac{Et^3}{12(1-\gamma^2)} \tag{3.14}$$

Where E is Young's modulus, γ is Poisson's ratio and t is the thickness of the plate. The plate equation can then be solved using appropriate boundary conditions. In the following subsections analytical pressure deflection expressions for circular, rectangular, and square plates are provided along with the corresponding relation between leak rate and deflection rate.

3.2.1. Leak rate expression for circular shaped membrane

For a circular membrane, an exact pressure-deflection solution is available. Expressed in cylindrical coordinates, the static deflection w(r) for a thin circular membrane with radius (a), clamped at the periphery [34] is:

$$w(r) = w_0 \left[1 - (\frac{r}{a})^2\right]^2 \tag{3.15}$$

Assuming that the boundary conditions are given by ∂w(0)/∂r=0, ∂ w(a)/∂r=0, w(a)=0,and that the center deflection, w(0) is finite. The center or maximum deflection is given by:

$$Z = w_0 = w(0) = \frac{\Delta P a^4}{64D} \tag{3.16}$$

The above expression is only valid when the plate deflection is sufficiently small compared to the plate thickness such that stress stiffening effects can be ignored.

By differentiating eq.(3.16):

$$\frac{dZ}{dt} = \frac{a^4}{64D}(\frac{d\Delta P}{dt}) \tag{3.17}$$

In order to relate deflection rate (dZ/dt) and leak rate (dN_{in}/dt), eq.3.9 is used, which is converted into (dΔP/dt) form in left side of the equation. This conversion is by done using linear relation between ΔP and Z, as given in eq.3.6. Therefore the expression relating (dΔP/dt) and (dN_{in}/dt) is given by:

$$(-\frac{d\Delta P}{dt}) = (\frac{dN_{in}}{dt})(\frac{RT}{V_{eff}}) \tag{3.18}$$

Substituting, eq.3.18 in eq.3.17, gives the relation between leak rate and deflection rate for the circular membrane.

$$-\frac{dZ}{dt} = (\frac{a^4}{64D})(\frac{RT}{V_{eff}})(\frac{dN_{in}}{dt}) \tag{3.19}$$

3.2.2. Leak rate expression for rectangular and square shaped membranes

For rectangular and square plates an exact solution to the plate differential equation does not exist. Instead, approximate solutions based on series expansions are normally used. The center deflection (Z) of a clamped plate having the length (a) and width (b), exposed to a uniform load, ΔP is given by:

$$Z = \frac{\Delta P b^4}{\alpha D} \tag{3.20}$$

Where α varies depends on the aspect ratio (a/b) [35]. Values for α are summarized in the table 3.1.

Table 3.1: Values of α for different aspect ratios

a/b	1.0	1.2	1.4	1.6	1.8	2.0	∞
α	795.524	580.581	483.185	435.039	408.988	394.223	384.507

By following the same differentiation as did in the eq.(3.17) and followed by substitution of eq.(3.18) gives rise to the relation between leak rate and deflection rate for the square and rectangular plate.

$$-\frac{dZ}{dt} = (\frac{b^4}{\alpha D})(\frac{RT}{V_{eff}})(\frac{dN_{in}}{dt}) \tag{3.21}$$

3.2.3. Comparison of deflection rates for circular-rectangular-square membranes

Having derived the leak rate expressions for all 3 membrane shapes, in this subsection, the comparison of leak rate measuring capabilities of all 3 membrane shapes is done and is shown in steps.

Step-1: As a first step, all the leak rate expressions are converted to dZ/dN (in nm/mol) form to enable easy comparison. Table.3.2 shows the expression for all types of membranes.

Table 3.2: Deflection rate expressions for circular-square-rectangular plates in the dZ/dN form

Circle	Square	Rectangle
$\frac{dZ}{dN_{in}}$ = (-$\frac{a^4}{64DV_{eff}}$) (RT)	$\frac{dZ}{dN_{in}}$=(-$\frac{b_1^4}{795.524DV_{eff}}$) (RT)	$\frac{dZ}{dN_{in}}$=(-$\frac{b_2^4}{\alpha DV_{eff}}$)(RT)

Step-2: In this step, all the dZ/dN expressions are shown in the form of a ratio.

$$\frac{dZ}{dN_{in}} = (\frac{a^4}{64DV_{eff}})(RT) : (\frac{b_1^4}{795.524DV_{eff}})(RT) : (\frac{b_2^4}{\alpha DV_{eff}})(RT) \tag{3.22}$$

Here b_1 corresponds to the length(or)width of the square and b_2 corresponds to the width of the rectangle. Now, by assuming the same effective volume (V_{eff}), flexural rigidity (D), and temperature (T), the ratio of dZ/dN_{in} reduces to:

$$\frac{a^4}{64} : \frac{b_1^4}{795.524} : \frac{b_2^4}{\alpha} \tag{3.23}$$

Step-3: In the final step, the factors of eq.3.23 are compared based on a value assigned for the geometrical parameters.

By considering a diameter (2a) of 500 µm, the cross-sectional area of the cavity is $1.96 \text{x} 10^5$ µm ^{2}. For the same area, the length and width (b_1) of the square is 443.11 µm. For the rectangle, by assuming a length of (a) is 500 µm, the width (b_2) becomes 392.70 µm. This gives an aspect ratio (a/b) of 1.27 and by using linear interpolation, the value of (α) is 546.66. Finally, this simplified the eq. 3.23 to:

$$6.10 \times 10^7 : 4.84 \times 10^7 : 4.35 \times 10^7 \tag{3.24}$$

This shows that **for the same effective cavity volume and for the same thickness of the membrane, circular membranes provide a higher deflection rate capability. Hence, the circular design is considered the suitable membrane shape for the test structure**.

3.3. Size Dependent Analysis

Having selected the circular membrane for the test cavity, in this section, different design values for diameter, thickness, and gap height are assigned, and calculated the leak rate (in the dN/dZ form) is to understand the order of values that resulted.

Leak-rate expression for circular membrane in dN_{in}/dZ form is given by:

$$\frac{dN_{in}}{dZ} = -(\frac{64D}{a^4})(\frac{V_{eff}}{RT}) \tag{3.25}$$

For this analysis, V_{eff} is assumed constant, and the membrane is assumed to be deflected in the downward direction under P_{ext} equivalent to atmospheric pressure of 1 atm and with 0 pressure inside the cavity. The deflected membrane is assumed paraboloid in shape, therefore the value of c1 is considered as 1/2. Assumed values of E and γ are 128 GPa and 0.28 respectively. Critical parameters in V_{eff} such as area (A), stiffness (K), and deflection (Z) are calculated according to the considered design parameters (Table.3.3). Calculated values of A, K, and Z are shown in tables.3.4, 3.5 and 3.6 respectively.

Table 3.3: Design parameters

Design Parameters	Values	Units
Diameter	500,1000,2000	µm
Thickness	25,50,100	µm
Gap height	10,100,250,450	µm

Table 3.4: Calculated area (A) for considered diameters

Diameter (µm)	Area (µm^2)
500	$1.96 \text{x} 10^5$
1000	$7.85 \text{x} 10^5$
2000	$3.14 \text{x} 10^6$

Table 3.5: Calculated value of stiffness (in N/µm) for different diameter and thickness values

Diameter(µm)/Thickness(µm)	25	50	100
500	0.60	4.80	38.30
1000	0.15	1.20	9.57
2000	0.04	0.30	2.40

Table 3.6: Deflection (Z) of the membrane (in µm) at atmospheric pressure of 1 atm

Diameter(µm)/Thickness(µm)	25	50	100
500	0.03	0.004	$5.12x10^{-4}$
1000	0.52	0.06	0.008
2000	8.4	1.05	0.13

For each gap height, dN_{in}/dZ (in mol/nm) are summarized in the following tables 3.7,3.8,3.9 and 3.10.

Table 3.7: dN_{in}/dZ for gap height - 10um

Diameter(µm)/Thickness(µm)	25	50	100
500	$-2.45x10^{-12}$	$-1.96x10^{-11}$	$-1.57x10^{-10}$
1000	$-5.97x10^{-13}$	$-4.89x10^{-12}$	$-3.93x10^{-11}$
2000	**$-8.98x10^{-14}$**	$-1.16x10^{-12}$	$-9.75x10^{-12}$

Table 3.8: dN_{in}/dZ for gap height - 100um

Diameter(µm)/Thickness(µm)	25	50	100
500	$-2.45x10^{-11}$	$-1.96x10^{-10}$	$-1.57x10^{-9}$
1000	$-6.12x10^{-12}$	$-4.90x10^{-11}$	$-3.93x10^{-10}$
2000	**$-1.47x10^{-12}$**	$-1.22x10^{-11}$	$-9.81x10^{-11}$

Table 3.9: dN_{in}/dZ for gap height - 250um

Diameter(µm)/Thickness(µm)	25	50	100
500	$-6.13x10^{-11}$	$-4.91x10^{-10}$	$-3.93x10^{-9}$
1000	$-1.53x10^{-11}$	$-1.22x10^{-10}$	$-9.82x10^{-10}$
2000	**$-3.77x10^{-12}$**	$-3.06x10^{-11}$	$-2.45x10^{-10}$

Table 3.10: dN_{in}/dZ for gap height - 450um

Diameter(µm)/Thickness(µm)	25	50	100
500	$-1.03x10^{-10}$	$-8.83x10^{-10}$	$-7.07x10^{-9}$
1000	$-2.76x10^{-11}$	$-2.20x10^{-11}$	$-1.76x10^{-9}$
2000	**$-6.84x10^{-12}$**	$-5.51x10^{-11}$	$-4.41x10^{-10}$

By considering different design parameters for test cavities, it could be observed that cavities with large diameters with small thicknesses and gap heights can provide sensitive leak rate detection.

3.4. Prediction of Plastic deformation

Since the silicon membranes are going to be fusion-bonded and subjected to the subsequent annealing process at temperatures above 1000 ^{o} C under atmospheric pressure, there is a thought that this high temperature would add to the risk of elastic failure of membranes. In general, silicon undergoes brittle-to-ductile transition at temperatures between 520 ^{o} C and 600 ^{o} C [36], during this stage the silicon membranes are susceptible to creep.

To observe this plastic deformation phenomenon Ren, Juan, et al. investigated the mechanical behavior of pressurized silicon diaphragms of different diameters, which were annealed at the temperature range of 600° C-900° C under the presence of atmospheric pressure [37]. The evolution of the deformation was obtained by studying the surface profiles at different time periods for a particular annealing temperature. Their corresponding experimental results revealed that for a specific thickness, larger diameter diaphragms have a higher plastic deformation such that the maximum deflection after annealing is observed to be larger than the deflection before annealing. Based on that the proposed hypothesis was, when it comes to creep, raising the temperature increases the diffusion rate of silicon atoms in the pressurized membranes and therefore speeds up the creep progress, which might eventually cause the membranes to likely plastically form in a high-temperature environment.

Hence, to finalize an optimal design for the test cavity a prior plastic deformation analysis needs to be done which would provide the ideal diameter for the given thickness of the membrane. In order to check the occurrence of plastic deformation in silicon membranes, a stress analysis is performed using COMSOL Multiphysics. The geometrical model, boundary conditions, material model, and criteria for checking the plastic deformation considered for this model are explained in the following subsections.

3.4.1. Geometrical model

Since the considered type of membrane is circular in shape, which is symmetrical, therefore the analysis is conducted in the 2D axis-symmetric domain. In the model (as shown in Fig.3.2) a 2D-rectangular plane is created representing the silicon membrane. By varying the length of the rectangular plane, the radius of the membrane is varied, and the thickness of the plane corresponds to the thickness of the membrane.

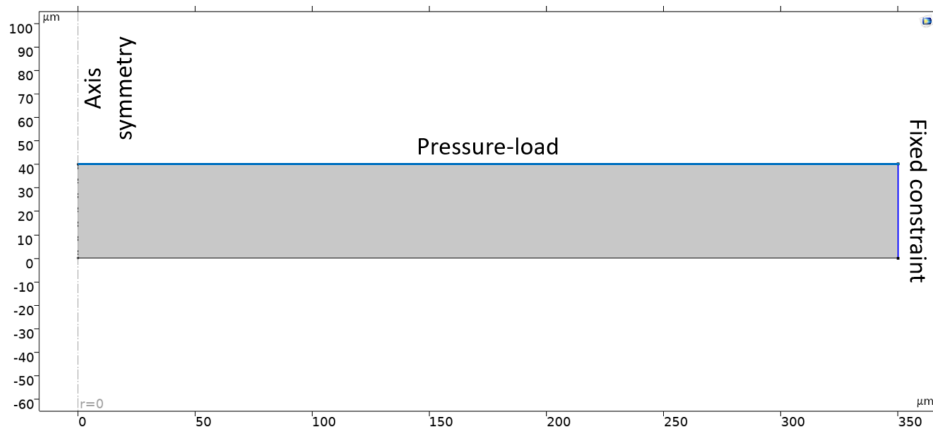

Figure 3.2: 2D Axisymmetric model created in the simulations for membrane having a radius of 350 µm

3.4.2. Boundary conditions

To the left edge, the axis-symmetry boundary condition is applied and a fixed constraint is provided to the right edge of the membrane. Since the annealing process in fusion bonding takes place at atmospheric pressure, therefore 1 bar is considered as the pressure load applied on the top surface of the membrane.

3.4.3. Material model

Silicon is an anisotropic material. The relation between stress and strain is given by the stiffness tensor C.

$$\sigma_{ij} = C_{ijkl}\epsilon_{kl} \tag{3.26}$$

In theory, there are 81 variables in C. For silicon, there are only 3 independent variables in elasticity tensor, due to equivalence of shear conditions and cubic symmetry. The relation between stress and strain for silicon can be seen in eq.(3.27).

$$\begin{bmatrix}\sigma_{11}\\ \sigma_{22}\\ \sigma_{33}\\ \sigma_{23}\\ \sigma_{31}\\ \sigma_{12}\end{bmatrix} = \begin{bmatrix} C_{11} & C_{12} & C_{12} & 0 & 0 & 0\\ C_{12} & C_{11} & C_{12} & 0 & 0 & 0\\ C_{12} & C_{12} & C_{11} & 0 & 0 & 0\\ 0 & 0 & 0 & C_{44} & 0 & 0\\ 0 & 0 & 0 & 0 & C_{44} & 0\\ 0 & 0 & 0 & 0 & 0 & C_{44}\end{bmatrix} \begin{bmatrix}\epsilon_{11}\\ \epsilon_{22}\\ \epsilon_{33}\\ \epsilon_{23}\\ \epsilon_{31}\\ \epsilon_{12}\end{bmatrix} \tag{3.27}$$

Where C_{11}=164 Gpa, C_{12}=64 Gpa and C_{44}=80 Gpa at room temperature (20 ^{o} C).

If the stress-strain relation is needed in a different direction, the tensor must be rotated using tensor transformations, so that one of the axes is aligned with the desired direction. There are shortcut formulas to calculate values for Young's modulus (E) and Poisson's ratio (γ) for common cases. In general, there are 3 crystallographic directions in silicon: <100>, <110>, and <111>, and formulas to calculate E along these directions are provided in Eq.(3.28),(3.29) and (3.30) respectively.

$$E_{<100>} = \frac{(C_{11} - C_{12})(C_{11} + 2C_{12})}{(C_{11} + C_{12})} \tag{3.28}$$

$$E_{<110>} = 2/[(\frac{C_{11}}{(C_{11} - C_{12})(C_{11} + 2C_{12})}) + (\frac{1}{2C_{44}})] \tag{3.29}$$

$$E_{<111>} = 3/[(\frac{1}{C_{11} + 2C_{12}}) + (\frac{1}{C_{44}})] \tag{3.30}$$

Formula to calculate Poisson's ratio along <100> direction is given in eq.3.31.

$$\gamma_{<100>} = \frac{C_{12}}{C_{11} + C_{12}} \tag{3.31}$$

In this model, silicon membranes are considered to be aligned with <100> directions as it is mostly preferred for photolithography and device processing. For simplifying the analysis, the material property is assumed to be isotropic. Calculated values of E<100> and γ<100> at room temperature are 128 Gpa and 0.28 respectively. The elasticity modulus is slightly dependent on the temperature, therefore Young's modulus in this model is used as a function of annealing temperature. The temperature-dependent Young's modulus of silicon used in this model is obtained from the data measured by Vanhellemont et al [38]. for temperatures ranging from 20 ^{o}C to 1400 ^{o}C. Fig.3.3 shows the values E<ijk> along the <100>, <110> and <111> crystallographic directions.

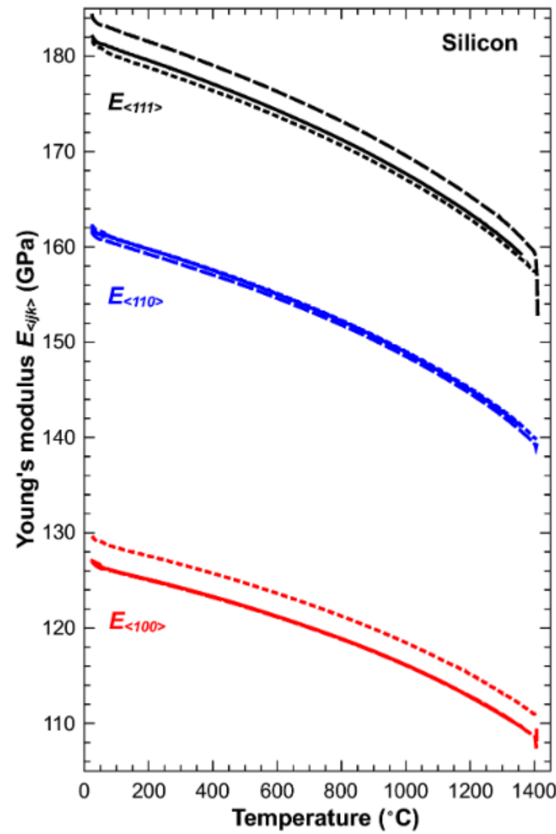

Figure 3.3: E<ijk> along the <100>-, <110>- and <111>-crystallographic directions for three Si samples measured by Vanhellemont et al.[38]

For analysis, different annealing temperatures are considered, which include 700,800,900 and 1000 ^oC. According to these temperatures, corresponding values of E<100>, E<110>, and E<111> are obtained from the graph (as shown in the Fig.3.3) and solved the non-linear eq.(3.28),(3.29) and (3.30) using Matlab to obtain solutions for C_{11}, C_{12}, C_{44} and poisson's ratio γ<100>.

Values of E<100>, E<110>, and E<111> and calculates values of C_{11}, C_{12}, C_{44} and γ<100> for considered annealing temperatures are summarized in the Table. 3.11.

Table 3.11: Material properties at each annealing temperature

Temperature (deg C)	**E<100> GPa**	E<110> GPa	E<111> GPa	C_{11} GPa	C_{12} GPa	C_{44} GPa	γ **<100>**
700	**123**	154	175	152.26	56.31	73.88	**0.27**
800	**121**	152	173	151.02	56.91	72.81	**0.274**
900	**120**	151	172	150.41	57.23	72.27	**0.276**
1000	**118**	148	170	148.89	57.76	71.03	**0.278**

3.4.4. Mesh

Since the geometrical model is rectangular in shape, therefore to accommodate this shape, a quadrilateral mesh was preferred (Fig.3.4). Here, an ***extremely fine*** element size to provide as much accurate results. The chosen element size parameters are as follows: maximum element size: 4μm, minimum element size: 0.007 μm, curvature factor: 0.2.

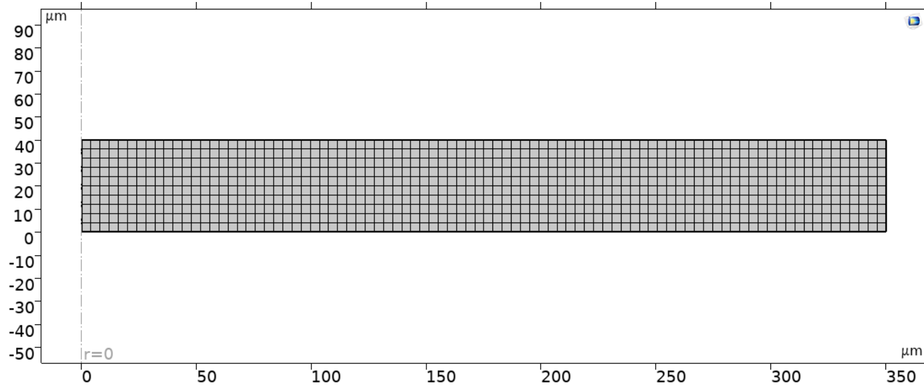

Figure 3.4: Quad mesh for the geometrical model having a radius of 350μm

3.4.5. Criteria for checking plastic deformation

As silicon undergoes brittle to ductile transition at elevated temperatures and the material property is considered isotropic, therefore the von-mises yield criteria is considered the best criterion for checking the plastic deformation.

Von-mises criterion is based on the determination of the distortion energy in a given material i.e., of the energy associated with changes in the shape in that material (as opposed to the energy associated with the changes in the volume in the same material). According to this criterion, a given material is safe as long as the maximum value of the distortion energy per unit volume in that material remains lesser than the distortion energy per unit volume required to cause yield in a tensile test specified of the same material.

Mathematically, the yield function for the von-Mises condition is expressed as:

$$f(J_2) = J_2 - k^2 = 0 \tag{3.32}$$

Where k is the material's yield stress in pure shear. The magnitude of yield stress in pure shear is $\sqrt{3}$ times lower than the yield stress in tension (σ_{yield}):

$$k = \frac{\sigma_{yield}}{\sqrt{3}} \tag{3.33}$$

If we set the von Mises stress (σ_v) equal to the yield strength and combine the above equations, the von Mises yield criterion is written as:

$$\sigma_v = \sigma_{yield} = \sqrt{3J_2} \quad or \quad \sigma_v^2 = 3J_2 = 3k^2 \tag{3.34}$$

The term J_2 is called the second-deviatoric stress invariant (stress component responsible for changing the shape of the material), which is given by:

$$J_2 = \frac{1}{6}[(\sigma_{11} - \sigma_{22})^2 + (\sigma_{22} - \sigma_{33})^2 + (\sigma_{33} - \sigma_{11})^2 + 6(\sigma_{23}^2 + \sigma_{31}^2 + \sigma_{12}^2)] \tag{3.35}$$

Here, σ_{11},σ_{22}, σ_{33},σ_{12},σ_{23}, σ_{31} are components of stress tensor. Substituting the eq.3.35 in eq.3.34, we have:

$$\sigma_v = \frac{1}{\sqrt{2}}\sqrt{[(\sigma_{11} - \sigma_{22})^2 + (\sigma_{22} - \sigma_{33})^2 + (\sigma_{33} - \sigma_{11})^2 + 6(\sigma_{23}^2 + \sigma_{31}^2 + \sigma_{12}^2)]} = \sigma_{yield} \tag{3.36}$$

According to eq.3.36, plastic deformation occurs when von-mises stress (σ_v) exceeds the yield strength of the material (σ_{yield}). In COMSOL, von Mises stress (σ_v) is generated by default.

3.4.6. Occurrence of Plastic deformation

With the developed FEM model, it was observed that maximum von-mises stress occurred at the edge of the membrane, as shown in Fig.3.5. Here, the considered membrane thickness is 40 µm. The onset of plastic deformation is predicted by comparing the maximum of occurred von-mises stress with the yield strength of silicon at different annealing temperatures, as shown in Fig.3.7. The yield strength used in this model is obtained from the data measured by Patel, J.R., and A.R.Chaudhuri [39], especially the data corresponding to the strain-rate of 5 x 10^{-3} cm/min (Fig.3.6) to cover a range of temperatures.

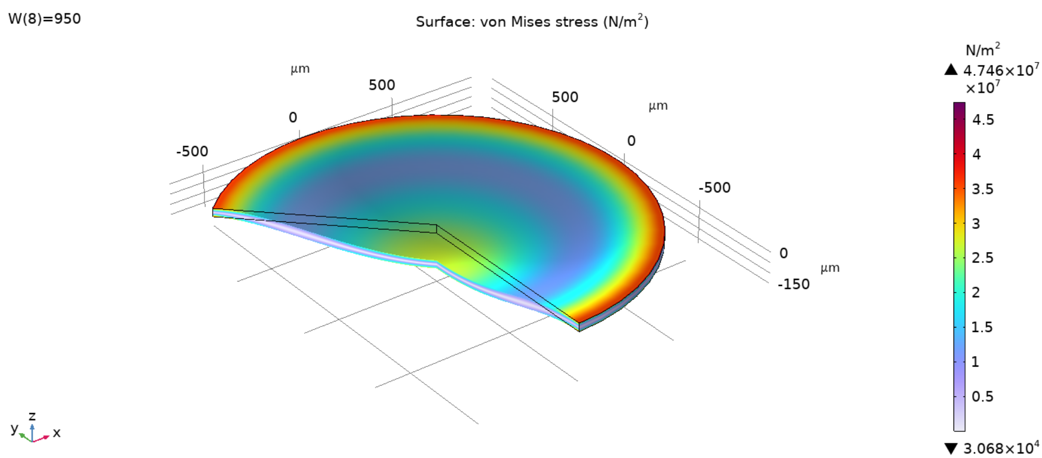

Figure 3.5: Distribution of von-mises stress (in Mpa) when the membrane diameter is 1900 µm

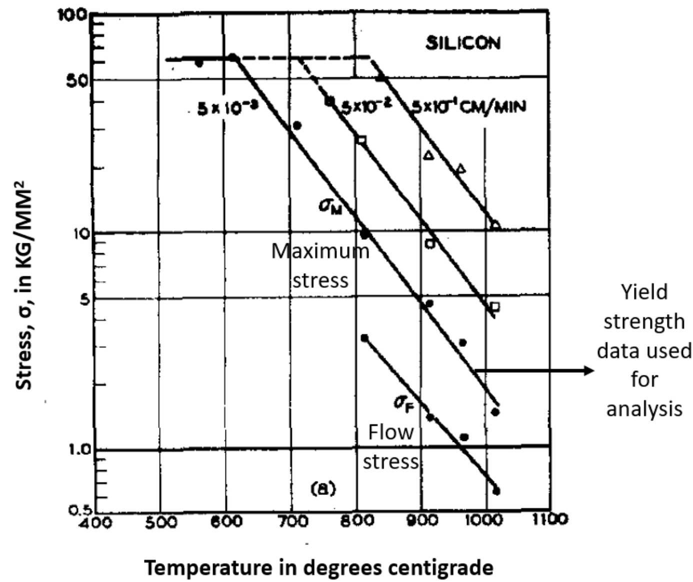

Figure 3.6: Temperature dependence of maximum and flow stress in silicon [39]

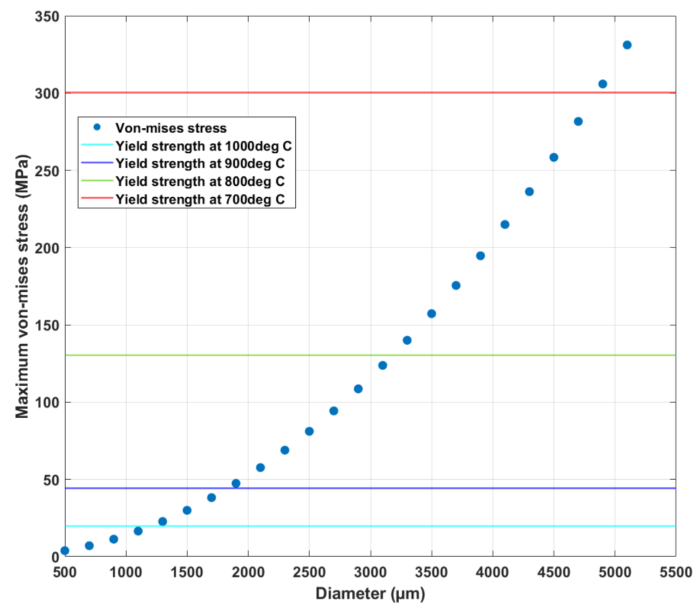

Figure 3.7: Plot of maximum von-mises stress as a function of membrane diameter (comparison of maximum von-mises stress with yield strength)

It was observed that maximum von-mises stress varied from 4 to 330 MPa for diameters ranging from 500 to 5100 µm. Consequently, not all the membranes would get plastically deformed at all temperatures. At 700 ^{o}C, the yield strength is 300 MPa, and according to that the plastic deformation would have happened for diameters above 4800 µm. At 800 ^{o}C, yield strength decreases to about 130 MPa. At this temperature, diameters greater than 3400 µm were expected to plastically deform. At 900 ^{o}C, yield strength decreases further to 45 MPa, and diameters above 1800 µm were likely to deform. When the operating temperature increases to 1000 ^{o}C, the plastic deformation can be serious for diameters larger than 1200 µm.

The results of plastic deformation analysis suggest that the higher the operating temperature and the large the membrane diameter, the more likely the plastic deformation is. In order to test this hypothesis, it was decided to consider test cavities with membranes that have a thickness of 40 µm and diameters of 300, 500, 700, 900, 1100, 1300, 1400, 1600, and 2000 µm. Along with this, the considered annealing temperature for test structure fabrication is 1000 ^{o} C.

3.5. Collapsing of membrane

Having selected diameters for membranes for a given thickness, in this final section, the gap height for the cavity is selected.

Once wafers are bonded in the vacuum, they are annealed at atmospheric pressure conditions, during that stage when the deflection of the membrane is greater than the gap height, it is expected that the membrane would collapse with the base of the substrate, as illustrated in Fig.3.8.

Therefore, to choose a gap height, the deflection of selected membranes at 1 atm pressure difference is first calculated and provided in the table 3.12. Here the calculations are based on Young's modulus and Poisson's ratio accounting for the annealing temperature of 1000 ^{o}C.

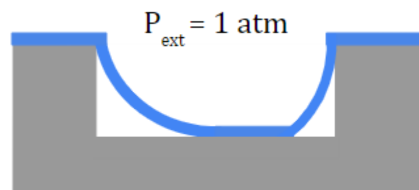

Figure 3.8: Illustration of a collapsing membrane with substrate base when deflection > gap height

Table 3.12: Deflection of membranes (in nm) at 1 atm external pressure - Thickness 40 µm

Diameter (µm)	Deflection at 1 atm (nm)
2000	2290.90
1600	983.35
1400	550.04
1300	408.94
1100	209.63
900	93.94
700	34.38
500	8.95
300	8.95

Since 2000 µm has the highest deflection of 2290 nm, therefore the corresponding deflection value is considered as the suitable gap height for all the diameters. **Hence to avoid collapsing of the membrane with the substrate, gap height corresponding to deflection of the 2000 µm diameter membrane at 1 atm pressure is considered, which is equivalent to 2.3 µm**.

4

Experimental Method

4.1. Digital Holographic Microscope

To measure the deflections of membranes, digital holographic microscopy (DHM) is employed. It is a quantitative phase microscopy technique which has been has been extensively used for a variety of applications including static and dynamic surface metrology [40]–[42], particle tracking [43], [44], tracking and monitoring of live biological cells [44]–[46].

Interferometric principles provide the basis of DHM. A coherent, monochromatic light source is split into objects and reference beams. The object beam passes through an objective lens, interacts with the sample surface, and is reflected through the objective lens, where it is recombined with the reference beam (as shown in Fig.4.1). The interferogram produced by the recombined object and reference beams is recorded as a 2D hologram on a charge-coupled device (CCD) camera [46], [47]. The hologram effectively is a complex superposition of interferograms each formed by a reflecting wave from a point on the object's surface and interfering with the reference wave. Thus, the hologram contains all phase and amplitude information of the specimen.

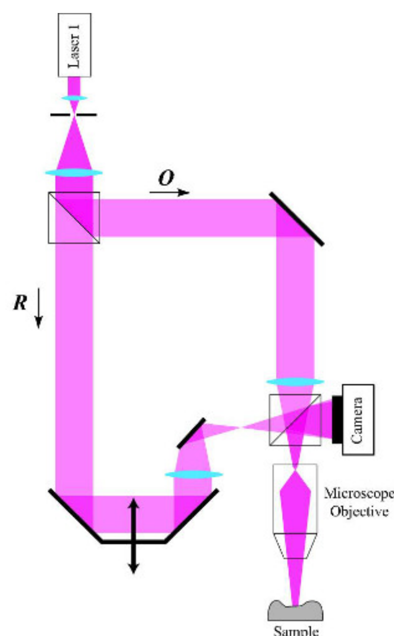

Figure 4.1: Basic optical configuration of DHM in reflection geometry to measure height profiles [48]

Numerical reconstruction of the hologram produces a reconstruction wavefront in an observation plane as a function of the recorded hologram intensity. This reconstructed wavefront consists of real and imaginary parts, from which a 2D amplitude image (similar to what would be observed in a conventional-light microscope) and a 2D Phase image are generated [49]. Additional processing accounts for aberrations and the shape (e.g., tilt) of the sample surface [47], [50]. The phase ϕ at a given pixel (ξ,η) in the image can be converted to height h, as a function of the known wavelength λ and the index of refraction [51], as shown in eq.(4.2).

$$h(\xi,\eta) = \frac{\lambda}{4\pi n}\phi(\xi,\eta) \tag{4.1}$$

The DHM utilized in this project was a Lyncée Tec DHM R2200, shown in Fig.(4.2).

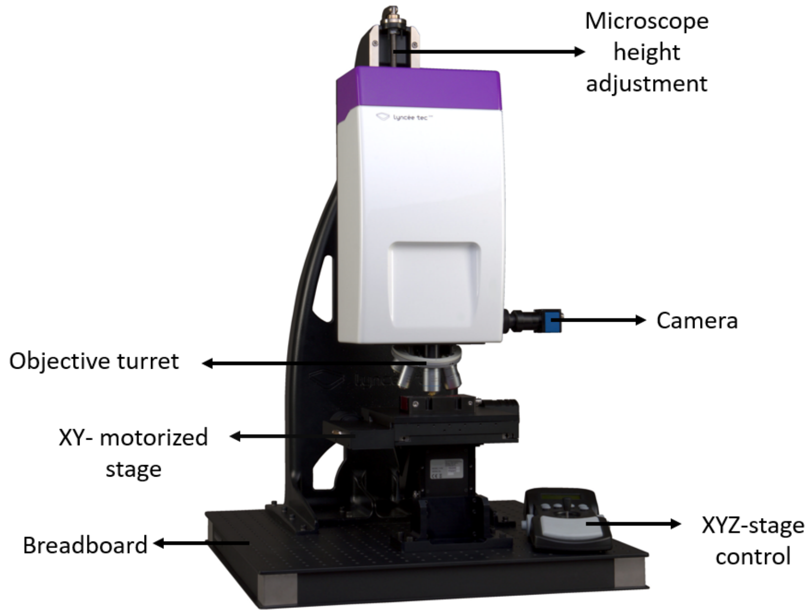

Figure 4.2: Lyncée Tec DHM

The instrument is equipped to produce three different wavelengths. The instrument is equipped to produce three different wavelengths (λ_1 = 665.5651 nm, λ_2 = 793.2365 nm, or λ_3 = 681.0068 nm) and can be operated in a single-wavelength (λ_1 only) or dual-wavelength (λ_1 and λ_2 or λ_1 and λ_3) mode. In our case, single wavelength mode was sufficient enough to acquire the deflection profiles, and the objective lens used in the DHM configuration for this study is summarized in table 4.1.

Table 4.1: DHM objective lens details

Magnification	Lens description	Lens type	Numerical aperture	Working distance (mm)
2.5 x	Leica N Plan 2.5x/0.07	Air	0.07	11.2

4.2. Steps for deflection measurement

Lyncée Tec has an in-built software called *Koala*. The Koala software is an application written in C++.net for Windows. It allows the interpretation of the holograms captured by the DHM and makes intensity and phase measurements on the observed sample. It also includes other tools, which can be used to obtain deflection profiles of the test specimen. In this section, a detailed description of obtaining deflection profiles and the value of maximum deflection is explained in a step-by-step approach with the measurement of the test specimen.

1) **Koala interface**: Lyncée Tec has a power supply unit for the microscope and motorized stage, which needs to be powered ON before initiating the measurements. Then, the Kola icon has to be clicked to start the software.

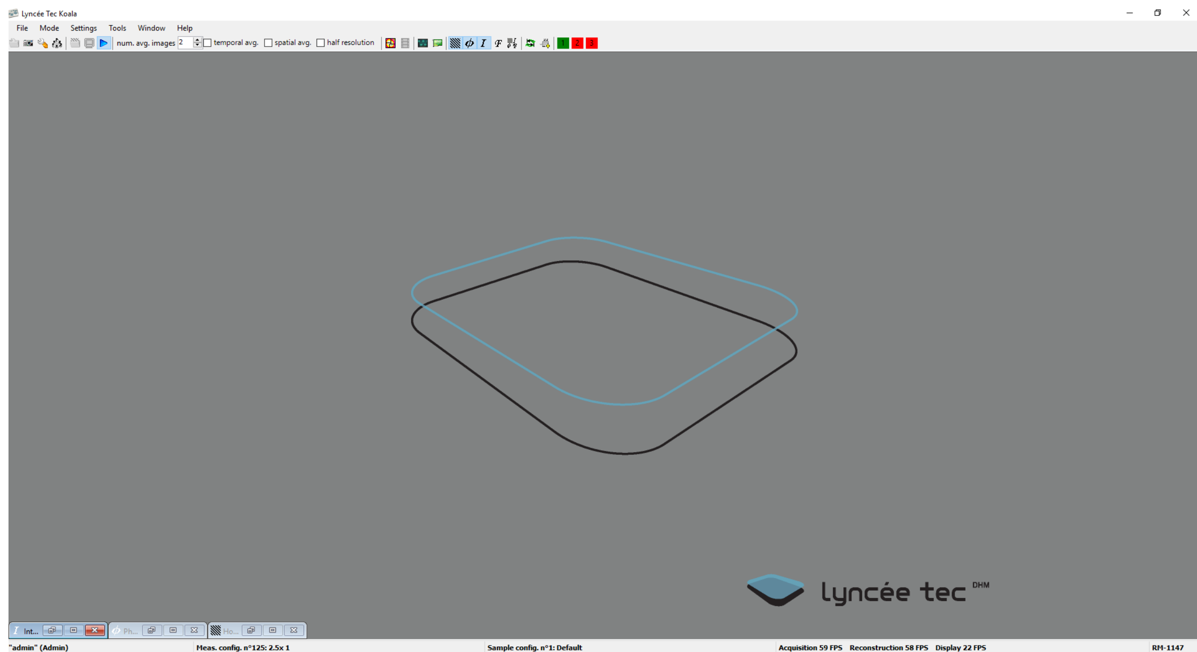

Figure 4.3: Main window of Koala

The main window of the Koala is shown in Fig.4.3. It is divided into three main parts:

- *Menu bar*, as shown in Fig.4.4 is composed of seven drop-down menus on the top line (FILE, MODE, SETTINGS, OPTIONS, TOOLS, and HELP), and the icon buttons (shortcuts and commands) on the lower bar.

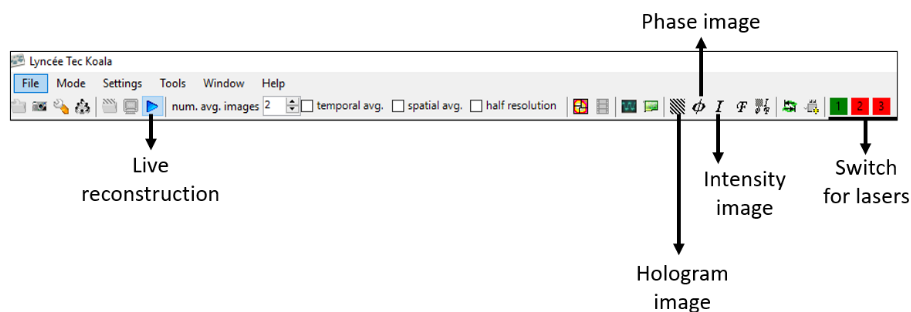

Figure 4.4: Menu bar of Koala

- Main section, empty when the program is started, is used to display the hologram presentation windows, phase, and intensity measurements.

- *Status bar*, as shown in Fig.4.5. It is composed horizontally of 4 fields from right to left.
Status: It indicates that the microscope is operational. If an error occurs, it is signaled in the first field.
Name of the current configuration
Acquisition rate is shown when the camera is in use.

"admin" (Admin) | Meas. config. n°125: 2.5x 1 | Sample config. n°1: Default | Acquisition 56 FPS Reconstruction 56 FPS Display 22 FPS | RM-1147

Figure 4.5: Koala status bar

2) **Setting up of initial configuration**: After the main window is opened, first, a configuration need to be selected for chosen objective and wavelength of the laser source. This can be opened with the command - *Open configuration* in the FILE menu. DHM offers standard factory configurations, which can be neither deleted nor modified. Once the open configuration is selected, the command opens a dialog box (Fig.4.6), from which the desired configuration can be chosen. Only one configuration may be open at a time. In our case, the selected configuration corresponds to 2.5x magnification and laser source with wavelength: 665.5651 nm .

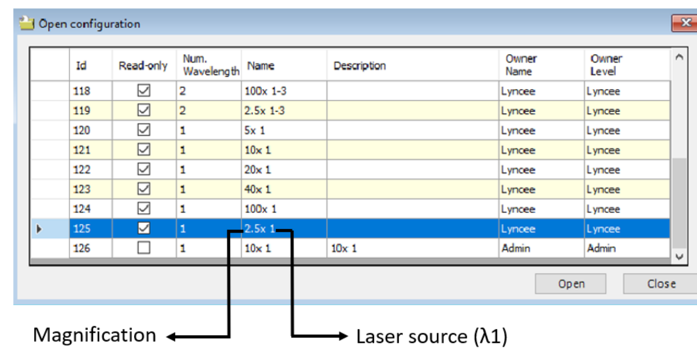

Id	Read-only	Num. Wavelength	Name	Description	Owner Name	Owner Level
118	☑	2	100x 1-3		Lyncee	Lyncee
119	☑	2	2.5x 1-3		Lyncee	Lyncee
120	☑	1	5x 1		Lyncee	Lyncee
121	☑	1	10x 1		Lyncee	Lyncee
122	☑	1	20x 1		Lyncee	Lyncee
123	☑	1	40x 1		Lyncee	Lyncee
124	☑	1	100x 1		Lyncee	Lyncee
125	☑	1	2.5x 1		Lyncee	Lyncee
126	☐	1	10x 1	10x 1	Admin	Admin

Figure 4.6: Open configuration menu

3) **Hologram acquisition**: Once a suitable configuration is selected, an appropriate functional mode of the Koala program needs to be selected, to start analyzing the test specimen. The command *Live reconstuction* in the main window allows real-time working, that is acquire holograms and rebuild continuously phase and intensity images. When the live reconstruction mode is activated, images are directly recorded by the camera, that is the hologram formed by the DHM (Fig.4.7).

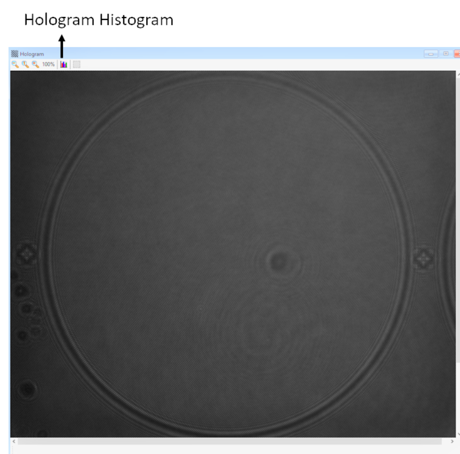

Figure 4.7: Hologram image of a membrane having a diameter of 2000μm

4) **Intensity image**: DHM can obtain two types of sample representation: one is the intensity or amplitude contrast image and another one is the phase or phase contrast image. Intensity images are the same images as those given by a classical optical microscope. It must, however, be noted that the intensity images are obtained by illuminating the sample with a monochromatic source (laser) and not with white light (i.e., a full spectrum of visible wavelengths) and cannot, therefore, give information about the color of the sample. Nevertheless, it gives information about how much the sample is focused on.

Intensity image can be obtained using the intensity icon *I* available in the menu bar (Fig.4.4). When the intensity image is opened, there is a large chance of having an image as shown in Fig.4.8. This means that the sample is not sufficiently focused.

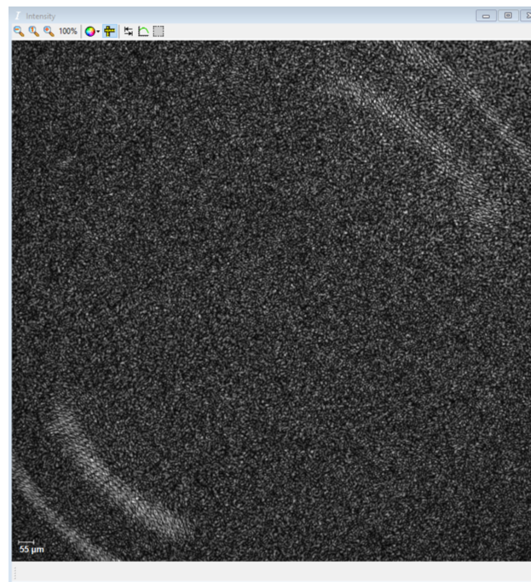

Figure 4.8: Intensity image when the focus is very less

To increase the focus on the sample, the DHM objective need to be moved closer to the sample. This can be manually done by rotating the screw head available at the backside of the microscope or by using the XYZ stage controller. Fig.4.9 shows a high contrast intensity image when a proper focus is achieved.

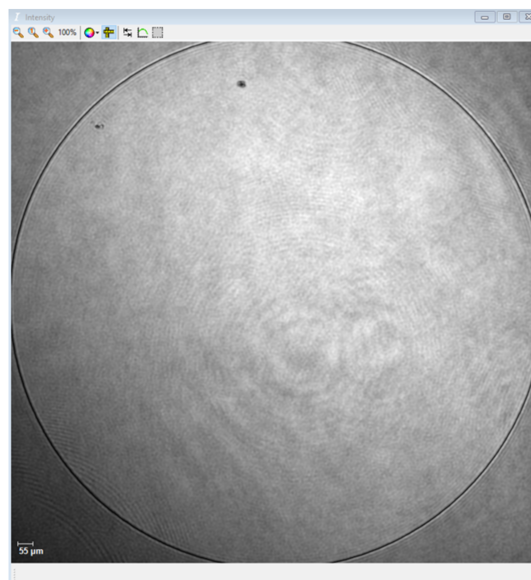

Figure 4.9: Intensity image with a maximum focus

5) **Phase image**: When the intensity image is correctly adjusted, the phase image of the sample can be analyzed to obtain the deflection profile. This can be obtained from the phase window in the MENU bar (Fig.4.4).

Fig.4.10 illustrates the principle of phase measurement by DHM on a homogeneous reflective sample lit by a monochromatic plane wave of wavelength λ. The wavefront is deformed during the reflection of the sample. This deformation with respect to the incident wave, measured in degrees is called dephasing $\Delta\phi$ [52]. For a homogeneous sample, this dephasing is directly connected to the 3D topology of the sample by the eq.4.2:

$$\Delta h = \frac{\lambda \Delta \phi}{4\pi n} \tag{4.2}$$

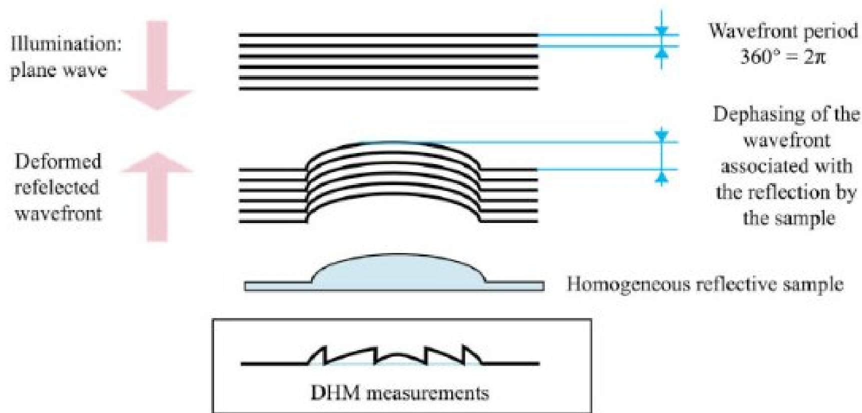

Figure 4.10: Principle of phase measurement in DHM

Where Δh is the height of the sample and n is the refractive index of the immersion medium (n=1 in the air). As common in interferometric metrology, when there are discontinuities in height, phase measurements yield discontinuities in the phase map. The phase map appears wrapped between -π and π for interferometric geometries. Therefore, DHM does not measure the real dephasing but the modulo 2π as given in the eq.4.3 [52]. This is similar to the topography as illustrated at the bottom of Fig.4.10.

$$\phi_{DHM} = \frac{\Delta h 4\pi n}{\lambda} mod 2\pi \tag{4.3}$$

For samples with a smooth enough topography, it is possible, using a mathematical technique called phase unwrapping supplied with the Koala software to recalculate the 3D wavefront topography, i.e., without the modulo 2π from the phase image captured by DHM.

To conclude on phase measurement, dephasing is a measure of the phase difference. It must be measured with respect to a reference plane normally defined as part of the sample. The Koala program has several options to define this reference plane and to adjust it digitally. This is referred to as digital tilt and phase offset adjustment.

7) **Digital tilt and Phase offset adjustment**: When the phase window is opened, there is a large probability that an image similar to the one shown in Fig.4.12 would be seen. This is because the reference plane of the microscope does not coincide with that of the sample. DHM can do this alignment digitally. Koala digitally matches the XY planes of two reference frames (angle α and angle β in Fig.4.11).

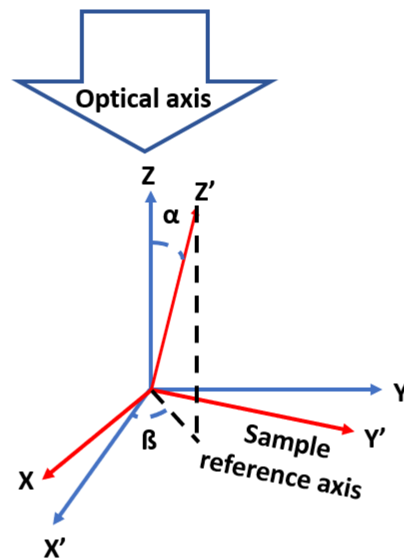

Figure 4.11: Reference Planes XYZ of the DHM and of the sample

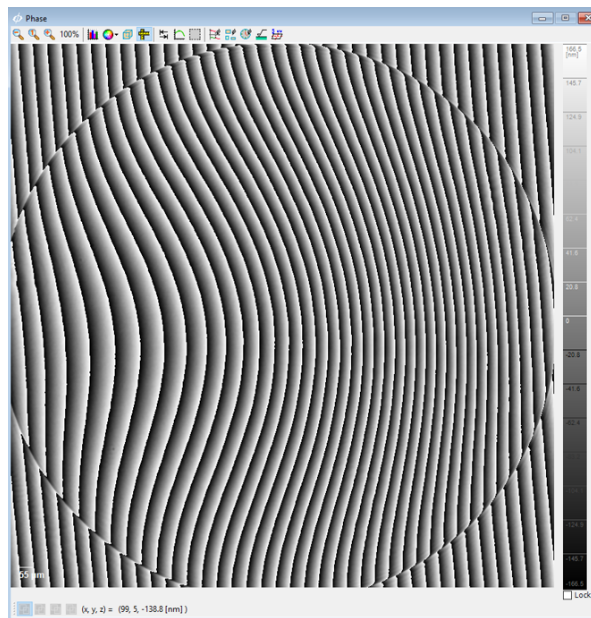

Figure 4.12: Phase window, when the sample is not coplanar with the reference plane of microscope

Practically, the phase measurement is made in two steps:

- Determination of the angles α and β between the microscope and sample reference planes, called the *tilt adjustment*.

A 3D topographic measurement needs to be defined relative to an orthogonal XYZ reference plane. XY plane of this referential is aligned relatively to the sample plane using the tilt correction tool. By default, Koala uses the fitting method 1D tilt to perform the tilt correction [53]. To execute this, the phase mask adjustment tool which is available at the top of the phase window must be selected (Fig.4.13). Tracing at least two orthogonal segments on a reference surface of the sample facilitates the koala to perform the tilt adjustment of the sample. The reconstructed phase image after the tilt adjustment is shown in Fig.4.13.

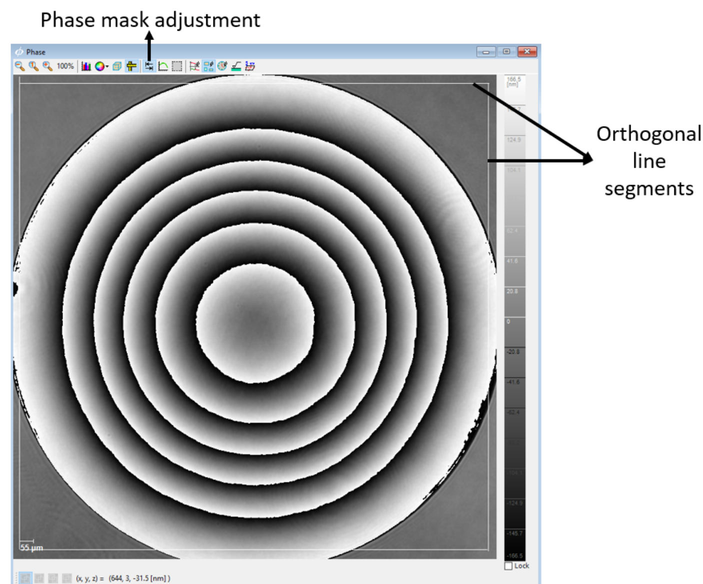

Figure 4.13: Phase window, when the sample is coplanar with the reference plane of microscope

- Adjustment of the origin of the reference frame to the optical axis (Z) or *offset adjustment*.

Once the sample's plane is aligned relative to the reference plane, there remains the origin of the plane (X=0, Y=0, Z=0) to be defined. In general, the origin of the Z (vertical) axis is set by defining an offset area with the tool phase offset adjustment available on the phase window (Fig.4.14). It defines the value of the Z-axis at a precise location. This also enables to compare successive measurements by having the same vertical reference for each of them individually. This is done by drawing surfaces or areas where the phase should be calculated. It is possible to define as many areas and the phase average will be calculated on these areas. The phase average will be calculated in these areas. It is always preferable to define the offset areas/surfaces on a flat part of the sample to use efficiently the fullest vertical range of the deflection measurement. If no zone is selected, Koala automatically adjusts the offset using the phase average calculated over all the regions of interest.

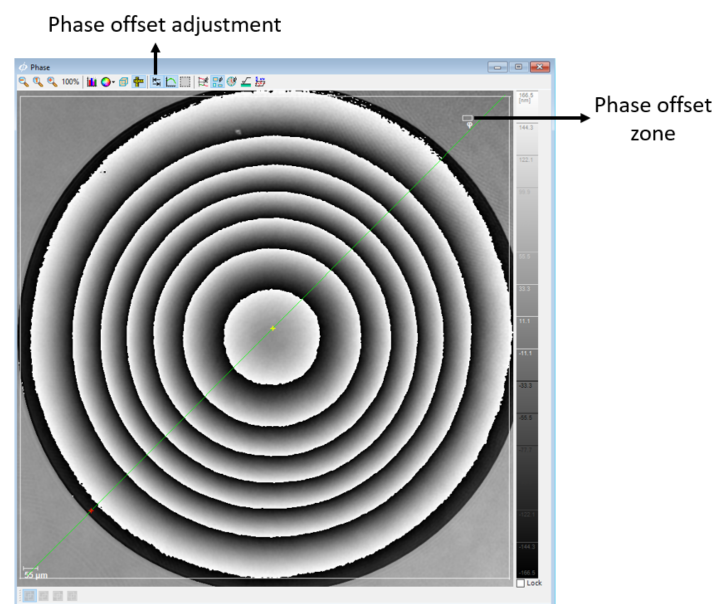

Figure 4.14: Phase window with phase offset defined

8) **Phase Unwrapping**: Once the phase image is obtained, it could be observed that there are contour lines in the phase map which are discontinuous (Fig.4.13). Phase measurements of surfaces with height discontinuities, yield phase discontinuities in the phase map. This is called phase jumps. Here the phase is wrapped and it can be visualized in the deflection profile. Using the 1D profile option from the same phase window, a deflection profile along a line can be obtained. Fig.4.15 shows the wrapped phase and corresponding 1D deflection profile.

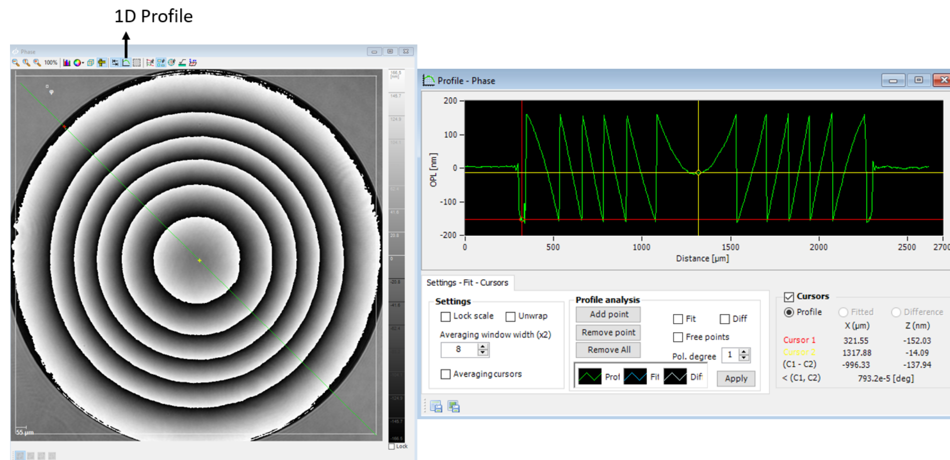

Figure 4.15: Wrapped phase image and corresponding 1D profile

Unwrapping is a mathematical transformation of the image. It provides good results when applying a region of interest with a continuously well-defined phase. There are two unwrapping methods available in Koala:

DCT unwrapping solves the unwrapping equation in the least-squares sense using the discrete cosine transform method. This method is computationally less-intensive and is sensitive to noise (location of the image without signal recorded from the sample) [54]. *Path following* method is another solver of the unwrapping equation, which supports user-defined masks and automatically generated quality masks. The path-following method starts the unwrapping of high-quality points and ends up with low-quality ones. This method is less sensitive to noise since noisy regions are filtered out by the masks [55]. This method is computationally expensive but more suitable for dynamic measurements.

Unwrapping algorithm can be selected using the *phase unwrapping* command from the SETTINGS menu. Once the method is selected, unwrapping can be executed by clicking the suitable icon in the phase window. Fig.4.16 shows the unwrapped phase image and the corresponding deflection profile.

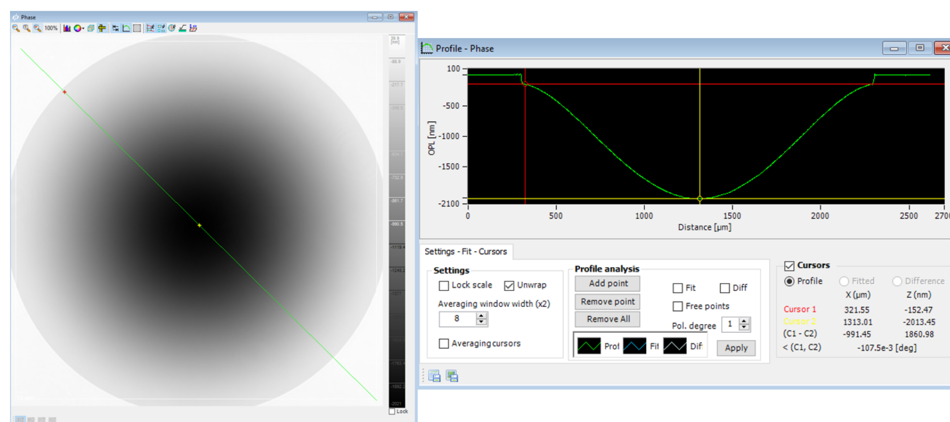

Figure 4.16: Unwrapped phase image and corresponding 1D profile

8) **Maximum deflection measurement**:

The 1D profile option from the phase window enables obtaining the deflection along a line, therefore to get a profile containing maximum deflection every time a line need to be drawn along different directions which ultimately becomes a trial and error method and time-consuming one. In addition, to get the magnitude of maximum deflection cursors in the profile window need to be moved accordingly to cover the full vertical range. If the deflection profile is not smooth, then the movement of the cursor becomes a cumbersome process and also questions whether the obtained magnitude is maximum or not. Thus, to avoid such conditions a MATLAB script was written to provide the actual deflection in one step.

To use the MATLAB script, the text (.*txt*) file of the unwrapped phase image is needed. The .*txt* contains unwrapped phase values for all pixels in the image. In addition to that it contains the information about no.of.pixels, pixel size, and the height conversion factor. The height conversion factor corresponds to the value of $\lambda/4\pi$n (as shown in eq.4.2) to get the actual deflection points. In our case, the value of the height conversion factor is 52.96 nm (with λ:665.5651 nm and n:1). On multiplying the height conversion factor with the unwrapped phase value, the actual deflected profile of the sample can be obtained. Fig.4.17 shows the MATLAB plot of the deflected sample obtained using the unwrapped phase image.

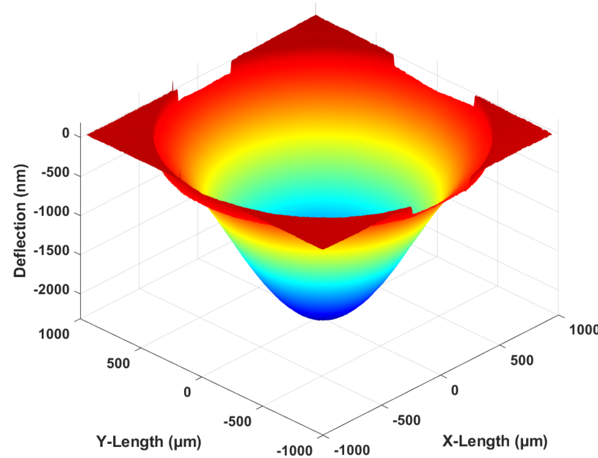

Figure 4.17: 3D profile of deflected sample having a diameter of 2000 µm

Once the .*txt* file is loaded into the code, a procedure is followed to obtain the actual value of deflection as shown in Fig.4.18. The source code is provided in the Appendix.C.

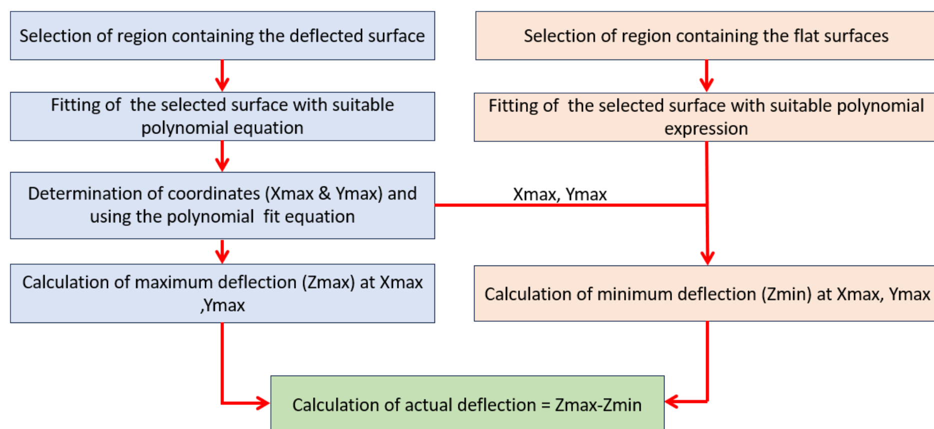

Figure 4.18: Working scheme of the MATLAB code to extract the actual deflection

To determine the point of maximum deflection (Xmax and Ymax), a small region of size 100 x 100 pixels containing the deflected surface is selected, as shown in Fig.4.19

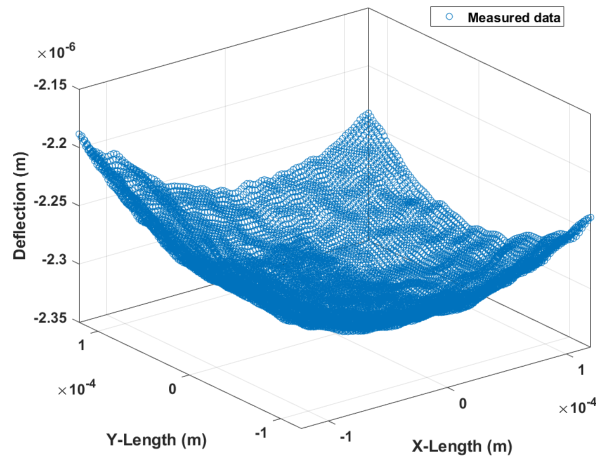

Figure 4.19: Selected region of interest for deflected surface

The selected surface is fitted with a polynomial equation, in our case, the quadratic polynomial is observed to be an appropriate fitting equation for the deflected surface. The quadratic fitting equation is shown in eq.4.4.

$$Z = p00 + p01x + p10y + p20x^2 + p02y^2 + p11xy \tag{4.4}$$

Where p00,p01,p10, p20, p02 and p11 are constants. By solving the derivatives dZ/dx=0 and dZ/dy=0, the point of maximum deflection (Xmax and Ymax as shown in eq.4.5 and 4.6 respectively) are obtained. By substituting the value of Xmax and Ymax in eq.4.4, the value of maximum deflection (Zmax) is calculated.

$$Xmax = \frac{2p02p10 - p01p11}{p11^2 - 4p02p20} \tag{4.5}$$

$$Ymax = \frac{-p10p11 + 2p01p20}{p11^2 - 4p02p20} \tag{4.6}$$

Fig.4.20 shows the comparison of actual and approximated deflected surfaces along with the indication of the point of maximum deflection.

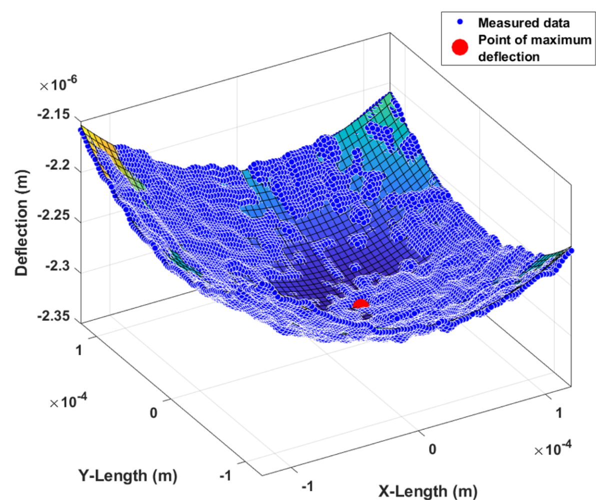

Figure 4.20: Comparison of measured and fitted deflected surface

To determine the minimum deflection value (Zmin), 4 small regions containing flat surfaces are selected around the corners of the unwrapped phase image, as shown in Fig.4.21.

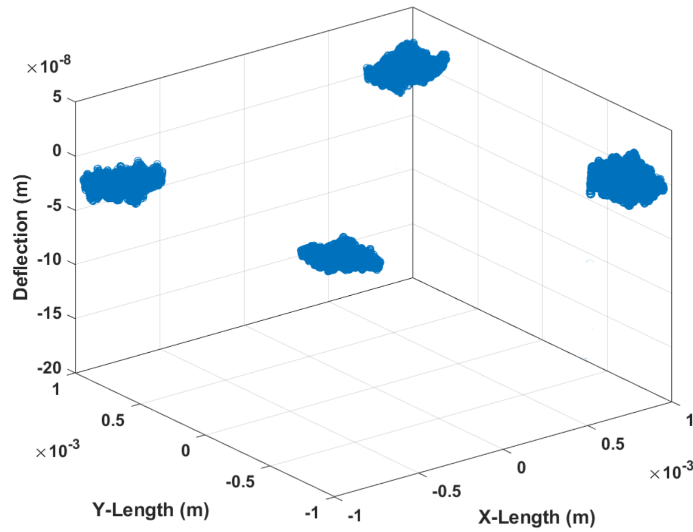

Figure 4.21: Selected region of interest for flat surface

In order to account for the tilt present in the measurement, these four flat regions are fitted using a linear equation as shown below:

$$Z(flat) = q00 + q01x + q10y \tag{4.7}$$

Where q00, q01, and q10 are constants. Zmin is calculated by substituting Xmax and Ymax obtained from eq.4.5 and eq.4.6 in eq.4.7. Fig.4.22 shows the comparison of actual and approximated flat surfaces and the indication of the point where maximum deflection occurred.

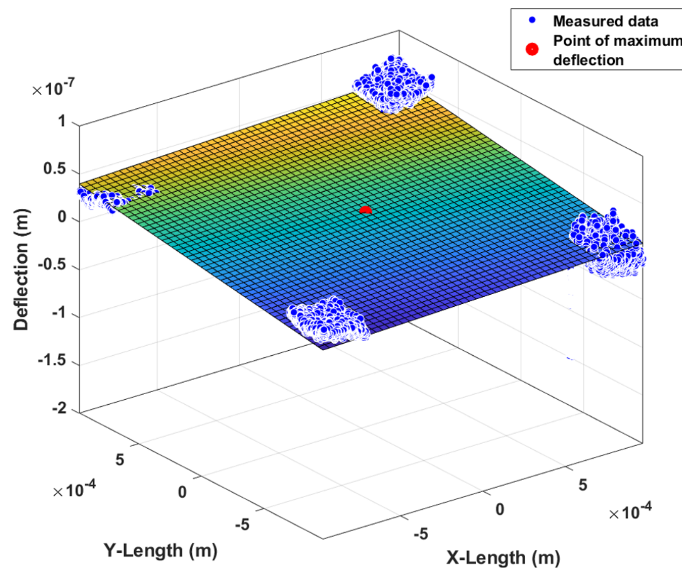

Figure 4.22: Comparison of measured and fitted flat surface

4.3. Errors in deflection measurement

While proceeding with steps for measuring deflection, there occurs errors in DHM that need to be corrected for reaching the ideal deflection measurement. Predominantly these errors arise while using the koala software. The key parameters which influence the deflection measurements are the contrast of the hologram image, title corrections segments for phase mask adjustment, and considered region of interest for deflection measurement. In this section, how variations in those koala parameters affect the captured deflection profiles is shown with an example of test specimen measurement.

4.3.1. Contrast of hologram image

:

For effective analysis of the sample, it is important to acquire a high-quality hologram. The interference fringes of the hologram consist of a series of alternating bright and dark lines (Fig.4.23). The contrast of the interference fringes of the hologram or more simply hologram fringe contrast is defined as the ratio of the difference over the sum of the maxima and minima along a profile, that is:

$$Contrast = \frac{Max - Min}{Max + Min} \tag{4.8}$$

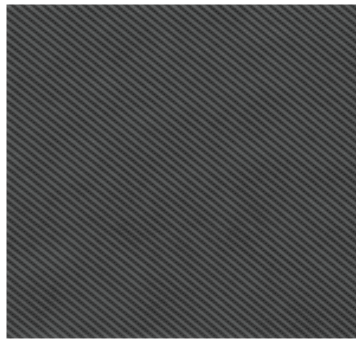

Figure 4.23: Fringe pattern in hologram

The ideal is a contrast of 1. In other words, the minima should be as dark as possible and the maxima as bright as possible. A reliable parameter to quantify the contrast is the standard deviation of the histogram of the hologram. This parameter is available in the form of *hologram contrast* at the bottom of the hologram histogram window. The hologram histogram window can be selected from the top menu of the hologram window, as indicated in (Fig.4.7).

When the histogram contrast of the hologram is less or at minimum (Fig.4.24), the corresponding intensity image appears blurry (Fig.4.25) and this reflects in causing a random profile for deflection, as shown in Fig.4.26.

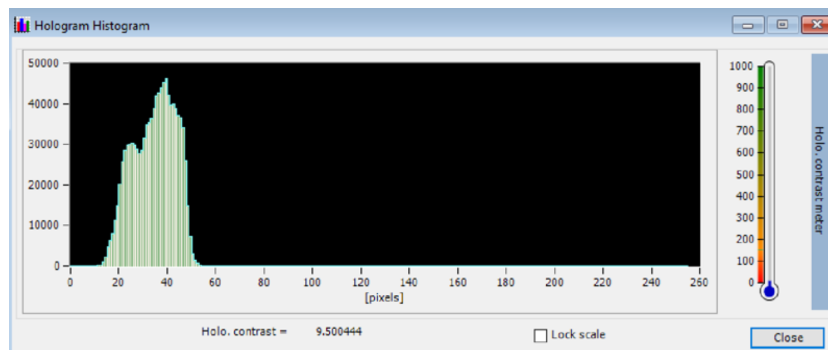

Figure 4.24: Low histogram contrast

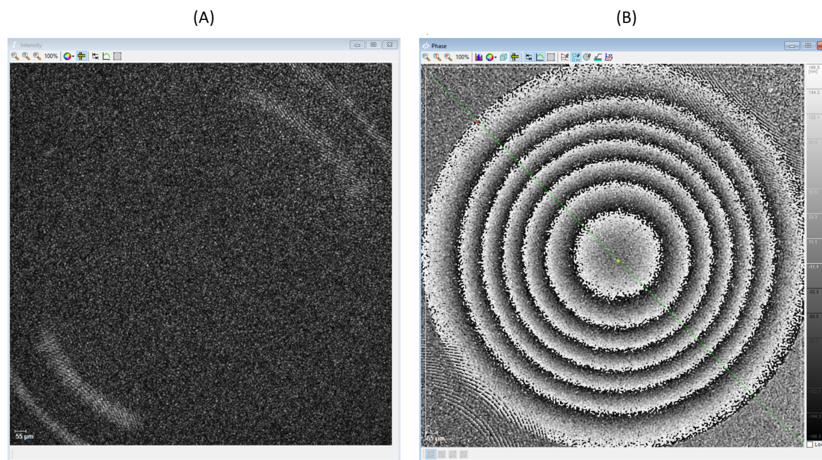

Figure 4.25: (A) Intensity image (B) Phase image, when the hologram histogram contrast is at minimum

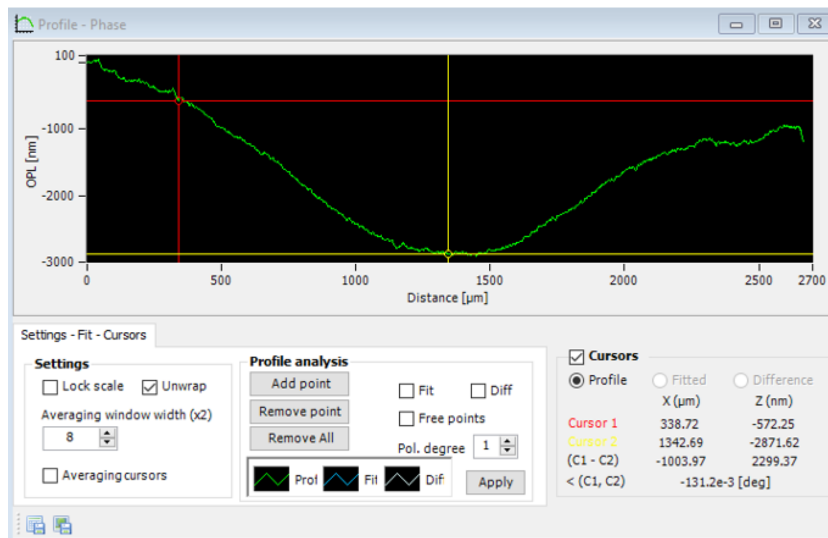

Figure 4.26: Deflection profile due to low-intensity contrast

To obtain the right deflection profile, the hologram histogram was increased by manually moving the microscope objective (or the optical head) closer to the test specimen. When the hologram contrast is increased to 100 (Fig.4.27), the intensity and phase image appears to be sharper and clear (Fig.4.28), and the obtained deflection profile is also appropriate (Fig.4.29).

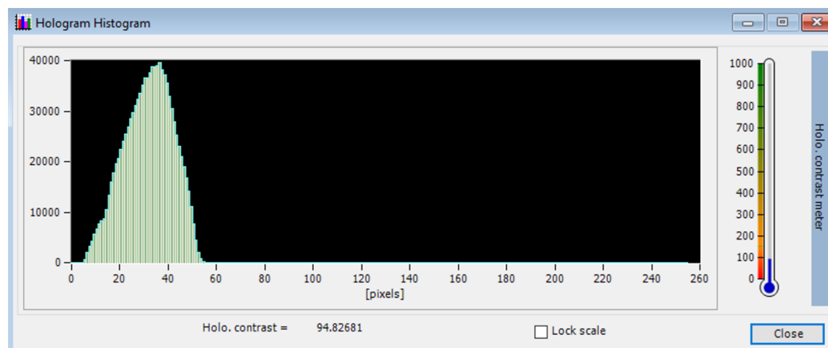

Figure 4.27: Hologram histogram contrast at 100

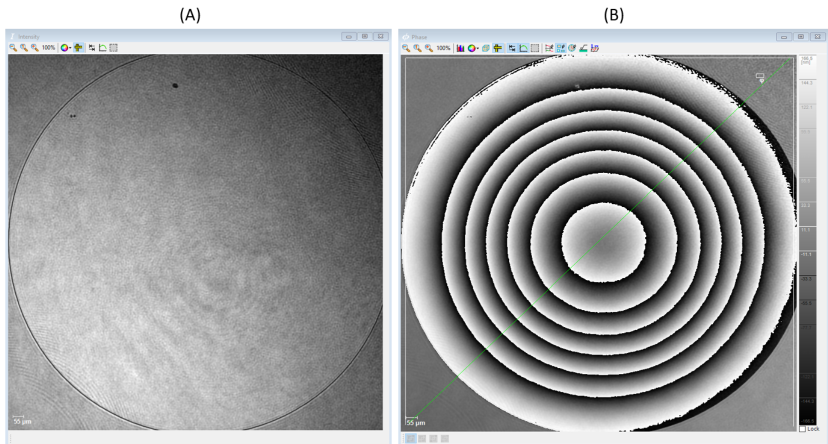

Figure 4.28: (A) Intensity image (B) Phase image, when the hologram histogram contrast is 100

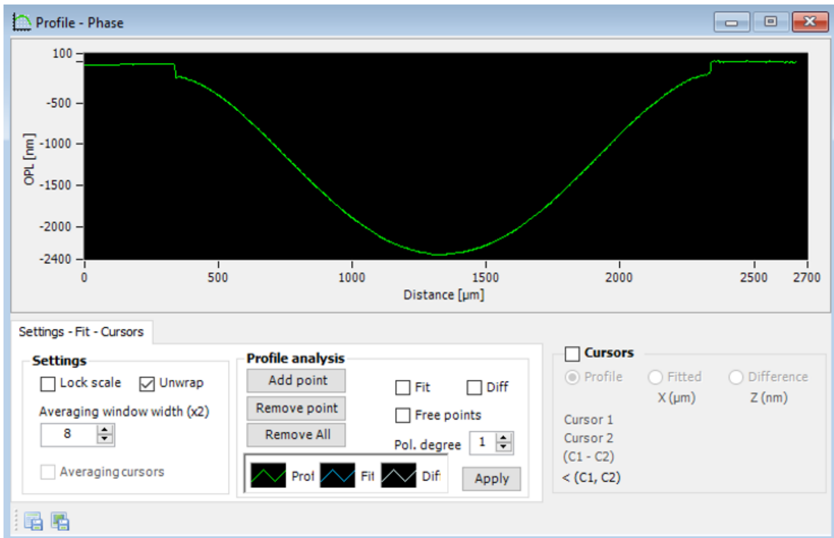

Figure 4.29: Deflection profile, when the hologram histogram contrast is 100

When the histogram contrast is increased further to 450, there was no significant change observed in the intensity image and the phase image (Fig.4.31). The deflection profile (Fig.4.32) appeared to be similar to the one shown in the previous Fig.4.29.

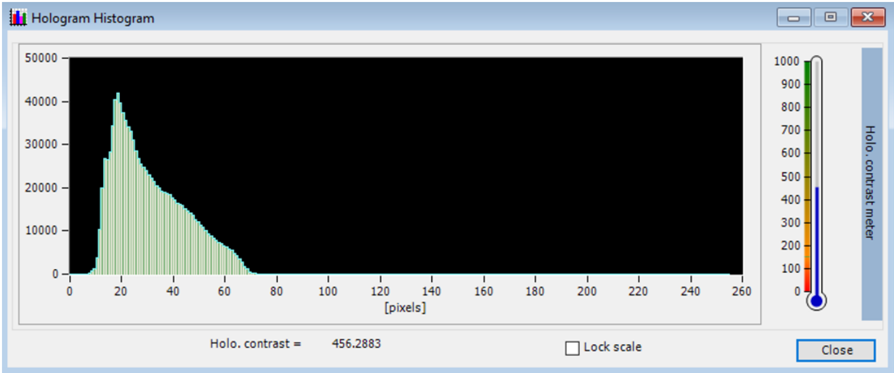

Figure 4.30: Hologram histogram contrast at 450

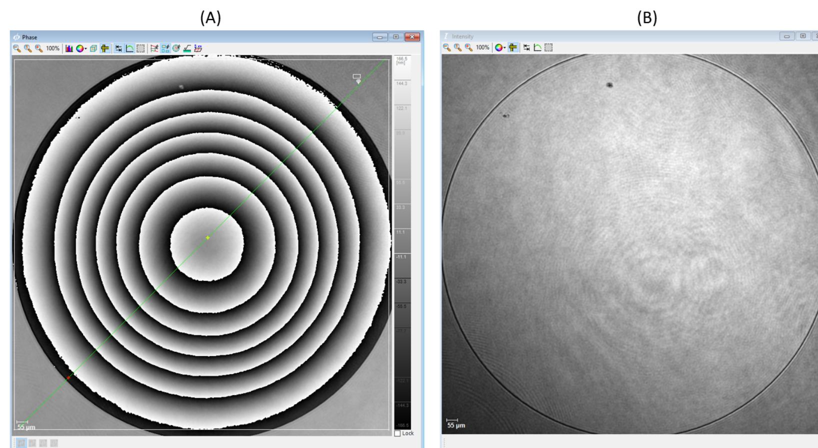

Figure 4.31: (A) Intensity image (B) Phase image, when the hologram histogram contrast is 450

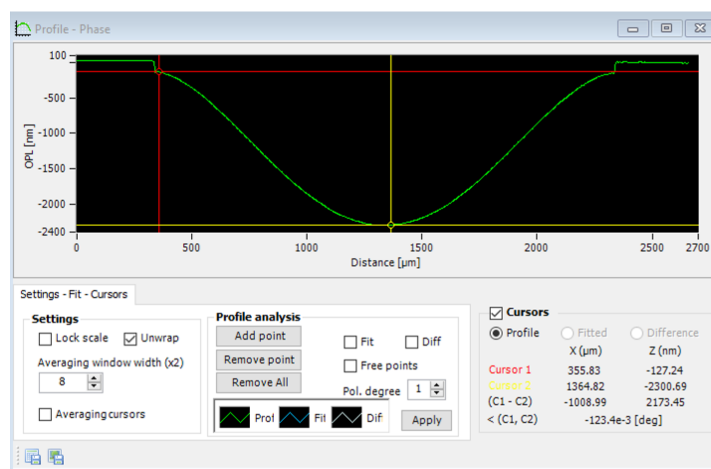

Figure 4.32: Deflection profile, when the hologram histogram contrast is 450

Hence the variations in hologram histogram contrast showed that at lower histogram contrast, the obtained deflection profile is not smooth and as a result, it becomes difficult to obtain a proper deflection profile. Therefore, to reach the final deflection measurement, it is essential to set a minimum level of hologram contrast every time. In our case, it was found that at least hologram contrast of 100 is required to be set to obtain a smooth deflection profile.

4.3.2. Tilt correction segments for phase mask adjustment

:

While performing tilt alignment of the sample using the phase mask adjustment tool available in the phase window, one needs to always draw 1D tilt correction segments on the sample surface to align the XY referential plane relative to the sample plane.

- When the drawn tilt correction line segment is small, the phase jump appears to be unresolved and the resulting deflection is improper as shown in Fig.4.33.

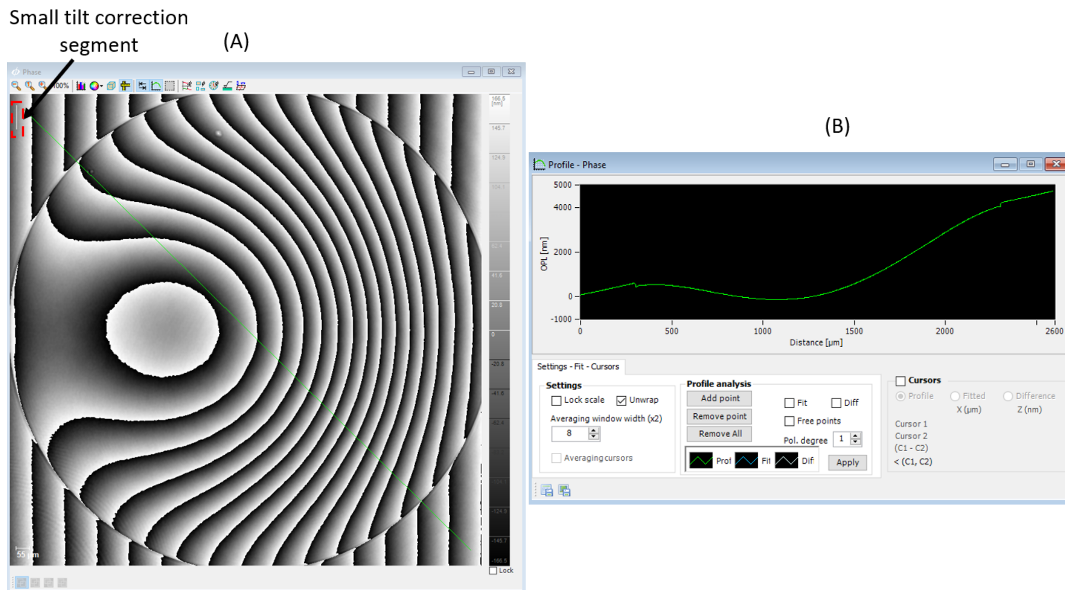

Figure 4.33: (A) Phase image when the drawn tilt correction segment is small (B) Deflection profile for the corresponding phase image

- When only 1 tilt correction line segment is drawn, the phase jump again appears to be unresolved (Fig.4.34).

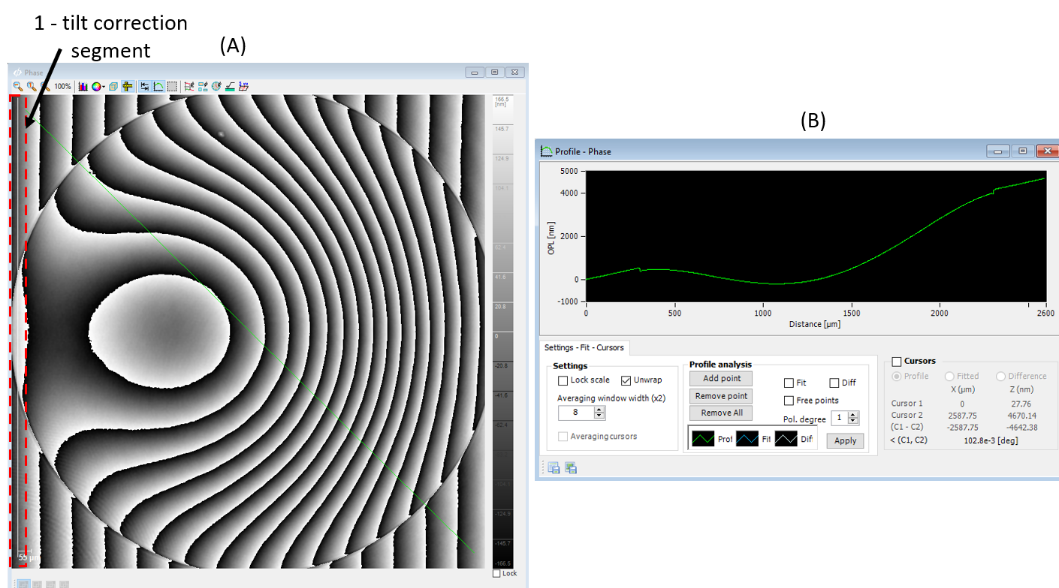

Figure 4.34: (A) Phase image when only one tilt correction segment is drawn (B) Deflection profile for the corresponding phase image

- When 2 orthogonal line segments are drawn, phase discontinuities could be clearly seen such that difference between a flat surface and a deflected surface can be observed (Fig.4.35).

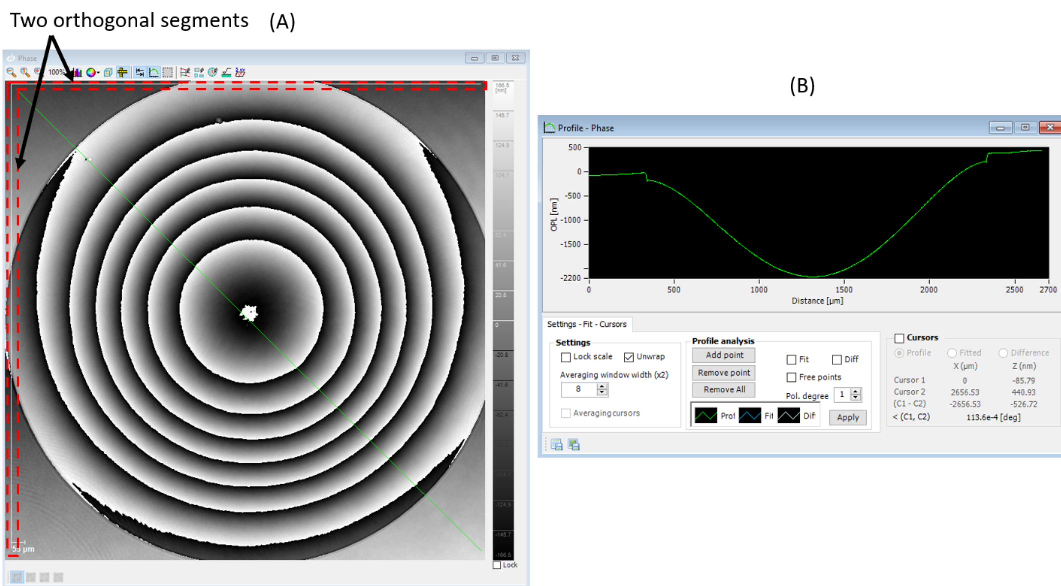

Figure 4.35: (A) Phase image when 2 orthogonal segments are drawn around the flat surface (B) Deflection profile for the corresponding phase image

- When 4 orthogonal line segments are drawn around the surface, phase discontinuities could be even more clearly differentiated (Fig.4.36).

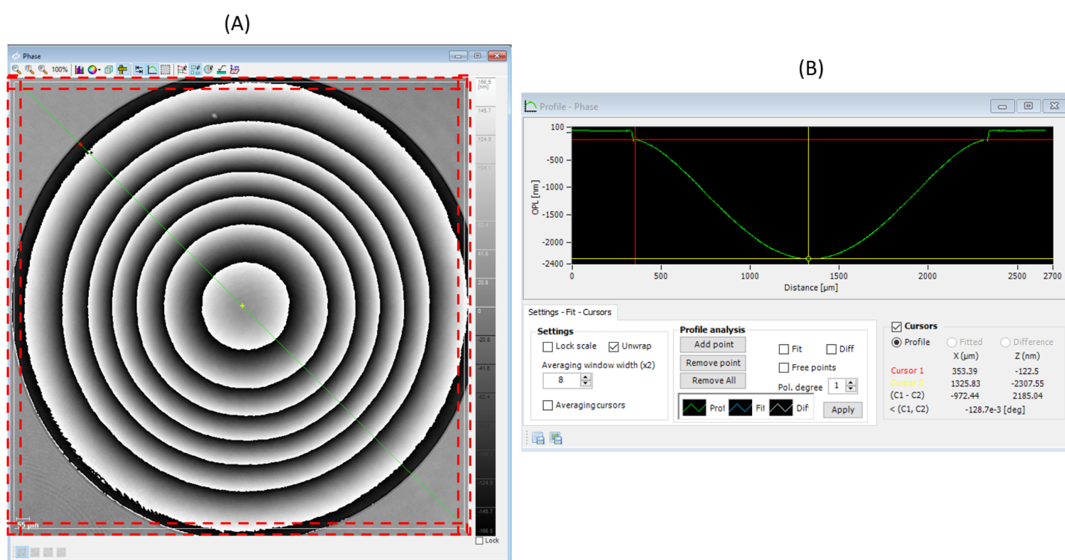

Figure 4.36: (A) Phase image when 4 orthogonal segments are drawn around the (B) Deflection profile for the corresponding phase image

Based on the trial with different tilt correction segments, it was observed that drawing a small segment or one-line segment led to a very minimalistic correction in tilt alignment which can eventually lead to inaccurate deflection measurement. Therefore, it is needed to trace at least two long orthogonal segments around the sample to obtain a clear deflected surface.

4.3.3. Region of interest for deflection measurement

While unwrapping the phase image for actual deflection measurement, it is often required to define smaller segments or regions of interest (ROI) around the deflected surface for accurate measurement. To investigate this issue, the deflection of a 900 µm diameter membrane is measured with a large ROI comprising 800x800 pixels. The phase image is shown in Fig.4.37.

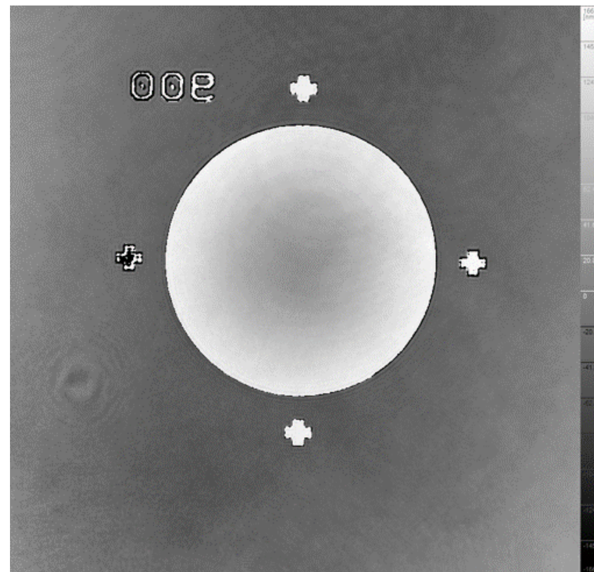

Figure 4.37: Phase image of 900 µm diameter of membrane with ROI of 800x800 pixels

Fig.4.38 shows the 3D representation measurement of the membrane which shows the unwrapping issue. At the edges, flat surfaces are not properly imaged. As a result, the flatness approximation also comes out to be incorrect (Fig.4.39).

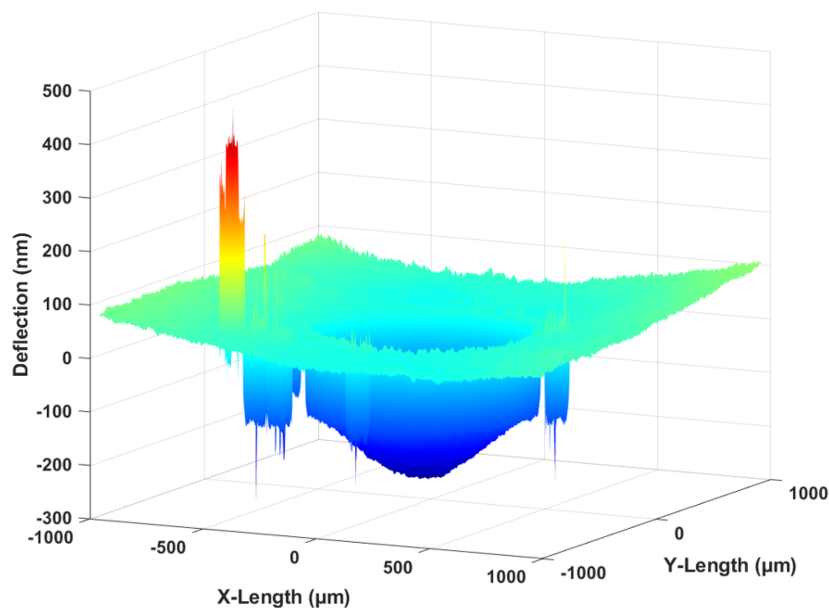

Figure 4.38: 3D profile of membrane with unwrapping issue at the edges

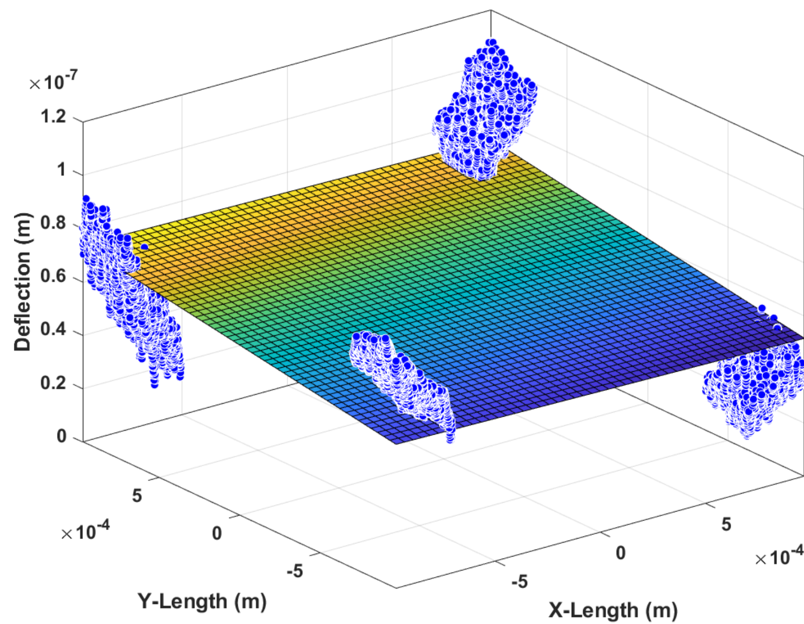

Figure 4.39: Approximation of flat surface with unwrapping issue

To overcome this issue, an ROI can be defined which is available at the top of the phase window. Using ROI allows unwrapping to be performed on the fixed window size and as a result flat surfaces could be properly imaged and also approximated with fit equations.

For the 900 µm diameter, an ROI comprising 400x400 pixels is applied, as shown in Fig.4.40. From the 3D profile (Fig.4.41) and flatness approximation image (Fig.4.42), it can be seen that along the edges surfaces are flat. Therefore, to have a reliable deflection measurement usage of ROI is essential.

Figure 4.40: Phase image of 900 µm diameter of membrane with ROI of 400x400 pixels

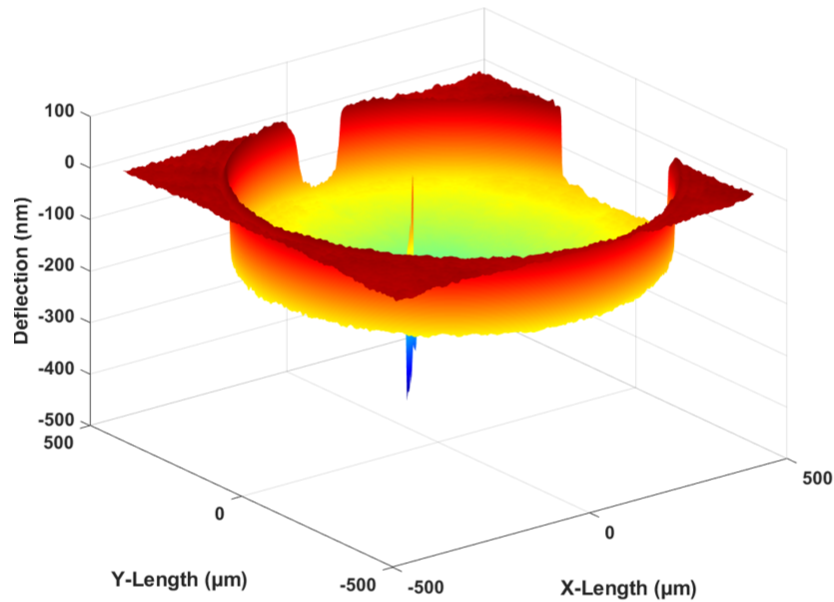

Figure 4.41: 3D profile of membrane with flat surfaces along the edges

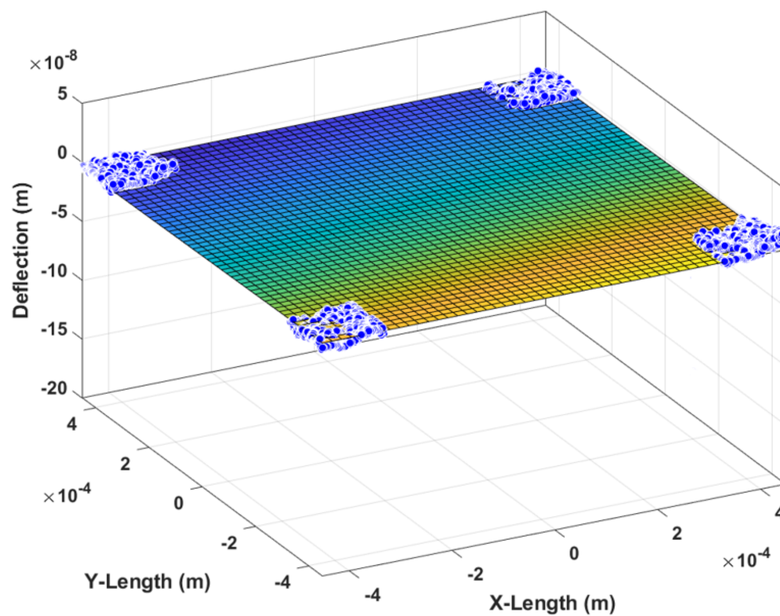

Figure 4.42: Approximation of flat surface with smaller ROI

4) **Error in edge detection**:

There is an additional error-case scenario that sometimes occurs while measuring with DHM is an edge detection error. If a part of the sample has a slope too steep to be resolved, then in such case the performed phase unwrapped leads to an unreliable measurement. Fig.4.43 shows the 3D profile of a membrane where the flat surfaces at 3 edges are flipped upside down.

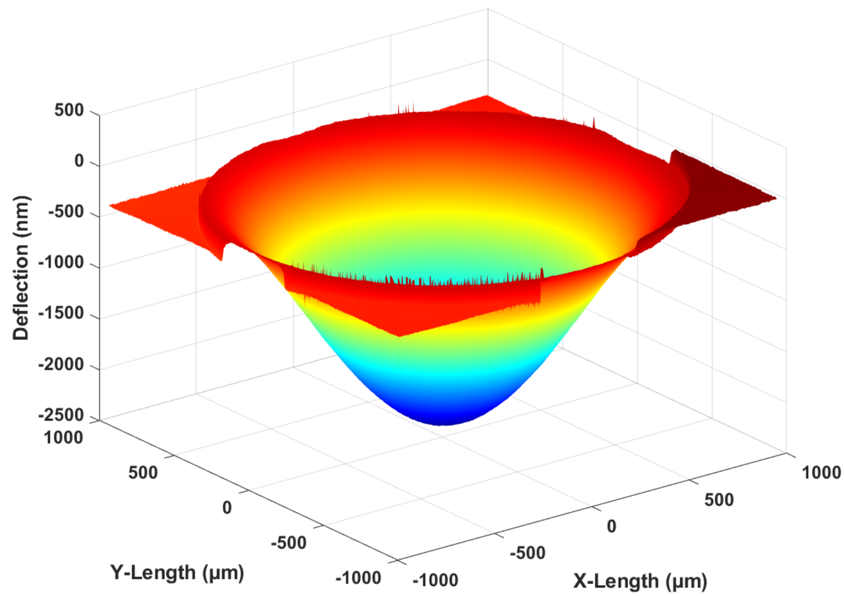

Figure 4.43: 3D profile of membrane having flipped surfaces along the edges

In such case, fitting the surfaces becomes incorrect as shown in Fig.4.44.

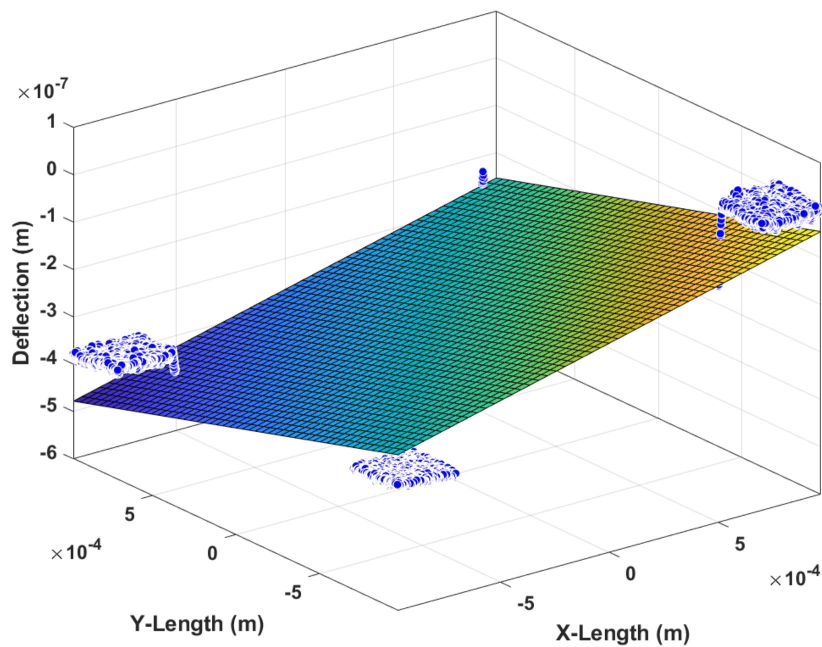

Figure 4.44: Approximation of flat surface with edge detection issue

For the edge detection issue, it was unable to find a proper solution. Rather, it was always preferred to restart the microscope and perform the measurements from step one to reach the final profile image as shown in the previous subsection Fig.4.17.

4.4. Experimental Setup

To test the hermiticity of the silicon-sealed cavities using DHM, a vacuum-chamber-based test setup is used. Fig.4.45 shows a schematic overview of the test setup used for conducting the hermiticity test. In this setup, the wafer-bonded cavity is mounted in a vacuum chamber with optical access, and a dual valve pressure controller is connected via an intermediate valve. In the dual valve pressure controller, one line is connected to the desired gas supply connection, and another line is connected to the vacuum pump.

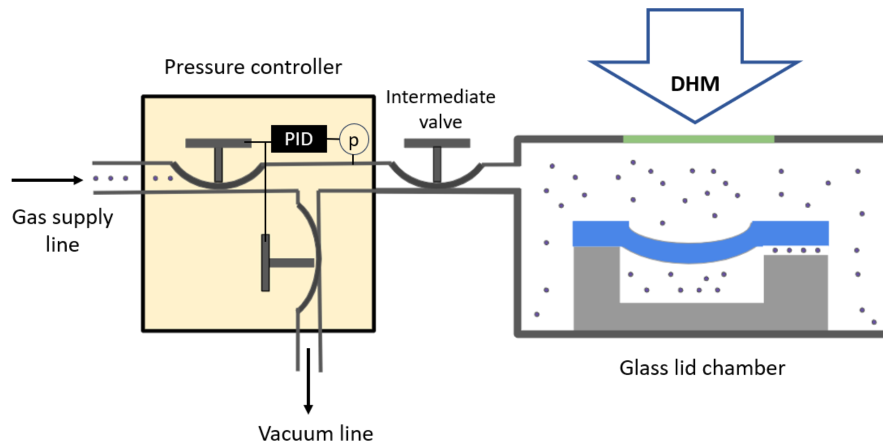

Figure 4.45: Illustration of hermiticity test setup

Fig.4.46 shows the experimental setup developed with different elements labeled. Refer to Table.4.2 for the list of components used.

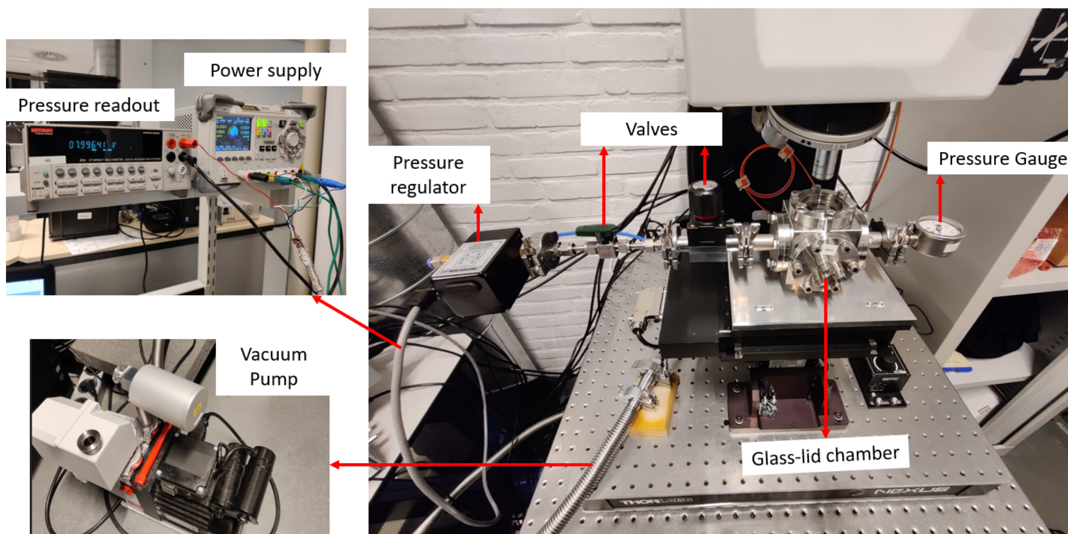

Figure 4.46: Experimental setup with labels indicating the major components

Table 4.2: Components used in Fig.4.46

Pressure controller	Proportion-Air QPV electronic pressure regulator
Power supply	RIGOL DP832A
Pressure readout	KEITHLEY 2701
Intermediate valves	EDWARDS speedivalve and Swagelok quarter-turn plug valve
Vacuum pump	Pfeiffer

Since a glass window is used, there are two main settings that need to be used in Koala: refractive index and optical path length specific for the sample.

- Refractive index: For a homogeneous sample, the relation between the phase measurement and the sample height is given by the refractive index of the surrounding medium (eq.4.2). For air, it is 1.

- Sample optical path length (OPL): To make a hologram, the object beam, and reference beams (Fig.4.1) need to interfere i.e., need to be coherent. In order to obtain two coherent beams, DHM separates the beam emitted by the laser source into two beams. When the two beams are recombined, they will be coherent and will form a hologram as long as the difference between the OPL of the two beams is less than the coherence length of the DHMs laser source. Measuring samples immersed in a liquid or through a window modifies the object beam OPL, as a result, it affects the hologram formation. Instead of modifying the object beam OPL, DHM provides an option for modifying the reference beam OPL to an arbitrary length using Koala to match perfectly and automatically the OPL of the object beam. The command SETTING-Sample allows access to sample settings to define the OPL, as shown in Fig.4.47. In our case, the optimal intensity and phase images (Fig.4.9 and Fig.4.15) are observed to be formed for OPL varying from -900 µm to -3000 µm.

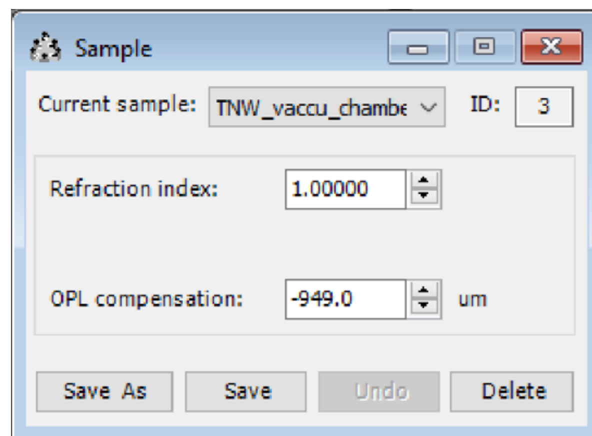

Figure 4.47: Sample setting window

4.5. Experimental Procedure

There are three experiments conducted using this test setup. The first experiment is for characterizing the membranes for pressure-deflection sensitivity, the second is for leak testing of bonded cavities with defined leak paths and the last is for leak testing the sealed-off bonded cavities.

Experiment-1 (Characterization of membranes for pressure-deflection sensitivity): The pressure-deflection characterization test was done to ensure that the membranes are showing deflections such that they can be compared with those predicted by theoretical formulas, as explained in the section.3.2.1 and also to test the presence of plastic deformation in membranes. The working procedure is as follows: The characterization test was conducted using the vacuum line connection. Inside the chamber, external pressure was varied from 1000 mbar to 100 mbar using the pressure controller, and the corresponding deflections of the membrane were captured using DHM. During this experiment, the intermediate valve was made open to provide access to the vacuum pump, and the gas supply line in the controller was connected to air. If the pressure inside the chamber increases or decreases beyond the set pressure level, then the controller automatically opens either the vacuum line valve or gas supply valve to regulate the pressure. Before working on this experiment, the reliability of the pressure controller was first inspected, this is explained in Appendix.D.

Experiment-2 (Leak testing of bonded cavities with defined leak paths): To get an initial understanding of how leakage works in wafer-bonded cavities, we fabricated some of the wafer-bonded cavities with

nanometer-gap channels. In this project, leak channels are defined between cavities. In order to facilitate a leak through these channels, a membrane from one of the cavities is broken and exposed to air under atmospheric pressure. At the initial time, when the cavities are not exposed to atmospheric pressure, the membrane deflected downwards. When one of the membranes is broken, the deflection of membranes from other cavities reduces due to the leak. This changing deflection is captured by DHM (Fig.4.48) over time to obtain the deflection rate (dZ/dt) and subsequently used to calculate the leak rate (dN_{in}/dt) using the expression derived for circular membrane (eq.5.3).

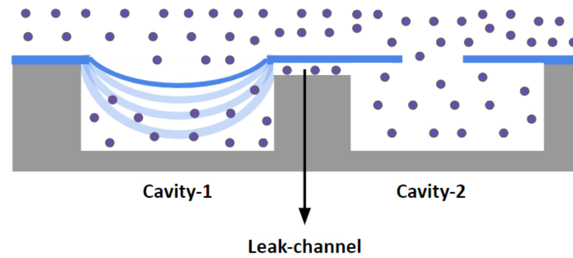

Figure 4.48: Illustration of the wafer bonded cavities with defined leak channel

Experiment-3 (Leak testing of sealed-off cavities): In this experiment, boned cavities with no leak channels are subjected to leak testing. As a first step, these sealed-off samples are exposed to air and tested for leakage. When no change in deflection is observed, they are exposed to a desired gas species and measured for change in deflection of membranes. In our case, Helium is used as the desired gas species, due to its smallest kinetic diameter (d_{He} = 260 pm).

To conduct the helium leak testing, the samples are kept in a vacuum chamber and filled with helium at 1000 mbar pressure. Before filling, the chamber was initially kept under the vacuum condition, and then by increasing the set pressure in the controller, it opens the gas supply valve to send the helium inside the chamber. To exclude any presence of air molecules, the chamber was flushed with helium multiple times. Once the helium is supplied, the chamber is locked with the intermediate valve such that to prevent leakage of gas outside or inside the chamber. At the initial time, when the chamber is filled with helium, the membrane deflects downwards when there is no pressure inside the cavity. This deflection reduces when the cavity pressure increases due to a leak. The changing deflection is again captured by DHM over time to obtain the deflection rate (dZ/dt) and subsequently used to calculate the leak rate (dN_{in}/dt).

4.6. Fabrication of test samples

Test samples for the planned experiments are fabricated at Philips. For samples having sealed-off cavities, the flow sequence followed for fabrication is illustrated in Fig.4.49. The process starts with a 200 mm diameter <100> double-sided polished (DSP) prime silicon wafer and a 200 mm diameter <100> silicon-on-insulator (SOI) wafer. The SOI wafer has a 40±0.5 µm silicon device layer and a 500±5 nm thick silicon dioxide layer on a 421±0.5 µm thick silicon handle layer. Then the prime silicon wafer is oxidized to form a 100 nm thick oxide layer, followed by that a thin layer of photoresist is deposited and patterned (Steps B and C). In the next step, the front side of the patterned wafer is etched using HF solution to remove the oxide layer and deep reactive ion etching (DRIE) to create the gap height (Step D). Then the silicon substrate is bonded to the SOI wafer by the silicon fusion bonding method (Step E). After that, the handle layer of the SOI wafer was completely etched away by the KOH wet etching process (Step F). Finally, the samples were made ready for the experiments after the wet etching of the silicon dioxide layer in an HF solution (Steps G and H).

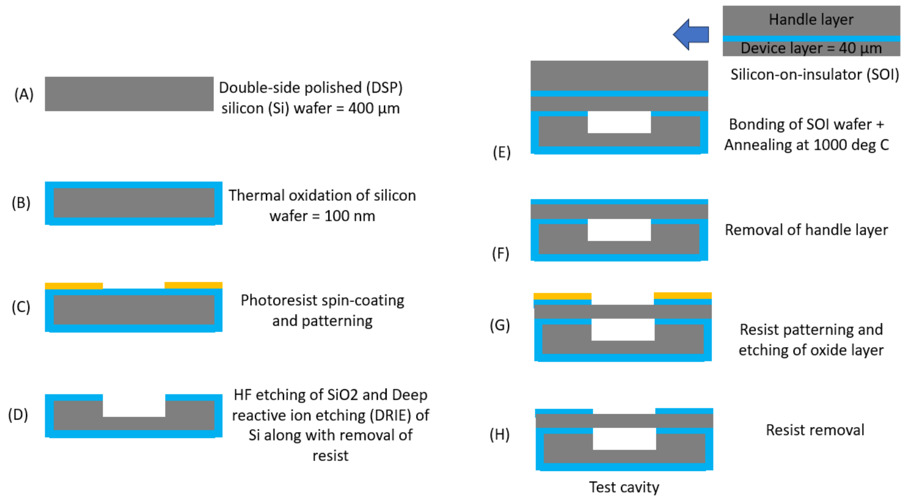

Figure 4.49: Process flow for fabricating silicon membranes with sealed cavity

The flow sequence followed for fabricating samples with leak channels is illustrated in Fig.4.50. Since rectangular channels are easily manufacturable using standard photolithography process, therefore this is the geometry adopted for our work. For these samples, similar steps were followed as used for preparing seal-off cavities (Fig.4.49). The only change occurs in steps D, E, and F. Once photoresist patterning is done in Step C, the oxide layer is etched in HF solution to create a depth for the leak channel (Step D). Followed by that, again photoresist is coated and patterned (Step E) for creating a cavity in Step F.

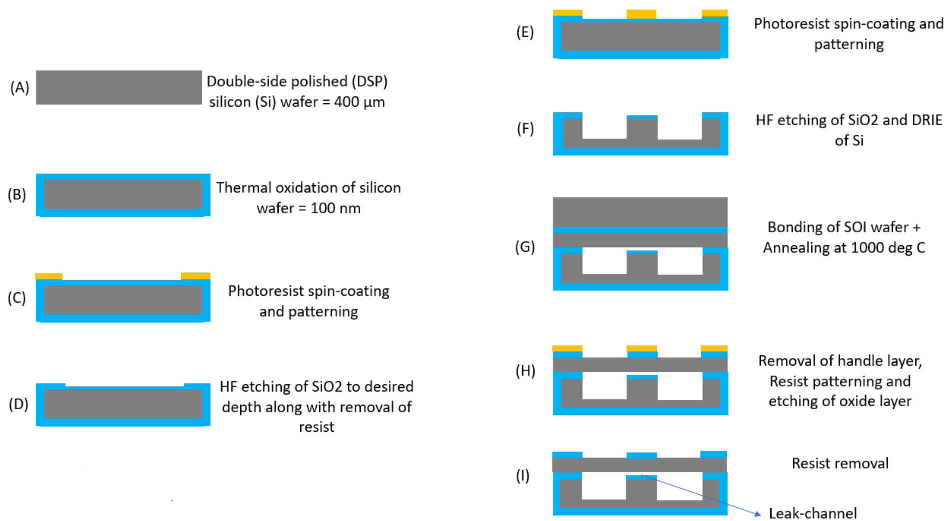

Figure 4.50: Process flow for fabricating silicon membranes with cavities having leak channels

For our experiments, samples with sealed-off cavities and samples with leak channels were fabricated in separate bonded wafers. The bonded wafer is diced into many chips with each chip of size 10mm x 10mm. In each chip, we made sure that there were many test cavities available for the same diameter so that in a single die multiple membranes could be tested. At the same time, the test cavities and leak channels are positioned in such a way that when one of the cavities is opened up, the other nearby cavities get exposed to the atmospheric pressure via the leak channels. To study the effect of leak channel size, different lengths, widths, and depths were provided for leak channels. The length of the leak channels corresponds to the distance between the membranes, which is shown in the mask layout designs for fabricating the membrane, and cavities, Fig.4.51. The width of the channels is provided in a separate mask layout, Fig.4.52. In this project, the considered depth for leak channels is 50 nm.

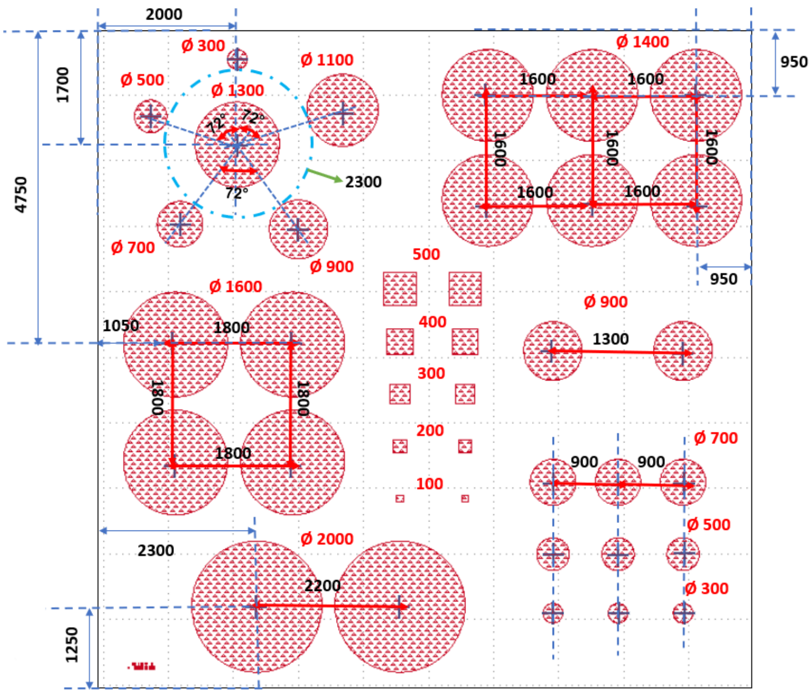

Figure 4.51: Mask layout design for membranes and cavities (Dimensions in μm)

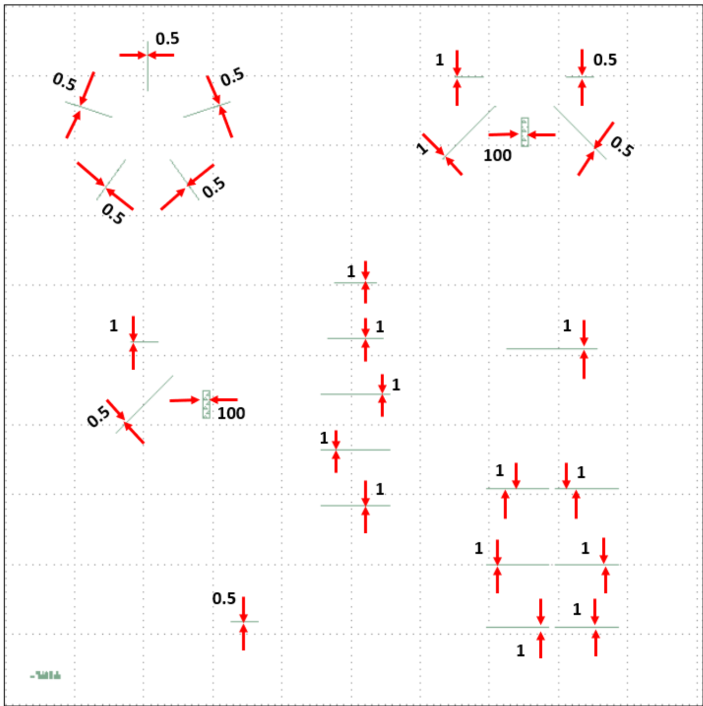

Figure 4.52: Mask layout design for leak channels (Width dimensions in μm)

4.7. Uncertainty in fabricated test samples

Prior to the leak test experiments, the prepared cavities were subjected to the uncertainty study, which is briefly explained below given subsections.

4.7.1. Non-contact profilometer imaging for depth measurements

Before bonding the substrate with the SOI wafer, fabricated cavity depths were first measured to check whether it achieved the desired values of 2.30 µm. The cavity depths were measured along a line on the 200 mm diameter wafer using a white light interferometer (CYBER Technologies CT-300) along with included software (AScan). The depth measurements were done in such a way that first the height level between the objective lens and the bottom of the cavity is measured, which is subtracted from the height level between the objective lens and flat surface (Fig.4.53).

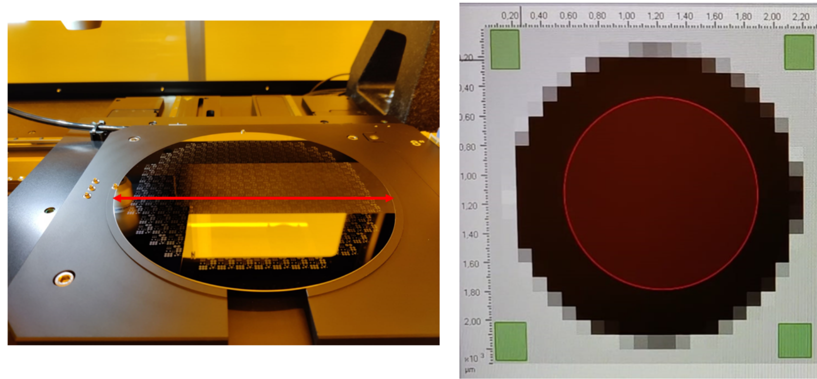

Figure 4.53: (A) Automated cavity depths measurements were performed along the line on the wafer (B) Markers drawn for measuring the bottom of the cavity and flat surface

In total, 17 chips (dies) were subjected to cavity depth measurements. Within a die, cavities with diameters of 2000, 1600, 900, and 300 µm were measured. From those measurements, we observed that the achieved cavity depths did not match with desired cavity depths. Instead of 2.3 µm, **the achieved depth was 3.24 ±0.06 µm**. Also, the variation in cavity depth appears to be asymmetrical along the line, as shown in Fig.4.54. This was attributed to the fact that the etching formula and etching rate were not tuned to this particular mask design, which eventually resulted in asymmetrical variations and a greater cavity depth.

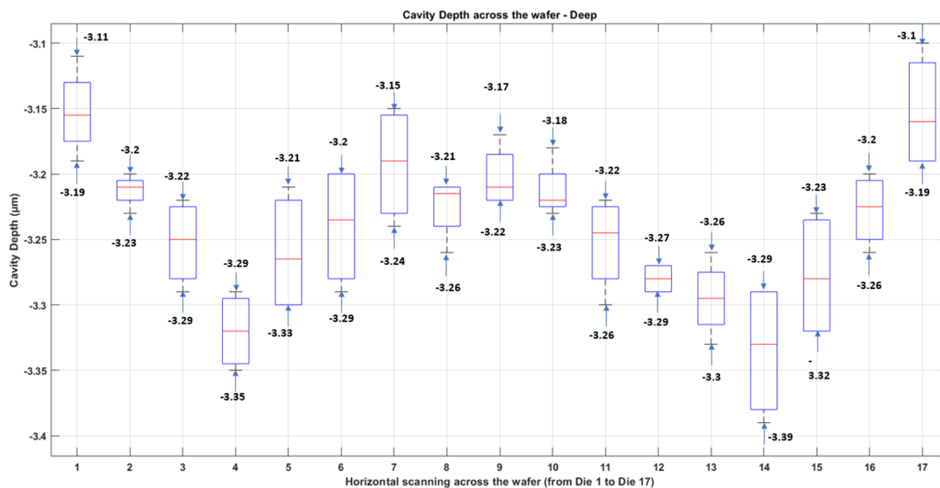

Figure 4.54: Variations in cavity depth among the measured 17 dies (wafer with deep cavity depth)

4.7.2. Scanning electron microscope imaging for thickness measurements

From the manufacturer's end it was provided that the device wafer (in this case the membrane) has a thickness of about 40±0.5 µm. To inspect and measure this uncertainty, a scanning electron microscope (SEM, JEOL-6010 LA) using a 90° sample holder was used after the test cavities were sputter-coated (SC7620, Quorum Technologies) with an 18nm layer of gold (Au). To measure thickness, the test cavities were cut along their cross-section using a nanosecond laser machine. Two test cavities were used and the thickness measurement was made during the imaging using the provided software InTouchScope (JEOL, Ltd.). From Fig.4.55 and Fig.4.56, we can clearly see that the uncertainty in measured thickness was apparently within the range as specified by the manufacturer. **Therefore the uncertainty in thickness is certainly considered as 0.5µm**.

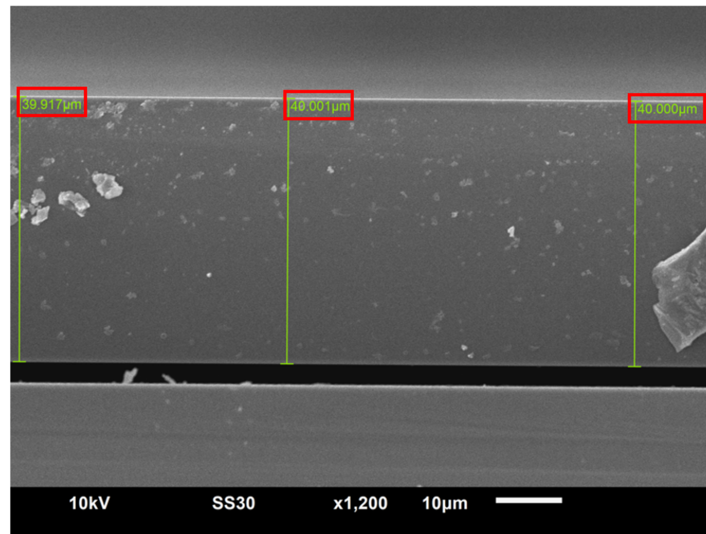

Figure 4.55: Thickness measurement of a membrane from test cavity-1

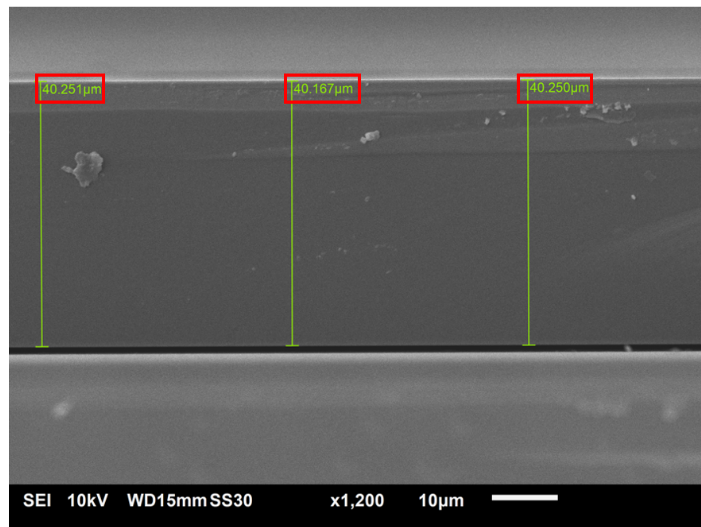

Figure 4.56: Thickness measurement of a membrane from test cavity-2

4.7.3. SEM imaging of leak channels

For samples with leak channels, it was reported from the manufacturer's end that leak channels achieved from the wet-etching process did not produce depths matching with desired channel depths, based on their atomic force microscopy (AFM) measurements. Instead of 50 nm depth, **the achieved depth of the leak channel was 34nm**. In addition to this, it was observed that the wet-etching did cause some notching at channel walls and on the bottom surface as well. From the obtained SEM images Fig.4.57 and Fig.4.58, we are able to confirm the fabricated leak channels do not have a uniform area of cross-section throughout the channel length.

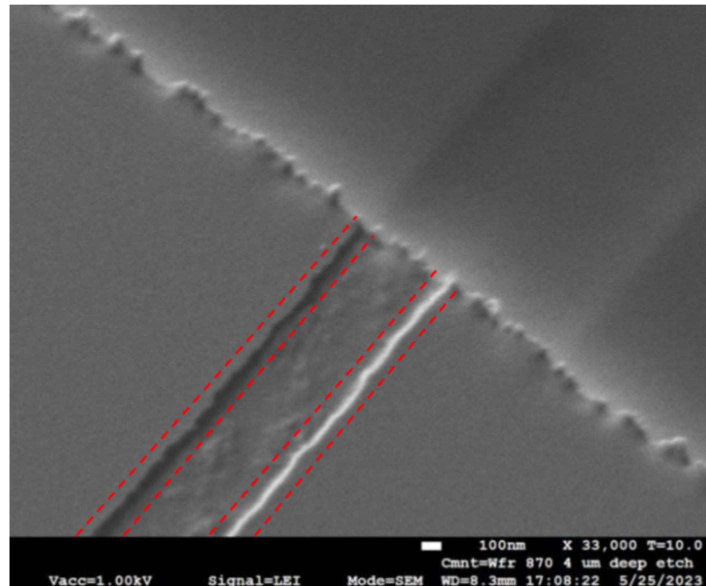

Figure 4.57: SEM images of leak channel having wedges along the walls

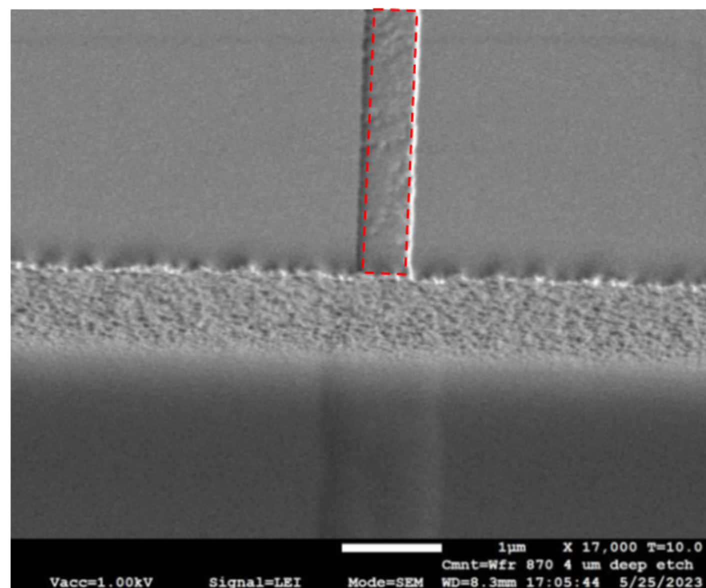

Figure 4.58: SEM images of leak channel having a rough bottom surface

4.7.4. Keyence digital microscope imaging for diameter measurements

To measure the diameter of membranes, a digital microscope (Keyence VHX-6000) was used. Using the 'mix' lighting option membrane diameter images were obtained. This was done to make a distinction between the targeted membrane diameters and the oxide surface (Fig.4.59 and Fig.4.60), which would enable easy measurement of diameter.

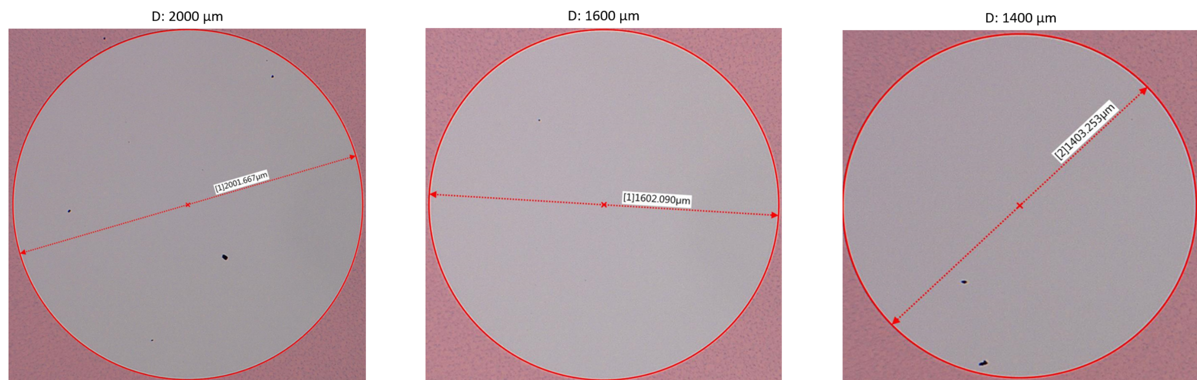

Figure 4.59: Diameter images made using the Keyeence digital microscope for diameters: 2000, 1600, and 1400 µm

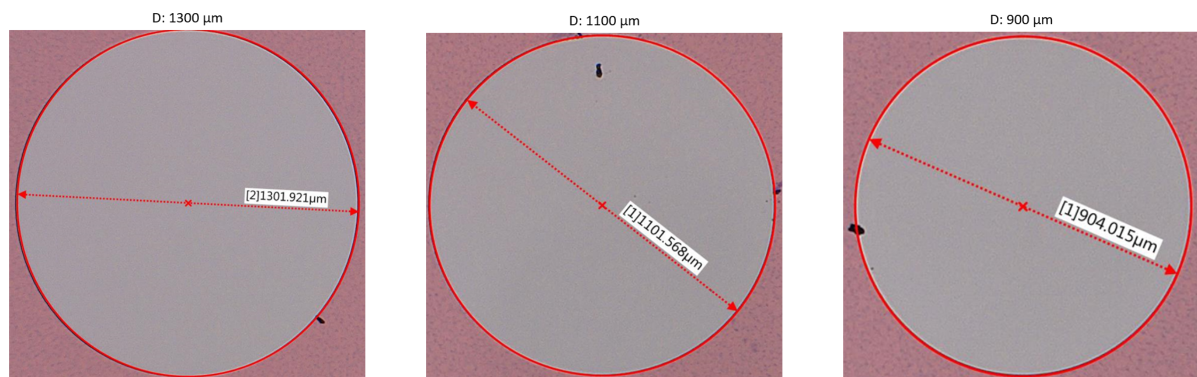

Figure 4.60: Diameter images made using the Keyeence digital microscope for diameters: 1300, 1100, and 900 µm

To analyze the uncertainty, 10 different samples are measured for each diameter. For all measurements, the maintained magnification was x100.0. Table.A.1 in Appendix.A summarises those measurements along with calculated standard deviations. Based on all the measurements, an average standard deviation is calculated, which could be used for all diameters. **Therefore, the considered value for uncertainty in diameter is 2.0 µm**.

4.7.5. Random uncertainty in deflection measurement

When a test cavity is subjected to leak testing, its corresponding membrane's deflection would be measured at different time intervals. Sometimes, it may even be required to measure the same membrane for several days. In such cases, DHM often needs to be switched OFF/ON and every time settings in Koala need to be defined to start the measurement. In addition, there might be changes in environmental conditions such as changes in temperature, and change in environmental pressure. These conditions cause random errors in deflection measurements.

To analyze the random uncertainty, the deflection of different membranes is measured for several days. Also, to check the reproducibility of pressure-deflection experiments, all the deflections are obtained by sweeping the external pressure from 1000 mbar to 100 mbar. All the deflection values and the corresponding standard deviation values are shown in Tables.B.1, B.2, B.3, B.4, B.5 in Appendix.B. Among the obtained standard deviations, the maximum value calculated is 7.25 nm. **Since the random error is unknown or unpredictable, therefore an over-estimation is made to the random error in deflection measurement, which is equal to 10 nm**.

4.8. Estimation of uncertainty in measuring leak rate

Having determined all the uncertainties, it is important to know how accurate our leak testing method is in measuring the leak rate for a given cavity. To understand this, an estimation is made on uncertainty in measuring leak rate.

The error estimation for leak rate is made for circular membrane, therefore we used the eq.5.3. Here it is represented in a simplified form:

$$\frac{dN_{in}}{dt} = (\frac{64D}{a^4})(\frac{V_{eff}}{RT})(\frac{Z_2 - Z_1}{\Delta t}) \tag{4.9}$$

By substituting the expression for D (isotropic rigidity) and V_{eff} (effective volume) in eq.4.9, the leak rate expressions are as follows:

$$\frac{dN_{in}}{dt} = \underbrace{(\frac{1024Et^3}{12(1-\gamma^2)d^4})(\frac{Ag + \frac{P_{ext}A^2c_1}{K} - 2Ac_1Z}{RT})}_{c_2}(\frac{Z_2 - Z_1}{\Delta t}) \tag{4.10}$$

For a given cavity, the main source of error in measuring a small leak rate is the error in the deflection (Z) measurement. When the deflection measurement error is comparable to Z_2-Z_1, the leak rate error becomes higher. Therefore, to estimate the error in leak rate based on the error in deflection, the partial derivative method is used. A general method of getting the formulas for propagating errors involves the total differential of a function. Suppose that z=f(w,x,y...), where the variables w,x,y,z, etc. are independent variables. The total differential is then:

$$dz = \sqrt{(\frac{\partial f}{\partial w}dw)^2 + (\frac{\partial f}{\partial x}dx)^2 + (\frac{\partial f}{\partial y}dy)^2} \tag{4.11}$$

Here dw=U_w as the uncertainty in w and likewise for other differentials dz, dx,dy, etc. To adopt this approach, we used the leak rate expression 4.10 and obtained the derivative expression for leak-rate $\frac{dN_{in}}{dt}$ with respect to deflection (Z). Here, the terms within c_2 are assumed constant for given a cavity and membrane. It is because, there are uncertainties involved in D,t, and g which gives a systematic error, but for a given cavity and membrane it is constant. Also, the contribution of error in Z within the term c_2 is assumed small. Therefore, over a time period dt, all the terms are considered constant.

In such a case, the error in $\frac{dN_{in}}{dt}$ is given by:

$$d(\frac{dN_{in}}{dt}) = \frac{c_2}{\Delta t}\sqrt{((dZ_2)^2 + (dZ_1)^2)} \tag{4.12}$$

By considering constant error in deflection for all times t, the above expression simplifies, which gives the final expressions for uncertainty in leak rate:

$$d(\frac{dN_{in}}{dt}) = \frac{c_2}{\Delta t}\sqrt{2}\ \ dZ \tag{4.13}$$

Here dZ is the standard deviation (error) in the measurement of deflection. In our case, as we estimated in subsection4.7.5, the value of dz is 10nm.

Having derived the expression for uncertainty in leakrate and assigned the value for error in deflection. Finally, an estimation is made for uncertainty in leakrate (in mol/sec) for all considered diameters, as shown in Table.4.3. Here the considered value of thickness is 40 µm, gap height is 3.24 µm and P_{ext} is 1000 mbar, and the value of Z in c_2 corresponds to P_{ext} for all diameter membranes.

Table 4.3: Estimation of uncertainty in leak rate (mol/sec) for membrane with a thickness of 40 µm and cavity with gap height of 3.24 µm

Diameter (µm)	Uncertainty in leak rate (mol/sec)
2000	1.93E-12
1600	3.85E-12
1400	5.35E-12
1300	6.34E-12
1100	9.11E-12
900	1.38E-11
700	2.30E-11
500	4.53E-11
300	1.26E-10

The above-calculated values are uncertainty involved in measuring leak rate for one second time gap between two successive deflection measurements. Based on these values, it can be seen that for a given thickness of the membrane and gap height of the cavity, uncertainty in measuring the leak rate is smallest for the largest diameter.

To implement the leak-testing method as part of the inline testing, it is important to understand the significance of the uncertainty values that have been determined above. In the experiments performed pertaining to the testing of leakage in sealed-off cavities, a cavity having a membrane with a diameter of 2000 µm yielded a leak rate of around 1×10^{-17} mol/sec (refer to section.5.4). In order to determine this leak rate, the deflection of the relevant membrane was measured over a span of several days. However, from a company point of view, a precise number is required for time to measure such an order of leak rate. In this scenario, the tabulated data provide useful information. For eg., in the case of a cavity having a 3.24 µm depth bonded with a membrane having a thickness of 40 µm, we estimated the uncertainty in measuring the leak rate for 2000 µm diameter as 1.93×10^{-12} mol/sec. Hence, in order to reach an error in leak rate equivalent to 1×10^{-17} mol/sec, the deflection measurement at least needs to be taken for 193000 seconds ($1.93 \times 10^{-12}/1 \times 10^{-17}$), which is equivalent to 2 days.

5

Results and Discussion

5.1. Pressure-Deflection Characterization

The pressure-deflection characterization test was performed on dies from the wafer having sealed-off cavities. In total, three dies were chosen. Within each die, all the 29 cavities (refer to fig.4.51) were tested which include 2-2000 µm drums, 4-1600 µm drums, 6-1400 µm drums, 1-1300 µm drums, 1-1100 µm drums, 3-900 µm drums, 4-700 µm drums, 4-500 µm drums and 4-300 drums. Hence, in total 6-2000 µm drums, 12-1600 µm drums, 18-1400 µm drums, 3-1300 µm drums, 3-1100 µm drums, 9-900 µm drums, 12-700 µm drums, 12-500 µm and 12-300 µm drums were subjected for sensitivity characterization. As explained in section 4.5, this experiment was conducted by reducing the external pressure inside the chamber and subsequent measurement of deflection using DHM. The deflection measurements were done for external pressures ranging from 1000 to 100 mbar.

The maximum deflection data obtained from this characterization test showed a linear behavior with respect to changing pressures. This linearity is as expected from the linear pressure-deflection relation (eq.3.16). A plot for a 2000µm drum is shown in Fig.5.1, where we can see the linear curve fitting perfectly captures the measured deflection data points. Here, the slope of the fitting equation represents the pressure-deflection sensitivity (in nm/mbar). Similarly, the same linear fitting method was used for all the diameter drums to obtain the sensitivity response. Along with the indication of linear behavior through slope in the fitting equation, there was also observed an offset in the form of an intercept, which is thought that membranes have an inherent plastic deformation, this is discussed more in the section. 5.2 .

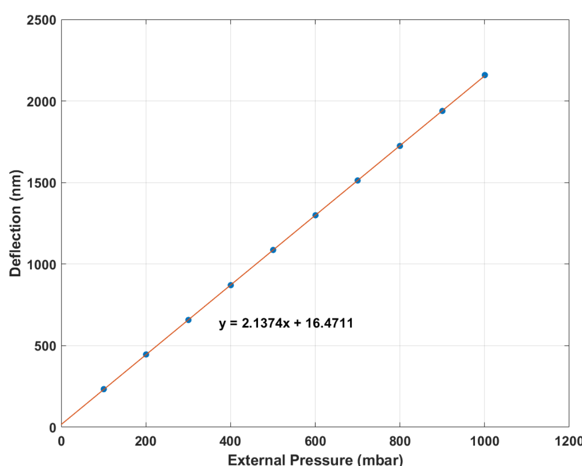

Figure 5.1: Measured and fit pressure-deflection curve for 2000 µm drum

The suitability of pressure-deflection characterization tests for diameters of 500 and 300 µm was found to be inadequate. This discrepancy arises due to the limited vertical measurement resolution of DHM in capturing small changes in deflection corresponding to variations in external pressure. Consequently, the deflection profile obtained from DHM appears to be not resolved well, as shown in Fig.5.2. As a result of this condition, the deflected surfaces were unable to be fit with the quadratic equation (as explained in step 8 of section 4.2) to determine the maximum deflection value and perform the subsequent linear fitting required to obtain the pressure-deflection sensitivity. This phenomenon is illustrated in Fig.5.3, which displays the pressure-deflection curve for a 500 µm membrane that cannot be accurately modeled using a linear equation. However, it was not noticed that this problem was present in membranes with diameters ranging from 2000 µm to 700 µm. The deflection profiles obtained for the 700 µm membrane, as shown in Fig.5.4, demonstrate the clear capture of membrane deflection by DHM. Consequently, the pressure-deflection curve could be accurately fitted with a linear equation to characterize sensitivity, as shown in Fig.5.5. Hence, to conduct the pressure-deflection characterization, only membranes with the following diameters were taken into account: 2000 µm, 1600 µm, 1400 µm, 1300 µm, 1100 µm, 900 µm, and 700 µm.

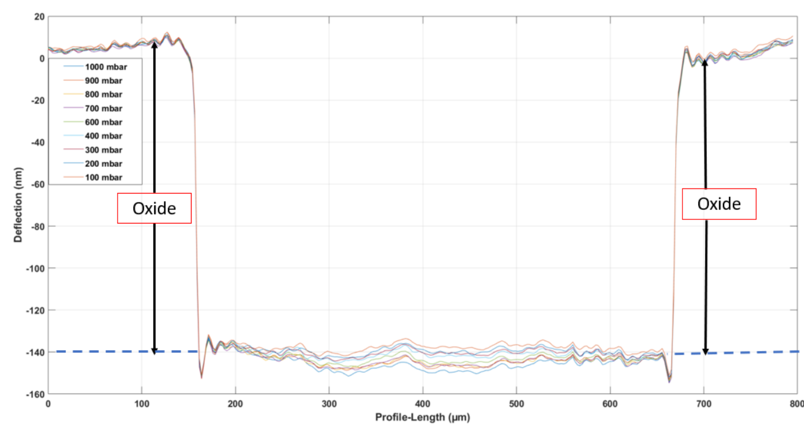

Figure 5.2: Deflection profile of 500µm membrane for external pressure varying from 1000 mbar to 100 mbar

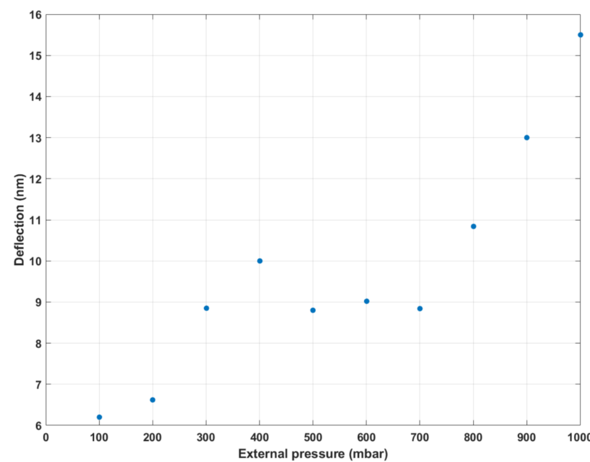

Figure 5.3: Improperly obtained pressure-deflection curve for 500µm membrane

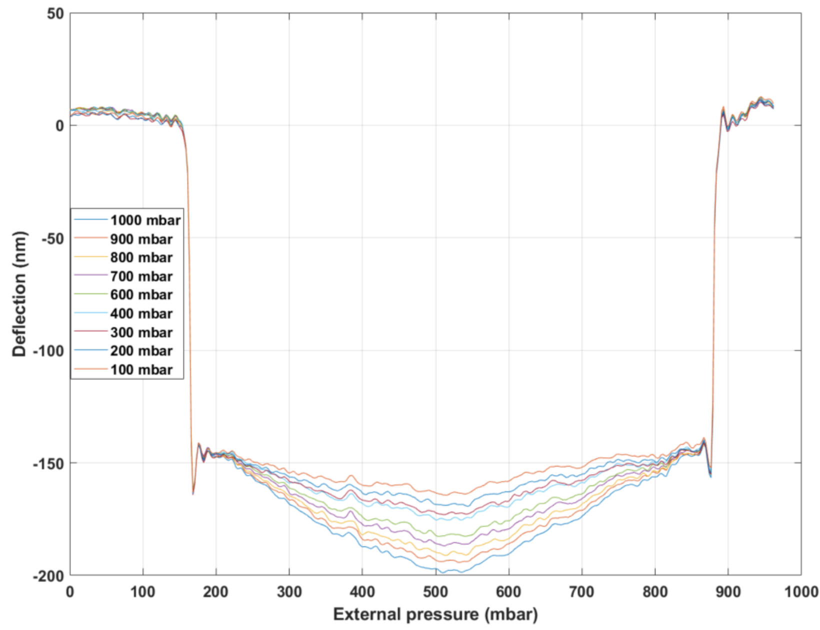

Figure 5.4: Deflection profile of 700µm membrane for external pressure varying from 1000 mbar to 100 mbar

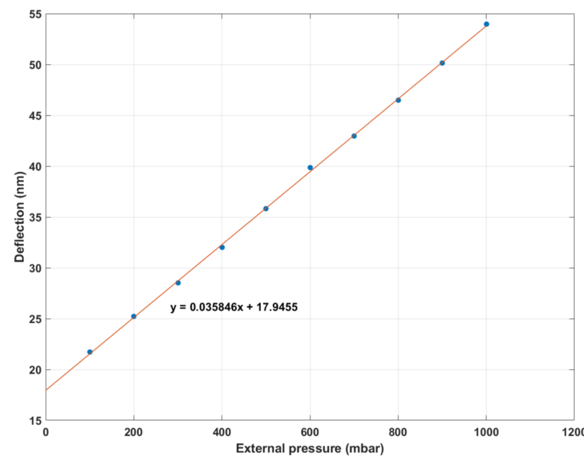

Figure 5.5: Measured and fit pressure-deflection curve for 700 µm drum

The pressure-deflection sensitivity is the key parameter used for the leak rate calculation (eq.5.3). Therefore, we compared the experimental sensitivity values for all diameters with the one calculated using the pressure-deflection eq.5.2 and the results (Fig.5.6) suggest that the considered analytical equation for circular membrane in the leak-rate equation and values considered for Young's modulus and Poisson's ratio are correct. Here the experimental values are the mean of all sensitivity values obtained for a specific diameter.

$$Z = \frac{\Delta P a^4}{64D}; \qquad D = \frac{Et^3}{12(1-\gamma^2)} \tag{5.1}$$

$$\frac{Z}{\Delta P} = \frac{a^4}{64D}; \qquad D = \frac{Eh^3}{12(1-\gamma^2)} \tag{5.2}$$

Where a is the radius of the membrane, Δ P is the pressure difference, E is Young's modulus, t is the thickness of the membrane, and γ is the Poisson's ratio.

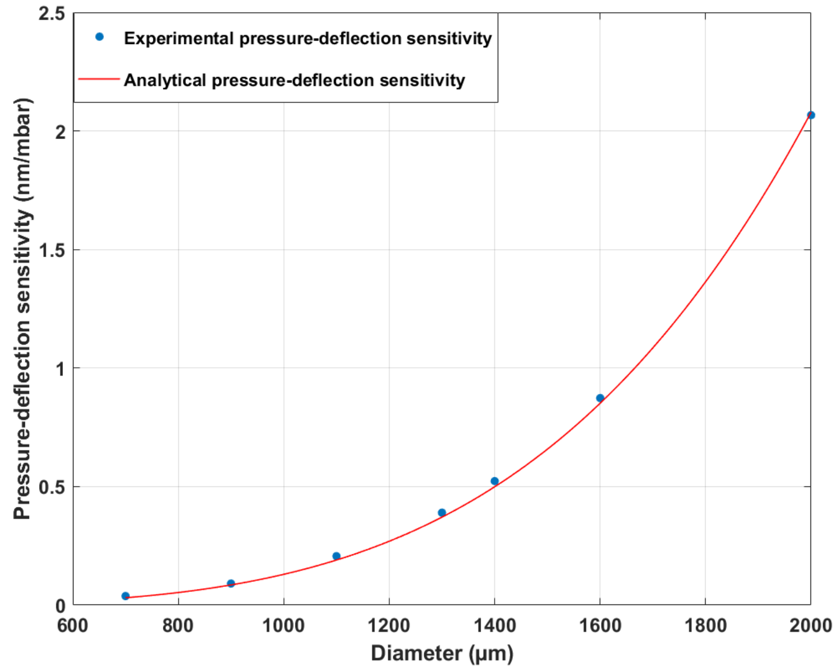

Figure 5.6: Comparison of experimental and analytical pressure-deflection sensitivity using eq.5.2
The used parameters for the analytical equation are: E<100> = 128 Gpa, γ=0.28 and thickness = 40 µm

5.2. Plastic Deformation

While performing the pressure-deflection characterization test, it was observed that the membranes had an inherent plastic deformation. The presence of plastic deformation was first observed in the form of a positive intercept in the fit equations obtained for pressure-deflection curves. Fig.5.10,5.11 and 5.12 shows the fit equations obtained for membranes (of diameter: 2000 µm, 1300 µm, and 700 µm) with intercepts marked with a red box. Here, the positive intercept value indicated there is a residual downward deflection of the membrane at 0 differential pressure.

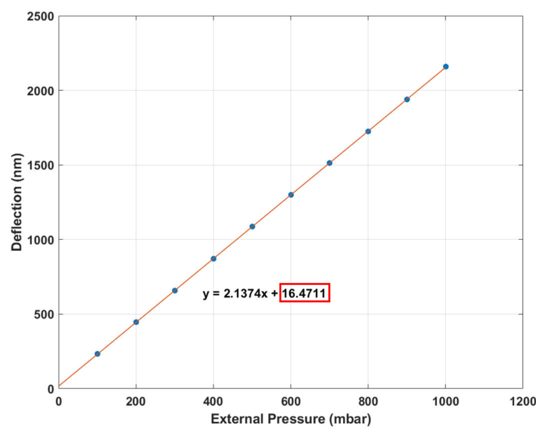

Figure 5.7: Pressure-deflection curve of the membrane having diameter 2000 µm

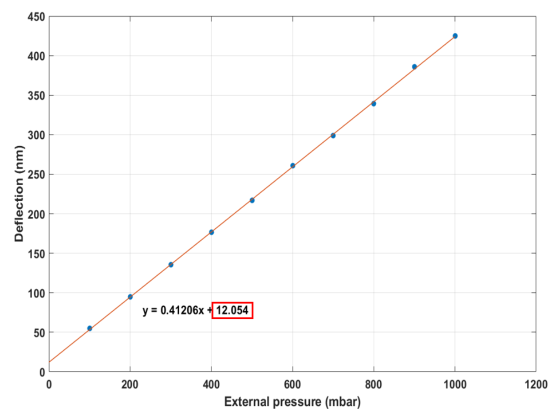

Figure 5.8: Pressure-deflection curve of the membrane having diameter 1300 µm

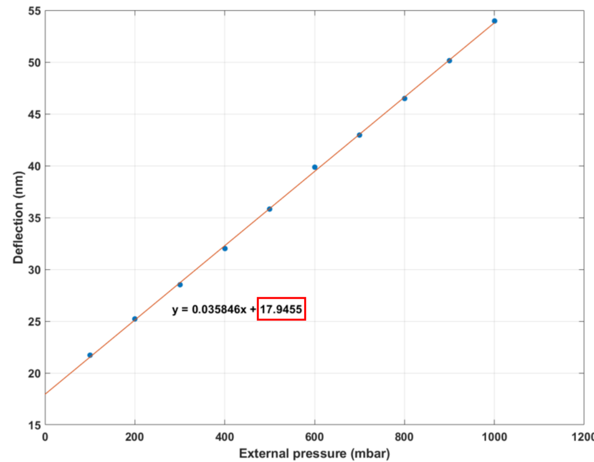

Figure 5.9: Pressure-deflection curve of the membrane having diameter 700 µm

Based on the acquired intercept values, it was not possible to observe a clear trend in the relation between plastic deformation and the diameter of the membrane for a specified thickness. Hence, in order to analyze the residual deflection under conditions of zero differential pressure, we utilized membranes from the cavities that had leak channels. In this experiment, holes were made on the cavity membrane to establish a connection for other cavities through a leak channel, exposing them to atmospheric pressure. Holes were created using the cutting machine with a TALON nanosecond laser with the following set of parameters: diameter of hole=40 µm, laser power: 100 %, cutting speed: 100 rpm, repetitions: 400, and diode current of 7 Amps.

Before the creation of holes, the membranes exhibited a downward deflection due to the elevated ambient pressure exerted externally on the cavity. Once holes are formed, the flow of air molecules into the leak channels begins, resulting in a decrease in the deflection of membranes in adjacent cavities. Two measurements were conducted on the membranes: one before creating the hole to see the initial deflection shape, and another after creating the hole to observe the deflection shape at a differential pressure of zero. In order to make sure that the second measurement corresponds with the deflection profile at zero differential pressure, the measurement was carried out across multiple days in a week to verify the consistency of the deflection shape.

Figures 5.10, 5.11,5.12, 5.13 and 5.14 show the deflection profiles of membranes with diameters of 2000 µm, 1600 µm, 1400 µm, 1100 µm, and 900 µm, respectively. These figures show the deflection shapes of the membranes both before and after the leakage. The experiment yielded the observation that all of the membranes exhibited a residual deflection at zero differential pressure.

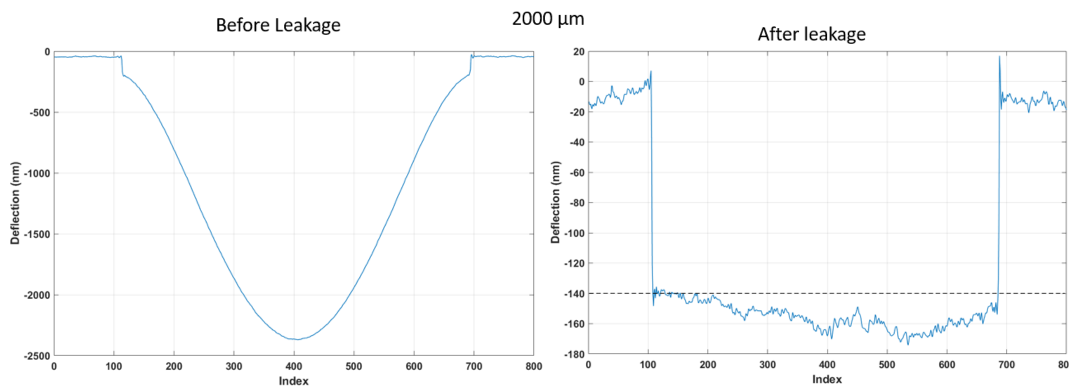

Figure 5.10: Deflection profile of 2000 µm diameter membrane before and after leakage

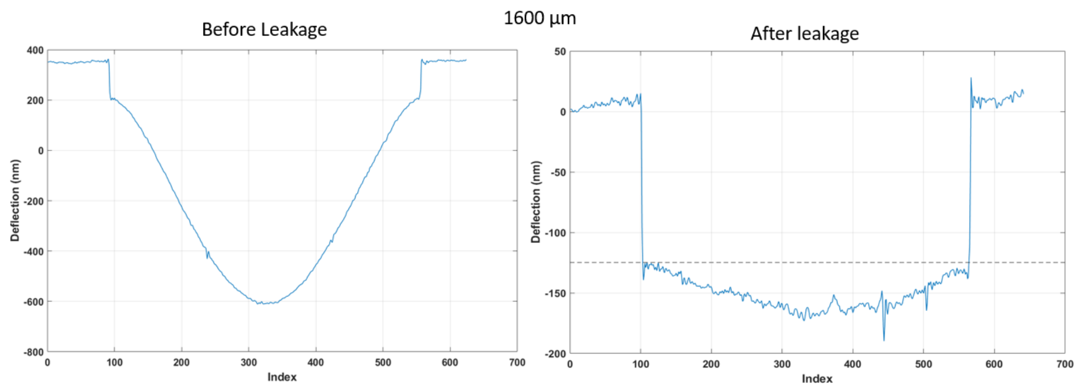

Figure 5.11: Deflection profile of 1600 µm diameter membrane before and after leakage

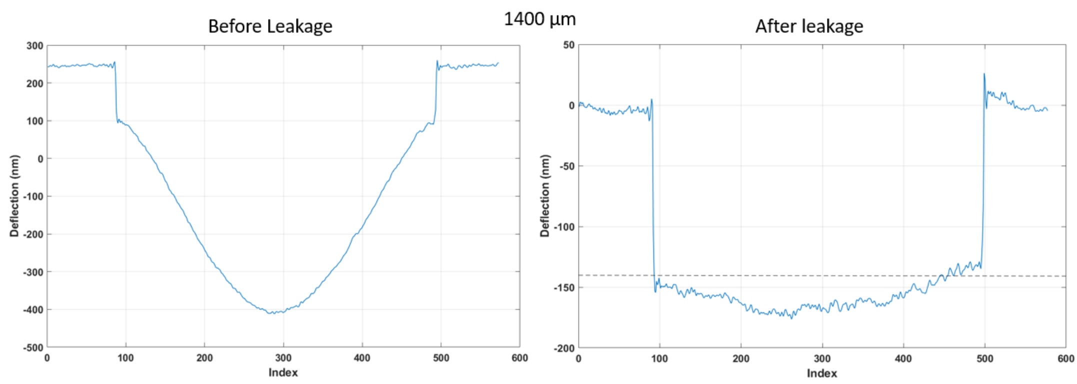

Figure 5.12: Deflection profile of 1400 µm diameter membrane before and after leakage

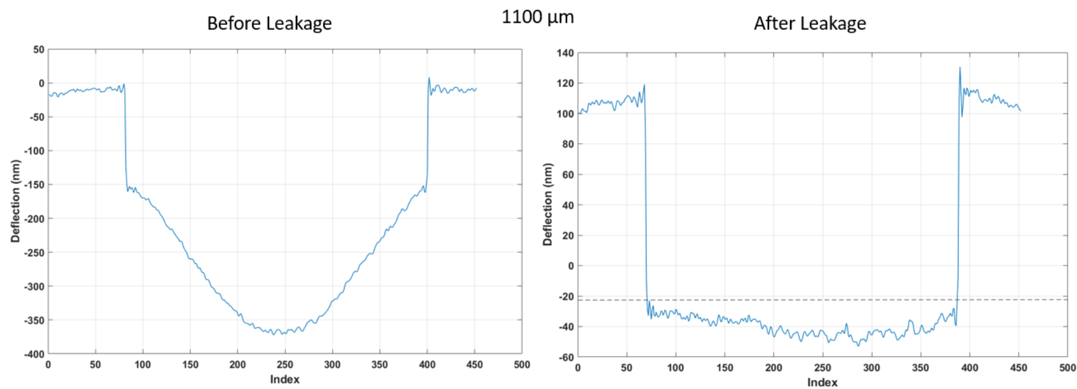

Figure 5.13: Deflection profile of 1100 µm diameter membrane before and after leakage

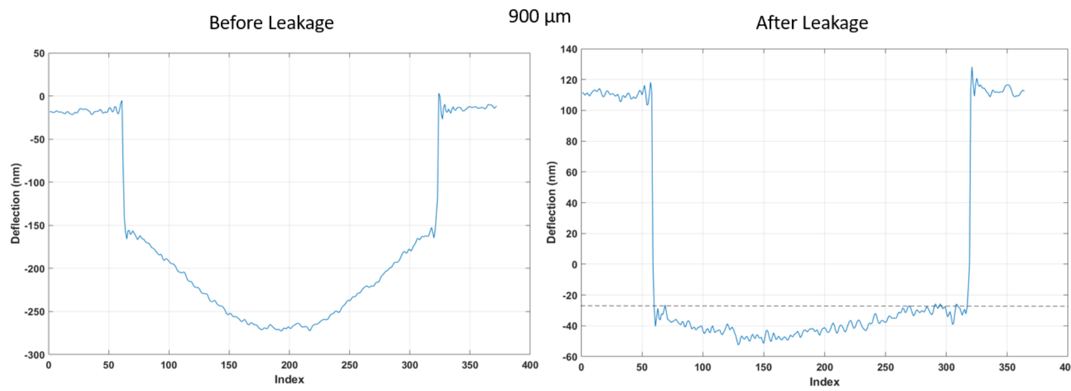

Figure 5.14: Deflection profile of 900 µm diameter membrane before and after leakage

The observed residual deflection did not correspond with the anticipated results derived from the study conducted in the plastic deformation analysis (section 3.4.6).

Based on the analysis of plastic deformation, it was hypothesized that membranes with diameters of 2000, 1600, 1400, and 1300 µm, and a thickness of 40 µm, when bonded to cavities and subjected to annealing temperatures exceeding 1000°C, would experience plastic deformation. As a result, these membranes would exhibit no deflection in response to variations in differential pressure. Nevertheless, it was observed that all of the membranes exhibited deflection changes in response to variations in differential pressure, regardless of their diameter. It is possible that the observed deviation from our initial predictions might be attributed to variations introduced in the fabrication process. In the process of fabrication, the whole 461 μm thick silicon-on-insulator (SOI) wafer was fusion-bonded to the cavity. Subsequently, annealing was performed, and thereafter, the handle layer and the buried oxide layer were removed to provide the appropriate membrane with the necessary diameter and thickness (Fig.4.49). Given that the entire SOI wafer was subjected to bonding and annealing processes, hence, it is possible that it may have avoided plastic deformation, contrary to our previous predictions.

On the other hand, the cause of the residual deflection observed in all the membranes remains uncertain. We suspect that the presence of an oxide layer between the silicon membrane and silicon substrate may contribute to this phenomenon. One possible explanation is that a mismatch in the thermal expansion coefficients between these layers could have resulted in residual stress, ultimately leading to the observed residual deflection. Hence, in the fabrication procedure employed in our project, it was not possible to determine the optimal dimensions for the membrane. Instead, we conducted leak testing on all the test cavities, as elaborated in the subsequent sections.

5.3. Leak testing of cavities with channels

To get a firsthand understanding of the process of leaking in wafer-bonded cavities, our initial approach involved conducting leak tests on cavities that were interconnected by rectangular leak channels. This section provides a detailed account of the methodology employed for conducting leak testing. It presents the leak rate values obtained for various channel sizes and compares them with the analytical leak rates calculated using expressions describing the continuum, slip, and free molecular regimes specific to rectangular channels.

5.3.1. Detailed experimental procedure

In this experiment, holes were once again introduced to the membrane, following the methodology employed in the previous experiment conducted to investigate plastic deformation (Fig.5.15). The holes were generated utilizing the same laser-cutting equipment and maintaining the same parameter configuration as applied during the plastic deformation experiment. Holes were created on membranes of cavities, which serve as openings through which the interconnected cavities communicate via leak channels of varying dimensions. All the tested leak channels were of depth equal to 34 nm, but the length and width varied as shown in the fabrication section (Fig.4.51 and in Fig.4.52).

After the holes were formed, it was observed that air molecules quickly entered the leak channels, resulting in a faster decrease in deflection for all the membranes (Fig.5.16). Consequently, we faced challenges in quantifying the reduction in deflection from the moment when hole development on the membranes commenced and leakage initiated. Therefore, to quantify the deviation from the initial point of leakage, a different methodology was utilized. The experimental procedure entailed the placement of the cavities within our vacuum chamber setup, as shown in Fig.4.45. The cavities were then exposed to the lowest possible external pressure. The current investigation yielded an observed minimum achievable pressure of around 10 mbar.

Through the reduction of external pressure, the air molecules that had previously entered the cavities were removed, so enabling the membrane to deflect and reach a condition of zero difference (Fig.5.17). Following the completion of this step, the vacuum chamber is then vented out to attain atmospheric pressure. As a consequence of the increased external pressure, the membranes undergo a downward deflection and subsequently begin leaking. Upon the release of the vacuum chamber into the environment, we began the measurement of the deflection of all membranes in the die by adjusting the X-Y stage platform of DHM (Fig.5.18). By employing this methodology, it becomes feasible to properly record the progressive reduction in deflection over a period of time, especially commencing from T=0 (approximately). As a result, this facilitated our comprehension of the decrease in deflection that occurs as a consequence of a leak.

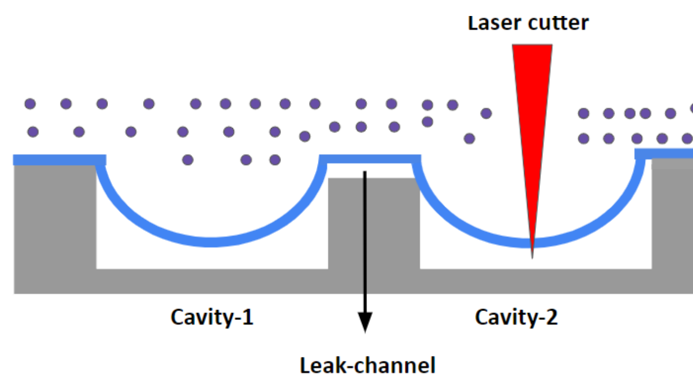

Figure 5.15: Hole generation on the membrane to open the cavity to atmospheric pressure

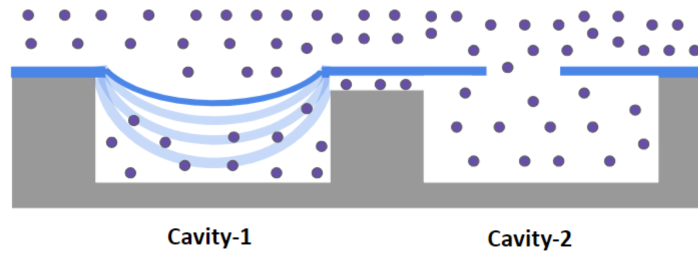

Figure 5.16: Reduction of membrane deflection due to immediate ingress of air molecules into the leak channel

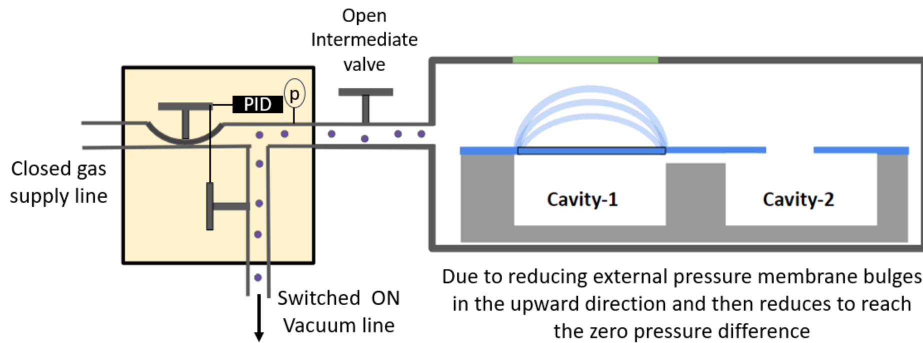

Figure 5.17: Evacuation of vacuum chamber

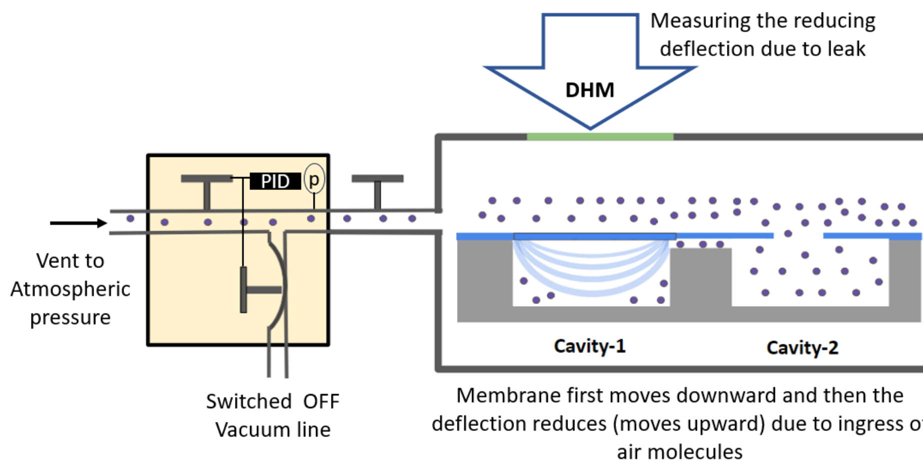

Figure 5.18: Venting of the vacuum chamber and measurement of reducing deflection

The measuring procedure involves gathering data sequentially for each membrane, beginning with membrane -1 and proceeding to membrane -2, membrane -3, membrane -4, etc. The assigned numbers for all membranes are shown in Fig.5.19. After collecting the initial set of measurement data for each membrane, second measurements were conducted, beginning with membrane-1 again and proceeding progressively through the remaining membranes. Using this cyclic technique, we measured the deflection of each membrane. In order to observe the deflection behavior of each membrane, nearly 6 hours of measurements were conducted. This allowed us to gather a substantial quantity of data for deflection.

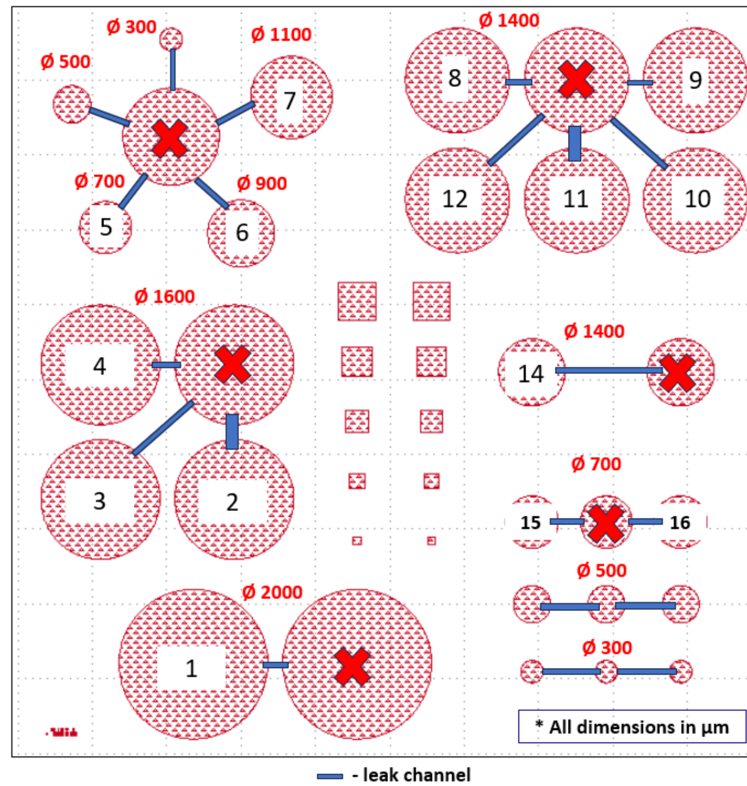

Figure 5.19: Numbers allotted for all membranes in die and red cross indicates the membranes indicates where holes are created Dimensions of the leak channels can be verified from Fig.4.51 and 4.52

5.3.2. Deflection measurement results

During the course of this experiment, it was seen that for some of the membranes, it was not possible to observe a time-dependent change in deflection, indicating that not all channels experience leakage. We suspect that the observed occurrence might potentially be attributable to the irregular topography of the leak channels, as shown in the SEM images (Fig.4.57 and Fig.4.58). It is anticipated that the presence of notches on the walls and surfaces of the leak channel may have obstructed the passage for air molecules to flow. Despite this challenge, we successfully measured deflection for certain membranes over time, wherein the leakage seemed to have happened via the channels. The deflection data acquired for membranes of varying diameters is presented in the following cases.

1. Fig.5.20 shows the deflection measurements acquired for a membrane with a diameter of 2000 µm. The acquired data was well fitted using the exponential fitting equation in the form of a.e^{bx} in MATLAB. The obtained fit equation closely resembled with exponential decay function (eq.3.12) which we derived for deflection in section 3.1. This observation provides confirmation supporting the correctness of the equation we formulated to establish a connection between the leak rate (dN$_{in}$/dt) and deflection rate (dZ/dt) (eq.3.9). Consequently, this equation can be utilized to calculate leak rates based on deflection data obtained from the experimental measurements. The calculation of experimental leak rates is explained in the next section.5.3.3.

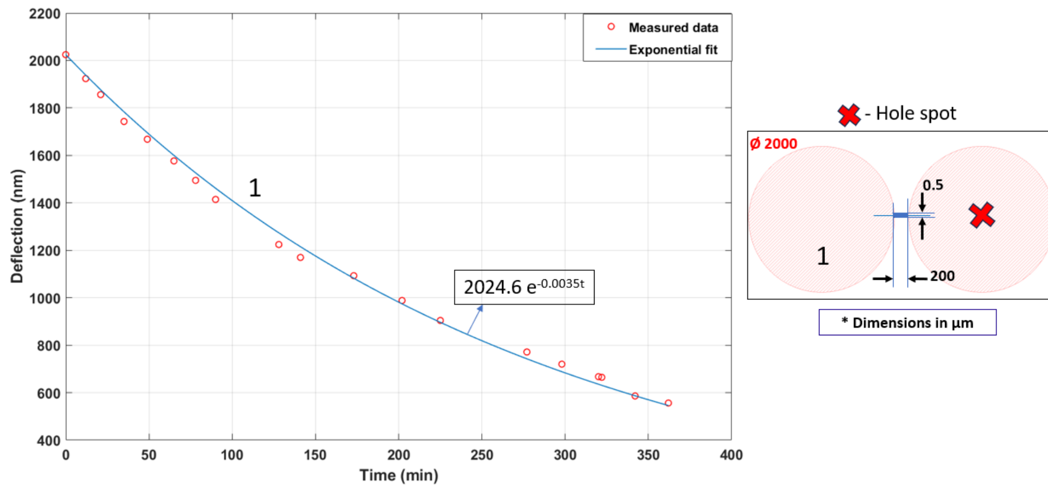

Figure 5.20: Deflection measurements of 2000 µm diameter membrane

2. Fig.5.21 shows the deflection measurements acquired for membranes with a diameter of 1400 µm. Here, we had evident observations of how the rate of reduction in deflection varies with varying leak channel sizes. The membrane (11), which is connected to the widest leak channel (W-100 µm x L-200 µm x H-34nm), exhibited the most rapid decrease in deflection. In contrast, the membrane (12), which is connected to the longest leak channel of size: W-1 µm x L-862.74 µm x H-34nm, demonstrated the slowest reduction in deflection. Additionally, it was observed that channels of equal length and height but varying widths exhibited differing rates of reduction. Specifically, membrane-11 showed a faster rate of reduction than membrane-8 (connected with a leak channel of size: W-1 µm x L-200 µm x H- 34nm), which exhibited an even faster rate of reduction than membrane-9 which is connected with a leak channel of size: W-0.5 µm x L-200 µm x H- 34nm.

In the case of membranes exhibiting the most rapid decline in deflection (specifically, membrane 11 and membrane 8), it was once again observed that they did not achieve a deflection value of zero with an increase in time. Instead, these membranes showed the presence of residual deflection possibly due to plastic deformation, as shown in the plastic deformation section (see Section 5.2) for various other membranes. Therefore, to fit these data, we slightly modified the exponential fitting equation with constant term c, in the form of a.e^{bx}+c, in order to capture the residual deflection value as well.

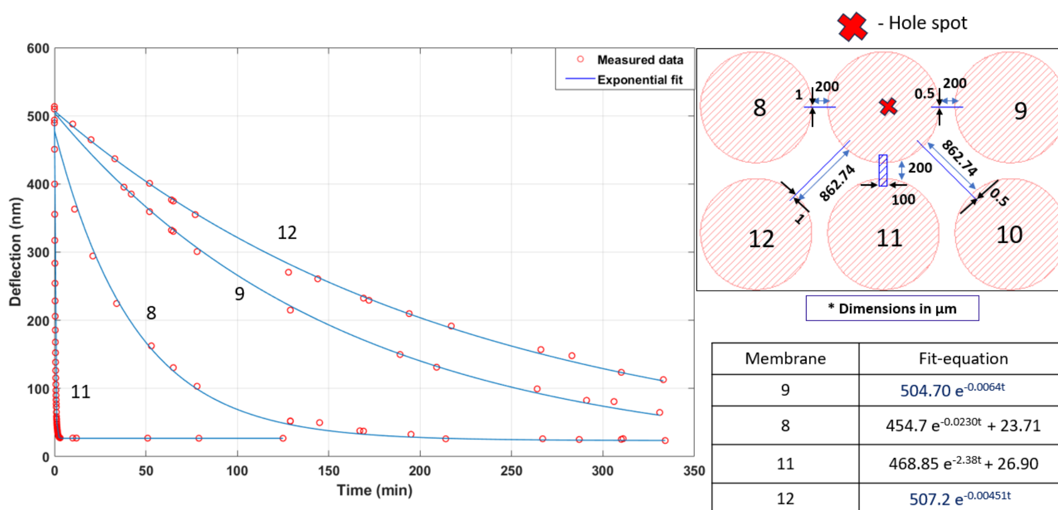

Membrane	Fit-equation
9	504.70 e$^{-0.0064t}$
8	454.7 e$^{-0.0230t}$ + 23.71
11	468.85 e$^{-2.38t}$ + 26.90
12	507.2 e$^{-0.00451t}$

Figure 5.21: Deflection measurements of 1400 µm diameter membranes

3. In order to see the same trend in deflection reduction as we saw for 1400 µm membranes, we did the same leak testing experiment for channels connected with 1600 µm diameter membranes. Fig.5.22 shows the deflection data obtained for 1600 membranes over time. In this case, it was again observed that the membranes (2) connected with the widest leak channel (of size W-100 µm x L-200 µm x H- 34nm) had the fastest reduction in deflection, as we observed for membrane - 11 of 1400 µm diameter and the membrane (3) connected with longest leak channel (of size W-1 µm x L-945.58 µm x H- 34nm) had the slowest decay in deflection as it is observed for membrane - 11 of 1400 µm diameter. Here also, we observed the residual deflection of membranes, especially for membranes 4 and 2. This eventually indicated that those membranes reached the 0 pressure difference state.

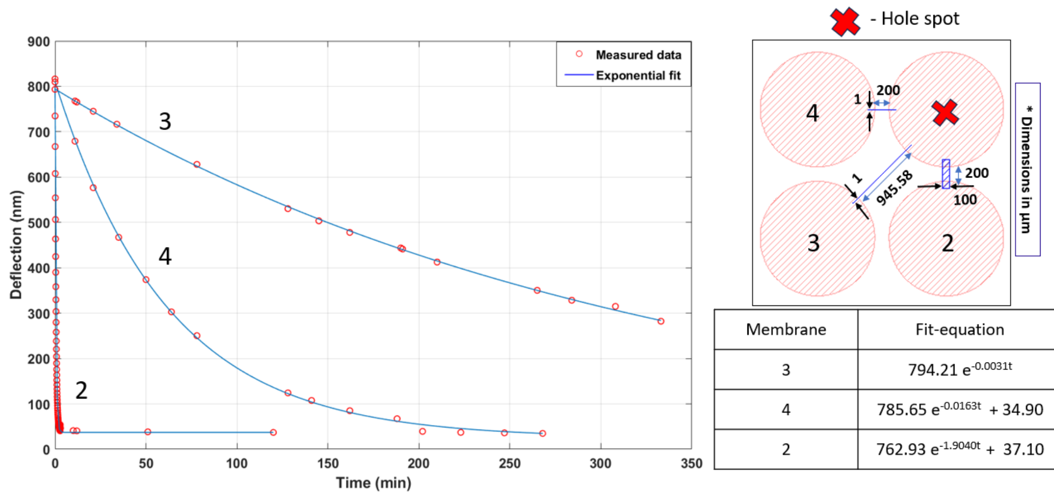

Membrane	Fit-equation
3	794.21 $e^{-0.0031t}$
4	785.65 $e^{-0.0163t}$ + 34.90
2	762.93 $e^{-1.9040t}$ + 37.10

Figure 5.22: Deflection measurements of 1600 µm diameter membranes

5.3.3. Calculation of experimental leak rate and comparison with theory

To understand whether the leakage has occurred through the channels of concerned dimensions, we calculated the experimental leak rates based on the deflection data points obtained from measurements. This experimental leak rate is then evaluated against the expressions for a steady mass flow rate through long micro/nanoscale channels that were developed for continuum, slip, and free molecular flow regimes.

- **Procedure for calculating experimental leak rate**: For the calculation of experimental leak rate, we used the eq.5.3 derived for circular membrane, which is given by:

$$-\frac{dZ}{dt} = (\frac{a^4}{64D})(\frac{RT}{V_{eff}})(\frac{dN_{in}}{dt}) \tag{5.3}$$

To calculate the leak rate (dN_{in}/dt), we need to calculate the deflection rate (dZ/dt). The experimental dZ/dt is calculated using two adjacent deflection data points: Z1 and Z2 at t1 and t2 such that dZ/dt = (Z2-Z1)/(t2-t1) at the time t_{avg} = (t1+t2)/2. Since V_{eff} is also dependent on Z, therefore this parameter is also considered as an average value such that at t = t_{avg}, V_{eff}=(V_{eff} (at Z1) + V_{eff} (at Z2)) / 2. The remaining parameters in eq.5.3 are constant, therefore we calculate (dN_{in}/dt) at every average time t_{avg}.

- **Procedure for calculating analytical leak rate**: To calculate the analytical leak rate, the expressions defined for a tubular channel (in section 2.2.1) cannot be applied to a rectangular channel. In this case, we used expressions presented by Gallis, M. A., and J. R. Torczynski. [56] for channels having width W large relative to the channel height H and for the consideration that the gas flow is fully developed.

As mentioned in the section 2.2.1, the principal parameter for gas flow conditions is the K_n which characterizes the degree of rarefaction. The continuum regime is donated by the subscript C and has K_n<0.001. The **mass flow rate in the continuum regime** is given by:

$$\dot{M_C} = \frac{2WH^3p_m}{3\pi\mu c^2 L}(p_1 - p_2) \tag{5.4}$$

Here, μ is the dynamic viscosity, c is the mean thermal speed $\sqrt{\frac{8RT}{\pi M}}$ and p_m is the mean pressure in a channel with external pressure p_1 and internal pressure p_2. The slip regime is denoted by the subscript S and has K_n = 0.001-0.1. The **mass flow rate in the slip regime** is given below:

$$\dot{M_S} = \dot{M_C}(1 + \frac{6p_\lambda}{p_m}\bar{\omega_S}) \tag{5.5}$$

$$\bar{\omega_S} = \frac{2-\alpha}{\alpha}(1 + b_1\alpha) \tag{5.6}$$

Here, p_λ is the pressure at which K_n = 1, which is equal to $p_\lambda = \frac{\pi\mu c}{4H}$ and ω_S is the slip function which includes the tangential accommodation coefficient α. The free-molecular regime is denoted by the subscript F and has K_n > 10. The **mass flow rate in the free molecular regime** is given by:

$$\dot{M_F} = \dot{M_C}(\frac{6p_\lambda}{p_m})\omega_F = \omega_F\frac{WH^2}{cL}(p_1 - p_2) \tag{5.7}$$

$$\bar{\omega_F} = \frac{2-\alpha}{\alpha}(1 + b_1\alpha) \tag{5.8}$$

Here, $\bar{\omega_F}$ is the free-molecular function, which includes accommodation effects through α, entrance-length effects through ϵ and channel cross-section effects through b_0. The terms α, ϵ, b_0 and b_1 are the fitting parameters to determine the behavior of the mass flow rate in the free-molecular, slip, and transition regimes, respectively.

α, the tangential momentum accommodation coefficient deals with the interaction of gas molecules with the contacting surfaces. If the surfaces were perfectly smooth, specular or perfect reflection would be observed, that is, the molecules striking the surface at any angle ϕ ([57]) would rebound, conserving the velocity parallel to the surface, but having the component of velocity perpendicular to the surface reversed.

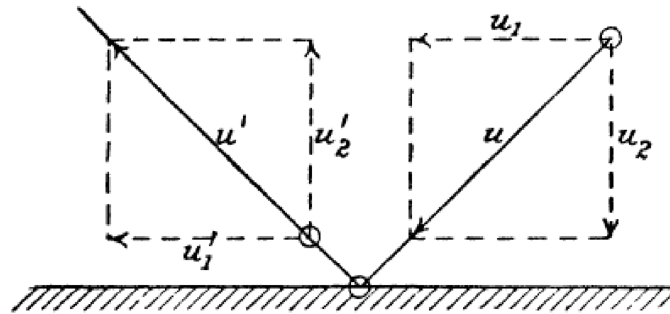

Figure 5.23: Illustration of molecules striking the surfaces of the channel and exhibiting the specular reflection [57]

With such reflection, the only force on the wall would be the pressure normal to it. The velocity at the surface would then be the velocity of flow along the wall (i.e., there would be no drag, α would be 0, and the gas would flow down the channels with no action on the walls), that is, its velocity through the cross-section of the tube would be uniform. This is not the case when there is friction along the walls. This means that there must be some mechanism by which the gas is retarded by the walls. If the walls were composed of spherical gas molecules at rest with large spaces between them, the molecules striking such a wall would lose their momentum, on average, they would be reflected as if they had velocities after reflection equally probable in all directions (diffusive flow). With such a process occurring, the gas would still have a velocity of slip. In such a case, the velocity at the wall would be less than that in the center and the gradient could be calculated. In general, α varies between 0 (specular reflection) and 1 (perfectly diffusive flow) [58]. Since

our leak channels are observed to be rough (Fig.4.57 and Fig.4.58), we considered the value of α as 1.

The parameter b_1 describes the slip regime. Matching the slip coefficient for unity accommodation (α = 1) to known theoretical values suggests that the parameter b_1 = 0.15 ± 0.03 for a wide variety of molecular interactions [59], [60]. For our analytical calculations, this parameter is chosen to be 0.15.

The product ϵb_0 is chosen in such a way that the mass flow rate approaches the correct value in the free-molecular regime. Based on the literature, it was observed that in most of the cases for a long channel length (L»H), the value of ϵ is assigned as 1 [57], [61]–[63]. Since, in our case, the minimum length of the channel is 200 µm, which is several times greater than 34nm channel height, therefore we also considered ϵ as 1. Having assigned values for 3 out of 4 fitting parameters, the last parameter b_0 is adjusted so that the analytical leak rate matches with the experimental leak rate.

As a last step, the pressure difference (p_1 - p_2) present in the analytical flow rate equations, is calculated using the deflection values obtained in our experiment with the help of pressure-deflection analytical eq.3.16. Also, the flow-rate equations presented for different regimes are in the unit of Kg/sec. To convert them to the unit of mol/sec, those equations are divided by the molar mass (M) of the air molecule, which is equal to 28.63×10^{-3} Kg/mol. The other values of constants used in those equations are as follows: $\mu = 18.25\times 10^{-6}$ Pa.Sec (for air), R=8.314 (J/mol.K). All the deflection measurements are conducted at an environmental temperature of 20 degrees C, the considered value of T is 293.15 K.

Comparison of experimental leak rate with analytical flow rate for different leak channel sizes are shown in the following cases. In all the cases, analytical leak rates are calculated using equations for the continuum regime, slip regime, and free-molecular regime. Both analytical leak rates and experimental leak rates are plotted against the pressure difference calculated using experimental deflection measurements.

1. Leak channel of size W:100µm x L:200 µm x H:34nm: Fig.5.25 shows the leak-rate plots for membranes having 1400 µm diameter (11) and 1600 µm diameter (2). This specific channel possesses the biggest width and the shortest length when compared to all other channels. The deflection measurements corresponding to membranes showed that they have a residual deflection (Fig.5.21 and Fig.5.22) at increased time. This indicated that they had reached the 0 pressure difference state. To account for this in the leak rate calculation, we calculated the pressure difference at corresponding residual deflection values for 1400 µm (11) and 1600 µm (2). These pressure-difference values are subtracted from all the values calculated for other deflections measured for the corresponding membranes. By doing this, it was observed that the deflections were not exactly measured from the point where p_1 = 0 and p_2 = 1000 mbar (Approx.), but rather from a time where some amount of air molecules had already entered into the cavities.

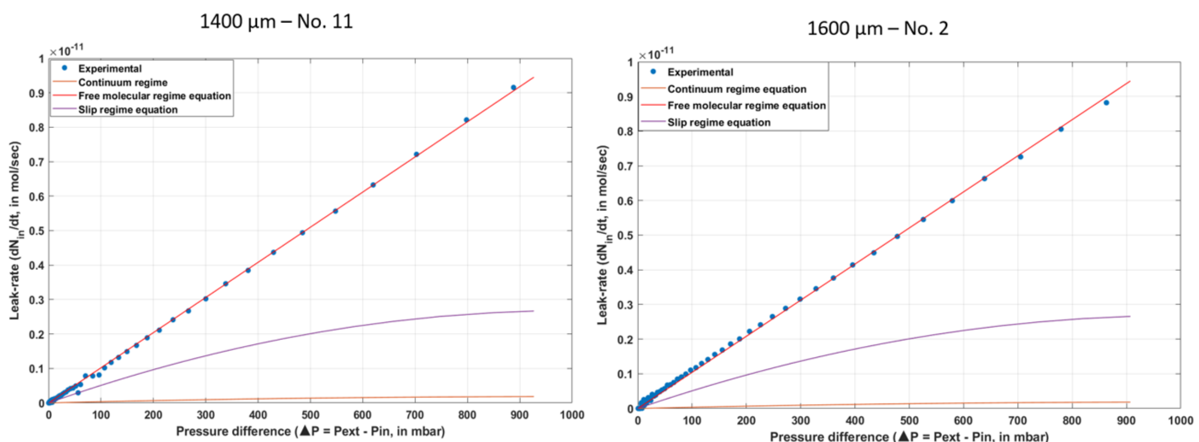

Figure 5.24: Leak rate calculated from the continuum, slip, free-molecular equations and leak rate calculated from deflection measurements are plotted against the pressure-difference, which is calculated based on deflection measurements obtained for leak channel size of W:100µm x L:200 µm x H:34nm

The fitting parameters used for the flow regime equations are as mentioned above: α=1, ϵ=1, b_1=0.15. For this channel size, by assigning b_0=2.4, it was observed that the analytical leak rate obtained using the free-molecular regime equation clearly overlays with the experimental leak rate values. This observation suggests that the flow resistance remains constant and is primarily influenced by the dimensions of the leak channel (eq.5.7). At extremely low-pressure differentials, it was noted that the leak rate values obtained from both slip-regime and continuum regime equations were also in agreement with the experimental values. This occurrence arises due to the drop in pressure differential, resulting in a reduction in the mean free path (λ) of air molecules as described by eq. 2.10. Consequently, this decrease in the λ leads to a decrease in the Knudsen number (K_n = λ / H, for a rectangular channel). When the K_n decreases, slip flow, and continuum flow become significant. The agreement between the values derived from the slip flow and continuum flow equations and the experimental values suggests that, in situations at extremely low-pressure differentials, the resistance to flow is influenced not only by the dimensions of the channel but also by the internal and external pressures (as indicated by eq.5.4 and 5.5).

2. Leak channel of size W:1µm x L:200 µm x H:34nm: Fig.5.25 shows the leak-rate plots for membranes having 1400 µm diameter (8) and 1600 µm diameter (4). Membranes (1400 µm - 8 and 1600 µm - 4) that were connected to this leak channel size were again observed to have the residual deflection at 0 differential pressure (Fig.5.21 and Fig.5.22). Therefore, the method we used for the previous leak channel size to calculate the pressure difference was also applied to this case. For this leak channel size, the calculated maximum leak rate is in the order of 10^{-14} which is 3 orders of magnitude less than what we calculated for the previous channel size (which is the order of 10^{-11}). The appropriate fitting parameters used in this case are α=1, ϵ=1, b_1=0.15 and b_0 = 2. In this case, again it was observed that at very low-pressure differences, the values obtained from the slip flow equation and continuum equation matched the experimental leak rates.

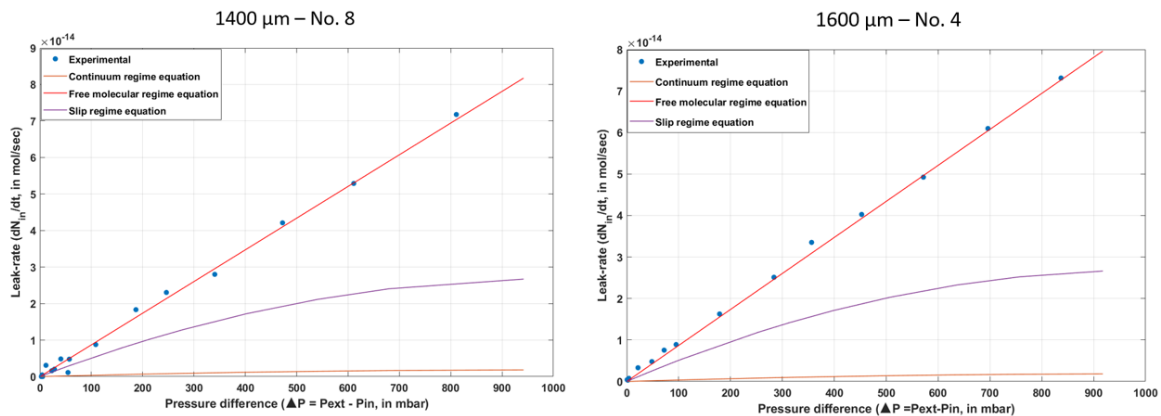

Figure 5.25: Leak rate calculated from the continuum, slip, free-molecular equations and leak rate calculated from deflection measurements are plotted against the pressure-difference, which is calculated based on deflection measurements obtained for leak channel size of W:1µm x L:200 µm x H:34nm

3. Leak channel of size W:0.5µm x L: 200 µm x H:34nm: Fig.5.26 shows the leak-rate plots for membranes having 1400 µm diameter (9) and 2000 µm diameter (1). For this dimension of the leak channel, we observed that the rate of deflection reduction was slower than for membranes connected to leak channels in previous cases (notably for 1400 m membranes; see Fig.5.21). Therefore, we were unable to observe any residual deflection corresponding to a differential pressure of zero.

For the fitting parameters, we used the same α, ϵ, and b_1 values as in previous cases. Here, b_0 = 1.67 had been found to be the most suitable parameter. Since we did not measure the deflection until the 0 pressure difference, neither did the calculated leak rates. As a result, there was a small difference between the experimental leak rate and the leak rate calculated from the slip regime equation and a large difference between the experimental leak rate and the leak rate calculated from the continuum regime equation.

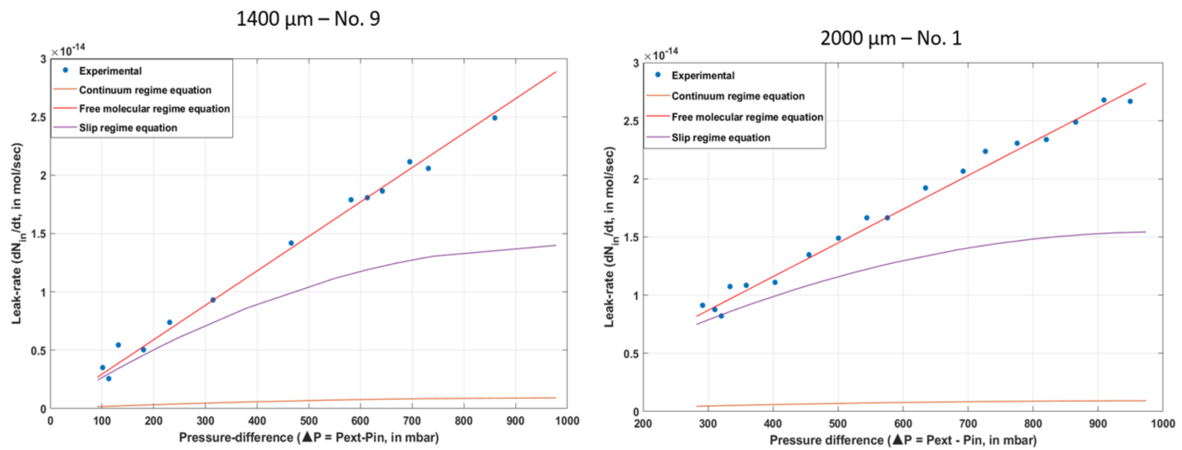

Figure 5.26: Leak rate calculated from the continuum, slip, free-molecular equations and leak rate calculated from deflection measurements are plotted against the pressure-difference, which is calculated based on deflection measurements obtained for leak channel size of W:0.5µm x L:200 µm x H:34nm

4. Leak channel of size W:1µm x L: (945.58 µm and 862.74 µm) x H:34nm: Fig.5.26 shows the leak-rate plots for membranes having 1400 µm diameter (12) and 1600 µm diameter (3). Among all the channels, these 2 membranes are observed to have the slowest rate of reduction in deflection due to their longest lengths (Fig.5.21 and Fig.5.22). Consequently, the measured deflections did not attain the state of zero differential pressure.

For these two leak channels, the fitting parameters used in this case are α=1, ϵ=1, b_1=0.15. Specifically, it was observed that b_0=2 is the appropriate fitting parameter. This is as same as what we used for the case with the leak channel of size W:1µm x L:200 µm x H:34nm, which indicated that the value of b_0 depends on the cross-section of the channel irrespective of length. In this instance, the minimum pressure difference calculated is greater than what was calculated for the preceding escape channel case. As a consequence, we observed an increase in the gap between the experimental leak rate and the leak rate predicted by the slip regime equation, indicating that the free molecular regime flow is the dominant flow for these pressure differences.

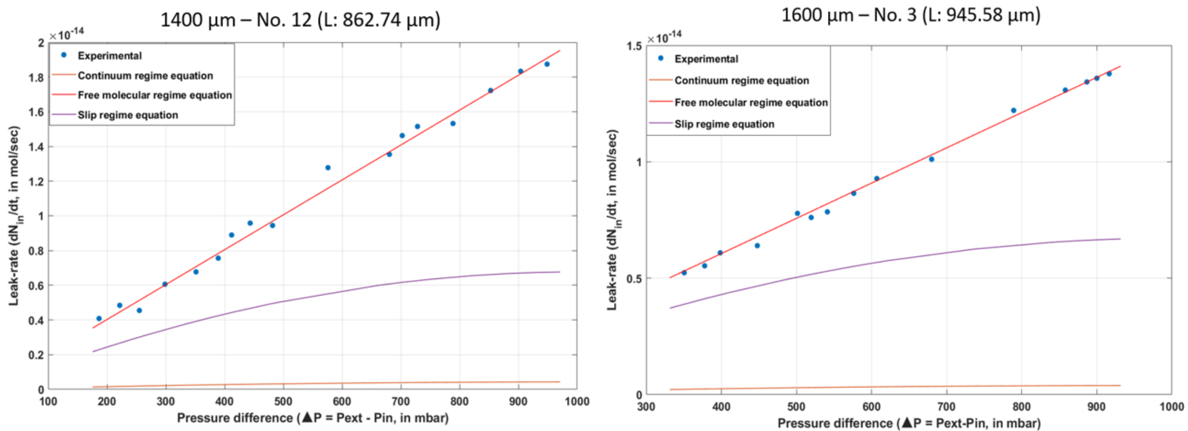

Figure 5.27: Leak rate calculated from the continuum, slip, free-molecular equations and leak rate calculated from deflection measurements are plotted against the pressure-difference, which is calculated based on deflection measurements obtained for leak channel size of (A) W:1µm x L:862.74 µm x H:34nm (B) W:1µm x L:945.58 µm x H:34nm

5.3.4. Summary

To demonstrate how leakage works in the wafer-bonded cavities, We prepared wafer-bonded cavities connected with nanometer gap channels of different dimensions. Despite the challenge that some of the leak channels did not exhibit any leakage or leakage was slow which could not able to measured within a specific period of time, we were able to measure the deflection of membranes that were connected to channels of other different sizes: 1) W:100µm x L:200 µm x H:34nm, 2) W:1µm x L:200 µm x H:34nm, 3) 0.5µm x L: 200 µm x H:34nm, 4) W:1µm x L: 862.74 µm x H:34nm and 5) W:1µm x L: 945.58 µm x H:34nm. From these measurements, it was understood that with the ingress of air molecules into the cavities, the membranes exhibit an exponential rate of reduction in deflection over time. From the experimental leak rate calculations, we observed that the maximum leak rate was in the order of 10^{-14} mol/sec for channels - 2,3,4 and 5, whereas, for the widest leak channel-1, the leak rate was observed to be in the order of 10^{-11} mol/sec. Also, it was understood that the obtained leak rate is not based on the size of the cavity or the size of the membrane diameter but based on the size of the leak channel.

Further, an attempt was made to compare the experimental leak rates with the leak rates derived from analytical flow models that are based on the continuum regime, slip regime, and free-molecular regime. Besides the known gas properties, geometric dimensions, and the accommodation coefficient (α), these expressions in addition contain 3 dimensionless parameters (ϵ, b_1 and b_0).The values for two parameters (ϵ, b_1) are selected by taking into account information from literature sources and the last parameter b_0 is determined by adjusting their values. The functional relationship between the values of ϵ, b_1, and b_0 could not be determined. However, by adjusting the values of b_0, it became possible to observe a good agreement between the experimental leak rate and the analytical model. This suggests that the leakage likely occurred mainly through the established leak channels between the cavities.

5.4. Leak testing of sealed-off cavities

Having conducted the leak testing of cavities with defined leak paths, in this section, we report the deflection measurement results of leak testing conducted for cavities with sealed-off cavities (or with no defined leak paths). Further, the section extends with the leak rates obtained from the calculations and finally, a discussion is made based on the calculated leak rates.

5.4.1. Experimental Results

In this final experiment, we first tested for cavities whether they exhibit any outgassing or leakage under the presence of air.

Since in our previous experiment case, we conducted leak testing of cavities under the pressure of atmospheric pressure of air. In this experiment, there was an initial thought of whether air molecules could enter the seal-off cavities. Therefore to check for outgassing or air leakage, we measured the deflection of different membranes from Day 1 to Day 8. The results of the measurements are provided in the appendix.E

From the measurements, it was observed that there was no significant change in deflection which indicated there was no outgassing and air leakage during this period of time. Now they are tested for helium leakage. The steps followed for helium testing are explained in the section.4.5. The helium gas supply is used from the helium gas cylinder which is connected Pfeiffer leak detector ASM-340. The helium gas supply has a control knob that can provide up to maximum output pressure of 1000 mbar and that is the reason why we set 1000 mbar of helium pressure inside the chamber. By setting it at 1000 mbar, in another way, we also made sure that none of the atmospheric air molecules entered the vacuum chamber.

After sending helium to the vacuum chamber, we were able to effectively measure deflection reduction for some of the membranes in a die, which are shown in Fig.5.28. The measurements were taken for almost 14 days and they are shown in Fig.5.29, Fig.5.30 and Fig.5.31 for membranes having diameter 2000 µm, 1600 µm,1400 µm, 1300 µm and 1100 µm. All the day-0 measurements in the graph correspond to the day-8 deflection measurement provided in the tables presented in appendix.E.

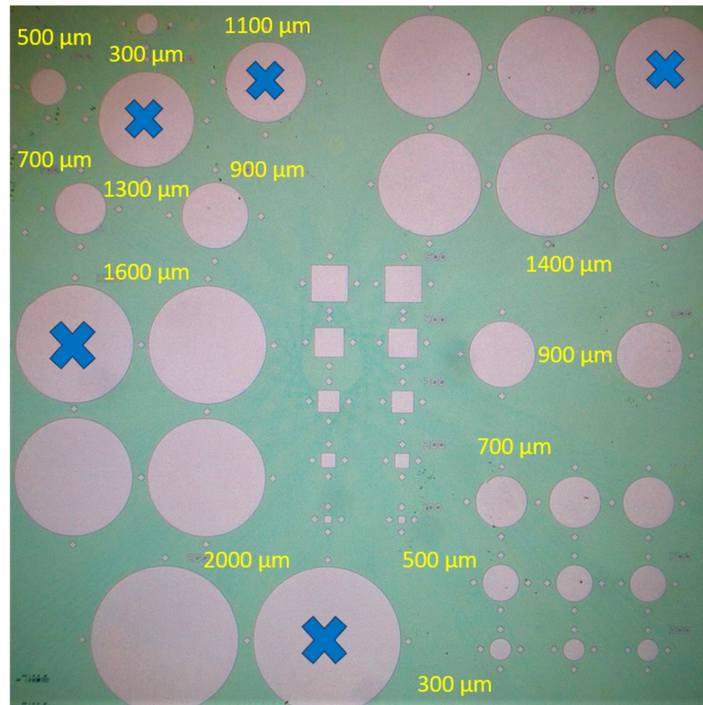

Figure 5.28: Keyeence microscope image of the tested die and the measured diameters in the die are indicated by blue cross mark

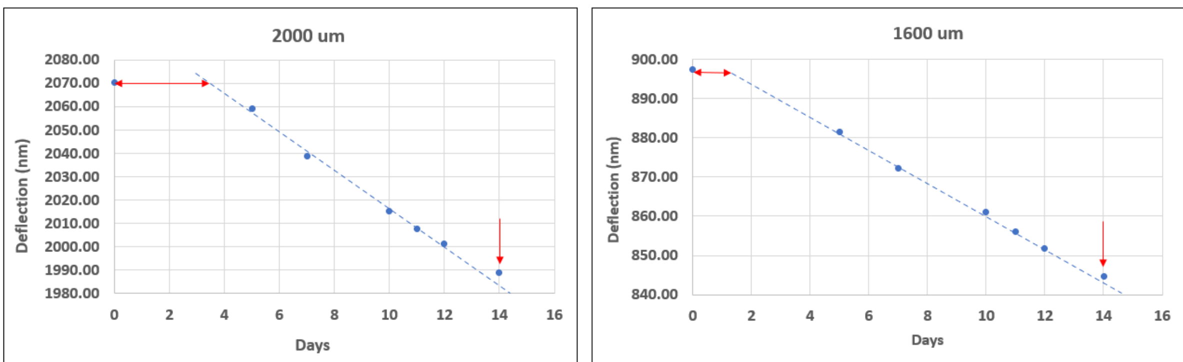

Figure 5.29: Deflection measurements of 2000 µm and 1600 µm diameter membrane under helium gas pressure

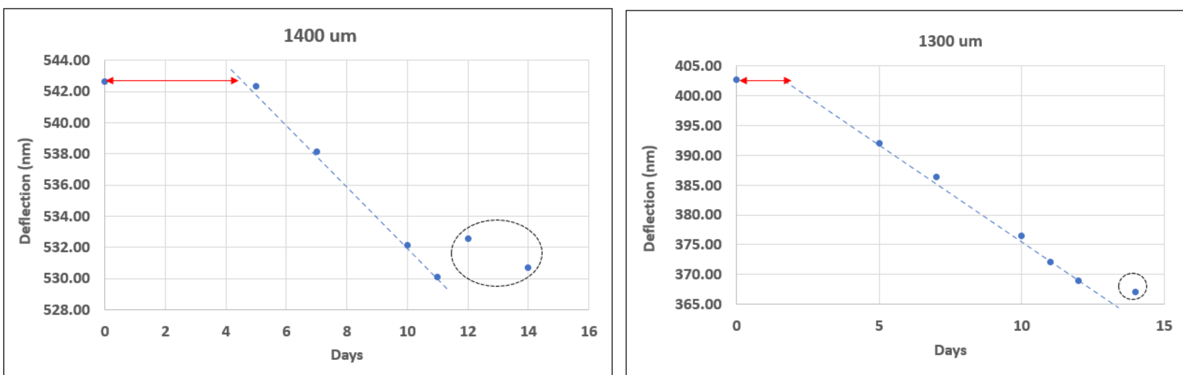

Figure 5.30: Deflection measurements of 1400 µm and 1300 µm membrane under helium gas pressure

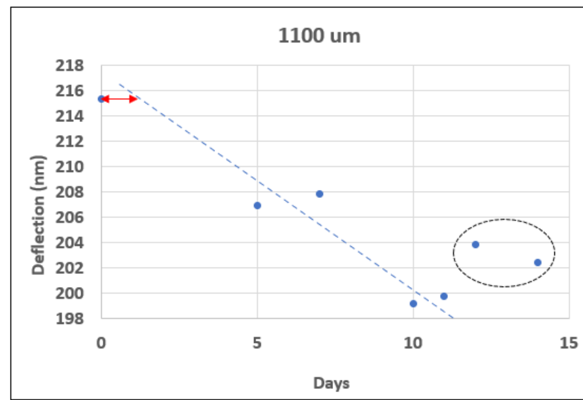

Figure 5.31: Deflection measurements of 1100 µm membrane under helium gas pressure

5.4.2. Calculation of leak rates

During the measurements, it was observed that the helium took some amount of time to enter into the cavities to indicate leakage. This is indicated by the double-headed red arrow mark in the graphs. At the same time, as the number of. days increased it was observed that the deflection of the membranes again increased (shown in the vertical red arrow mark and dotted circles), it was suspected that helium inside the vacuum chamber was replaced by air, and helium inside the cavity began to come out and as a result, deflection started increasing. Therefore, to calculate the leak rate, only the deflection data points that exhibited a linear rate of reduction were considered. Since there are only a few data points obtained, these data points are linear fitted to obtain the rate of deflection and calculate the corresponding leak rate using eq.5.3. In this case, it was able to perfectly apply the linear fitting for membranes having diameters from 2000 µm to 1300 µm, but for 1100 µm, the linear fitting appeared to be not perfect, it seemed that deflection needed to be measured for some more days to observe the trend of reduction, nevertheless, we tried to fit the obtained data using linear equation and see how much leak rate it gives.

Slope in Fig.5.32, Fig.5.33 and Fig.5.34 indicate the deflection rate obtained for each diameter.

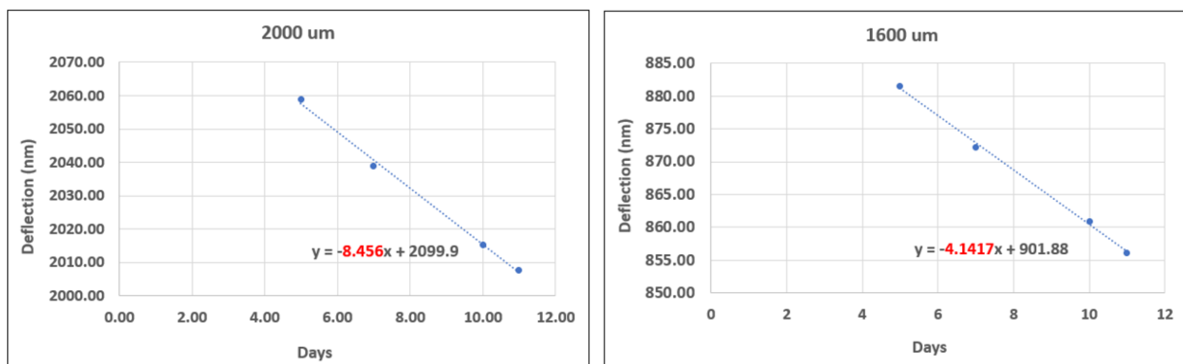

Figure 5.32: Linear fitting of deflection data points for 2000 µm and 1600 µm diameter membranes

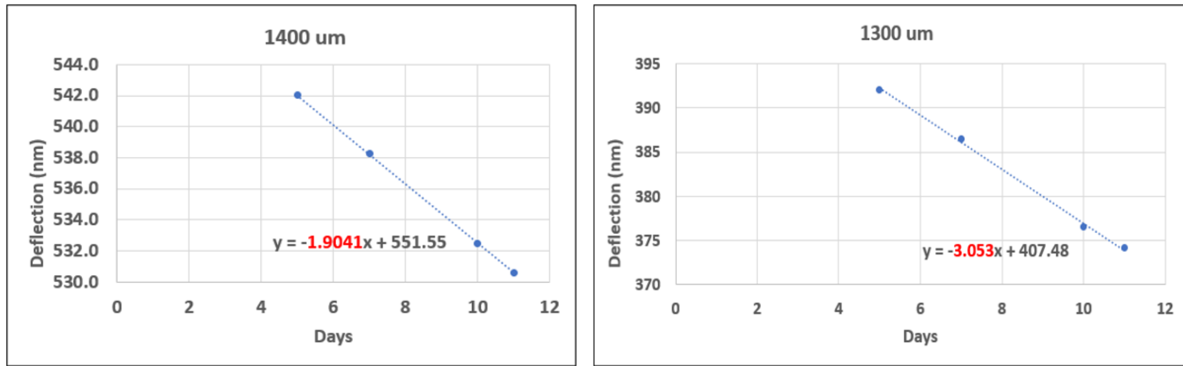

Figure 5.33: Linear fitting of deflection data points for 1400 μm and 1300 μm membrane

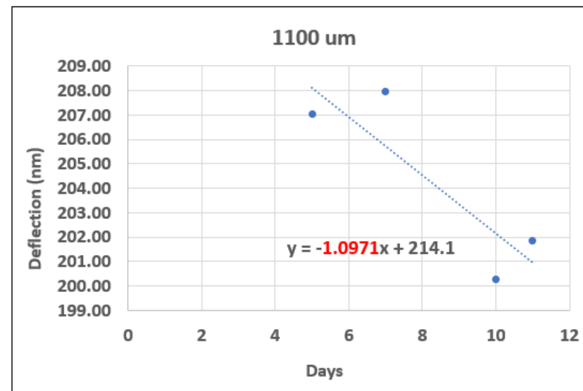

Figure 5.34: Linear fitting of deflection data points for 1100 μm membrane

Based on the obtained slopes, helium leak rates calculated for membranes along with the deflection rate are shown in the table.5.1. Along with this, we calculated the uncertainty involved in these measurements. For this, eq. 4.13 is used and for Δt we used 7 days, as only 7 days of measurement (Day-5 to Day-11) is used for calculating leak rates. Based on the uncertainty calculations, it was observed that even more no.of.days is required for small diameter membranes to have a lower order of error.

Table 5.1: Calculated helium leak rates for membranes and uncertainty involved in measuring leak rates

Diameters (μm)	Deflection rate (nm/day)	Leak rate (mol/sec)	Estimated uncertainty (mol/sec)
2000	8.46	1.36×10^{-17}	3.72×10^{-18}
1600	4.14	1.29×10^{-17}	7.43×10^{-18}
1400	1.90	8.23×10^{-18}	8.84×10^{-18}
1300	3.05	1.07×10^{-17}	10.48×10^{-18}
1100	1.09	6.62×10^{-18}	15.07×10^{-18}

5.4.3. Discussion

Based on the obtained leak rate values, it is thought whether the leakage has occurred through the membrane area (through silicon membrane) or along its circumference (through silicon oxide). Therefore the obtained values are plotted against diameter and diameter^2 and tried to provide a linear fitting to check. From the plotted graphs (Fig.5.35), it seems that the linear fitting line passes well through the 0-point for the graph showing leak rate vs diameter indicating that gas molecules could have entered through the oxide. However, due to a lack of data points, a firm judgment could not be made along which path the helium molecules have entered.

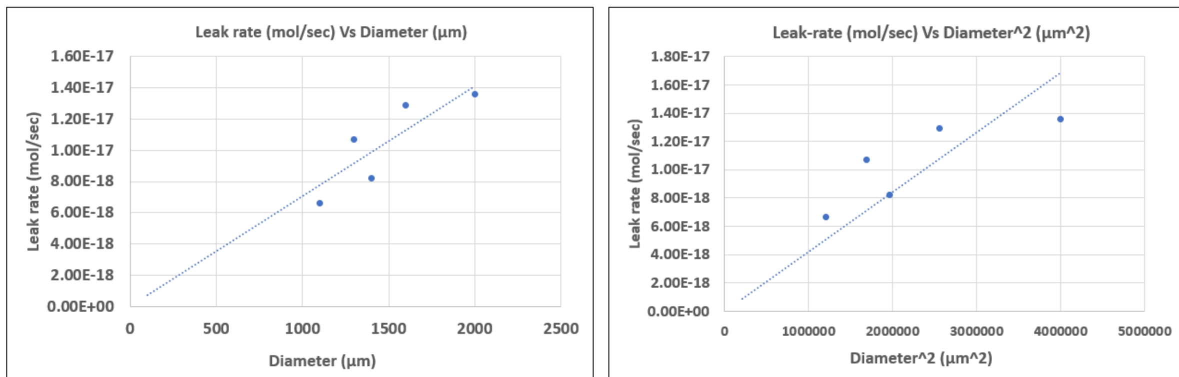

Figure 5.35: (A) Plot of leak rate against diameter (B) Plot of leak rate against diameter^2

To investigate further, an additional attempt was made to first check whether gas molecules entered through the silicon membrane area by considering the measurements made by Van Wieringen, A., and N. Warmoltz [64] for permeation of helium on silicon. Their corresponding test was conducted using a cylindrical wall (with an inner diameter of 1.80 and an outer diameter of 2.24cm) made of silicon. In their experiment, the cylindrical wall was exposed to helium from the outside, and the permeation of silicon was measured by a helium mass spectrometer from the inside. The permeation was measured in the units of molecules/cm.sec which represents the amount of gas in molecules per sec that passes through 1cm^2 of a flat wall of thickness 1cm with one atm pressure on the entrance side and vacuum on the other. Since the permeation was given in molecules/cm.sec, it was thought an analysis could be made by multiplying their permeation value obtained with our membrane area and by dividing by the thickness of our membrane so that this would give an idea of how much helium can penetrate into silicon. However, their measurements were made in the elevated temperature ranges of 967 ^{o}C and 1207 ^{o}C. Therefore, an insight could not be made on how much helium can penetrate into silicon at room temperature.

On the other side, an attempt was made to check whether gas molecules entered through the oxide based on the measurements made by Perkins, W. G., and D. R. Begeal. [9]. In this reference, the permeation values were provided for temperatures from 24 ^{o}C, however, their corresponding experiment was conducted in such a way that the silicon membrane of thickness 'L' is exposed to fixed helium pressure from the one side (i.e., from the side of -L/2) and the permeation of helium is measured from the opposite side (i.e., from the side of L/2). In our case, there is a chance of helium entering from any side of a given membrane in the die (this can be visualized based on the microscope image of the tested die shown in Fig.5.28). Therefore, in this case as well a proper judgment could not be made whether the gas molecules entered via the oxide. Hence, based on the considered literature resources and limited data points for leak rate a conclusion could not be attained along the path where the helium molecules could have entered into the cavities.

However, based on the test structures we designed for leak testing, we observed that the cavity design with a diameter of 2000 um membrane with a thickness of 40 um and with a gap height of 3.24 µm has the least uncertainty in measuring a leak rate of 1.93×10^{-12} mol/sec for one second time difference between two deflection measurements. This means that the minimum leak rate that can be detected by this cavity is 1.93×10^{-12} mol/sec. Having this cavity, it is thought how it can be used to measure leak rates as a *leak testing sensor* for MEMS packages fabricated on the same wafer. Here, it is assumed that the sensor experiences the same leakage as experienced by the MEMS packages. This is explained in the following cases:

Case 1: In the first case, a MEMS package having cavity dimensions equal to the *leak testing sensor* is considered. Therefore, the considered cavity volume is 0.01017 mm^3 (1.017×10^{-11} m^3). Let's assume that this MEMS package has a requirement to maintain 1 mbar of internal pressure for the duration of 10 years, with an acceptable increase in internal pressure of 10 % over its lifetime. Now, it is thought what is the leak rate requirement of this package? and how long do the deflection measurements need to be done with our *leak testing sensor* to measure this small leak rate?

- The 10 % increase in internal pressure corresponds to a 0.1 mbar change in pressure for the 10-year lifetime.

- Density of gas at 0.1 mbar = 0.00410 mol/m^3.
(This is calculated using the ideal gas law with P = 0.1 mbar and T=293.15 K).

- No.of.molecules required to increase 0.1 mbar pressure for the package volume of 1.017×10^{-11} m^3 = 4.16×10^{-14} mol. Therefore, for a 10-year (3.154×10^8 seconds) period the number of. molecules required to increase 0.1 mbar of internal pressure is equal to 4.16×10^{-14} mol.

- This gives the leak-rate requirement for the concerned package as (4.16×10^{-14} mol) / (3.154×10^8 seconds) = 1.31×10^{-22} mol./sec.

- Now, we know the minimum detectable leak rate for our leak testing device for 1 second which is 1.93×10^{-12} mol/sec. Therefore the time required to measure the leak rate of the MEMS package is (1.93×10^{-12}) / (1.31×10^{-22}) = 1.47×10^{10} seconds = 1.70×10^5 days. Measurement up to this much no.of.days would not be suitable to conduct this as an inline testing process.

All the above calculations are summarized in Table.5.2.

Table 5.2: Time required to measure leak rate of MEMS package with package volume of 0.01 mm^3, with the requirement of 0.1 mbar change over the lifetime of 10 years

Parmeters	Values	Units
Density of gas at 0.1 mbar	0.00410	mol/m^3
No.of.molecules to increase 0.1 mbar pressure for the package volume of 1.017×10^{-11} m^3	4.16×10^{-14}	mol.
Leak rate of concerned package for the 10 year period	1.31×10^{-22}	mol./sec.
Time required for leak rate measurement	1.70×10^5	days

Case 2: Instead of having a stringent requirement of 0.1 mbar in pressure change for the concerned package, it is thought how much will be the time required for our sensor to measure? if acceptable internal pressure change is 10 mbar for a 10-year duration for the above-mentioned package dimensions.

Table 5.3: Time required to measure leak rate of MEMS package with package volume of 0.01 mm^3, with the requirement of 10 mbar change over the lifetime of 10 years

Parmeters	Values	Units
Density of gas at 10 mbar	0.410	mol/m^3
No.of.molecules to increase 10 mbar pressure for the package volume of 1.017×10^{-11} m^3	4.167×10^{-12}	mol.
Leak rate of concerned package for the 10 year period	1.31×10^{-20}	mol./sec.
Time required for leak rate measurement	1.70×10^{3}	days

By relaxing the requirement to 10 mbar pressure change, the time required reduces by a factor of 100. But still, this value still remains high.

Case 3: In this case, instead of the volume of the package as 0.01 mm^3, the volume is now taken as 1 mm^3 with the same requirement of 10 mbar change in pressure. Again the same above calculation is repeated but with the new volume considered.

Table 5.4: Time required to measure leak rate of MEMS package with package volume of 1 mm^3, with the requirement of 10 mbar change over the lifetime of 10 years

Parmeters	Values	Units
Density of gas at 10 mbar	0.410	mol/m^3
No.of.molecules to increase 10 mbar pressure for the package volume of 1.0×10^{-9} m^3	4.10×10^{-10}	mol.
Leak rate of concerned package for the 10 year period	1.29×10^{-18}	mol./sec.
Time required for leak rate measurement	17	days

By increasing the volume of the package to 100 times larger, there is a significant reduction in the time requirement of measurement.

Case 4: As a last case, the volume is further increased to 2 mm^3. Here, again the time required for the sensor measurement is calculated with the same requirement of 10 mbar change for a 10-year duration time.

Table 5.5: Time required to measure leak rate of MEMS package with package volume of 2 mm^3, with the requirement of 10 mbar change over the lifetime of 10 years

Parmeters	Values	Units
Density of gas at 10 mbar	0.410	mol/m^3
No.of.molecules to increase 10 mbar pressure for the package volume of 2.0×10^{-9} m^3	8.2×10^{-10}	mol.
Leak rate of concerned package for the 10 year period	2.59×10^{-18}	mol./sec.
Time required for leak rate measurement	8	days

This many days of measurement can make it possible to conduct this test as an inline testing process.

Finally, this analysis demonstrates that by employing the selected "leak testing test structure," it could be possible to conduct lifetime testing within a minimal number of days for large-volume MEMS packages that have a tolerance of 10 mbar internal pressure change.

6 Conclusion

In this research, a method is developed to accurately measure the hermeticity of fusion-bonded silicon wafers, which can be used to test the bond quality of wafers as an inline testing process. The method involves fabricating a test structure between the bonded wafers such that one wafer contains a cavity and the other wafer contains a membrane, which deflects due to the pressure difference present between the outside and inside of the cavity. When leakage occurs between the bonded wafers, the pressure difference changes, and the deflection of the membrane changes. When this deflection is detectable, then by measuring those deflections, the leak rate can be quantified. The test structure can also be used for assessing the pressure after fabrication, but this thesis focuses only on determining the leak rates.

Test structure design:

To address the accurate measurement of leak rate, first, we designed test structures with the aim of measuring as small a leak rate as possible. The design process was explained in detail in section 3.1. Through this design analysis which focused on using the cavity volume effectively to measure small leak rates, we decided to use multiple test structures with circular membranes of thickness 40 µm, diameters of 2000, 1600, 1400, 1300, 1100, 900, 700, 500, and 300 µm and a cavity with a depth of 2.3 µm.

Measurement method, fabrication and uncertainty analysis:

The designed test structures were fabricated using the using the photolithography process. We fabricated two types of samples using the test structures, one with samples having nanometer gap size leak channels connected between the cavities and another with completely sealed-off cavities (section.4.6). Using the two types of samples, we decided to conduct three experiments: (1) Pressure-deflection characterization of membranes (2) Leak testing of samples with leak channels, and (3) Leak testing of samples with sealed-off cavities using Air and Helium gas. To conduct these experiments, an experimental setup (section.4.4) was developed that enables to change of external pressure inside a vacuum chamber that contains the test sample, and deflection measurements were captured using Lynceetec's DHM. The reason for choosing this equipment is that it has a long working distance (11.2 mm) due to which samples could be tested by keeping them in the vacuum chamber.

Before proceeding with the experiments, the samples were subjected to an error analysis where multiple measurements were made on fabricated samples to check their uncertainty in dimensions. Through these measurements, first, we observed that the attained cavity depth of samples was not 2.3 µm but it was 3.24 ± 0.06 µm (section.4.7.1). Then, based on membrane diameter and thickness measurements it was observed that all the attained diameters and thickness were up to the designed specification with an uncertainty of ± 2 µm and ± 0.05 µm respectively (Section.4.7.4 and.4.7.2). Then, using DHM we measured the deflection of samples for multiple days to determine the error in deflection measurement. Here, we found that there is an accuracy limit to the deflection measurement with the DHM of 10 nm (section.4.7.5). However, for cavities with membrane diameters of 500 and 300 µm, the accuracy limit was hard to detect because it was

not possible for DHM to measure very small changes in deflection for these small membranes.

Using the value of membrane diameters, thickness, and error in deflection measurements, we estimated the uncertainty in measuring leak rate for a 1-second time difference between two successive deflection measurements (section 4.8), which is the important step in this project work to understand the accuracy of leak testing measurements. The calculated values demonstrated that for a given time interval between the deflection measurements, the error in leak rate will be less for membranes with the largest diameter for a given thickness of the membrane and for a given gap height of the cavity. In our case, the least error is observed for 2000 um membrane of about 1.93×10^{-12} mol/sec for a 1-second time interval (section.4.8).

Experiments:

In the final stage, the test structures were first subjected to a pressure-deflection sensitivity characterization (section.5.1). Through this experiment, we were able to observe a good agreement between the experimental pressure-deflection value with the analytical values (Fig.5.6) which made sure that the designed membranes were functioning as per our design and led us to proceed for further experiments. During this experiment, we encountered that all the membranes had a residual deflection due to plastic deformation, which we then confirmed through a separate experiment where we punctured holes on samples with leak channels (section.5.2) and observed deflection of nearby cavities for multiple days. The plastic deformation observed from this experiment was not as we predicted from the design, but we suspect that this plastic deformation could be due to residual stress caused by the mismatch in thermal expansion coefficient between the silicon and oxide present in the fusion bonded wafers.

Before proceeding to the leak testing of samples with sealed-off cavities, to understand the process of leakage we first conducted the leak testing of samples with the leak channels (section.5.3). Through this experiment, the measured leak rates were compared with analytical values (Fig.5.25,5.25, 5.26 and 5.27) using models that describe the continuum, slip, and free-molecular flow of gas through the rectangular channels (eq.5.4,5.5 and 5.6). These expressions contained many parameters, out of which some are known which include gas properties, geometric quantities, and the accommodation coefficient. Besides, there were also three dimensionless parameters (ϵ, b_1, and b_0). In which, the value for b_1 was considered by accounting information from literature, and the value for ϵ was considered based on theoretical considerations. By adjusting the value of b_0, the experimental leak rates were observed to have good agreement with the values obtained using free-molecular flow models. Through this experiment, we were able to well-characterize the flow through leak channels using analytical models.

Finally, we conducted leak testing of samples with sealed-off cavities (section.5.4). Since the samples did not have any outgassing or air leakage, they were tested for leakage using helium gas under external pressure of 1000 mbar. Based on multiple days of deflection measurements, we could effectively measure the leak rate of the cavities (Fig.5.32,5.33 and 5.34). Based on the estimated uncertainty (Table.5.1), we observed that for larger samples (samples with diameter: 2000, 1600, 1400 µm) the measurements are done in such a way that the order of error achieved is comparable to the leak rates measured. However, for small samples (especially for 1100 µm having the same membrane thickness and same cavity depth) even more no.of.days is required to have reduced uncertainty.

On the basis of this experiment, it was not possible to draw a definitive conclusion regarding the path along which gas molecules entered to exhibit leakage. However, based on the test structure designs, an attempt was made to determine if the devised test method could be used as a leak testing sensor to measure leak rates for MEMS packages (section.5.4.3). For this purpose, we regarded the cavity design with the largest diameter of 2000um which had the lowest uncertainty in measuring leak rates to be the most appropriate sensor, assuming that the sensor experiences the same leakage as the MEMS package. Based on this analysis, it was inferred the proposed method could be beneficial for guaranteeing the lifetime of packages with significant volumes (exceeding 1 mm^3) that can tolerate internal pressure change of up to 10 mbar during their lifespan.

7
Recommendation

In this chapter we present some of the recommendations based on the work so far done for this project.

1. Improvements to detect even small leak rate:

In this thesis, we used the test structures designs by considering the membrane diameters and cavity depth corresponding to a membrane thickness of 40 µm, as it was convenient for us to fabricate this membrane thickness by just removing the handle and oxide layer of the SOI wafer. This limited our scope in estimating the smallest measurable leak rate. It was inferred that using the device design corresponding to 2000 µm with a cavity depth of 3.24 µm, the smallest possible measurable leak rate is approximately 2.59×10^{-18} mol/sec with minimal days of measurement to have comparable order of error, which is equivalent to 8 days (refer to Table.7.1). Therefore, it is thought whether it is possible to measure an even smaller leak rate by modifying the test structure dimensions. This is discussed in the following cases:

Case 1: The first consideration was to increase the membrane's diameter beyond 2000 µm while maintaining the same membrane thickness of 40 µm. For this the considered diameter: is 3000 µm and the expected leak rate to be measured is 1×10^{-20} mol/sec.

Table.7.1 demonstrates that increasing the diameter necessitates increasing the gap height, which has no effect on detecting the small leak rate within a minimal number of days of deflection measurement.

Table 7.1: Time required to measure the leak rate of 1×10^{-20} by considering device design with a membrane diameter of 3000 µm and a thickness of 40 µm.

Parmeters	Values	Units
Membrane diameter	3000	µm
Membrane Thickness	40	µm
Deflection at 1 atm	10.52	µm
Required minimum gap height	12	µm
Pressure-deflection sensitivity	10.52	nm/mbar
Minimum detectable leak rate for one second (using eq.4.13)	2.64×10^{-12}	mol/sec
Leak rate to be measured	1×10^{-20}	mol/sec
Time required for leak rate measurement	(2.64×10^{-12}) / (1×10^{-20}) = 3×10^{3}	days

Case 2: In this case, the same 3000 µm diameter is considered but now the thickness is reduced to 10 µm.

Table 7.2: Time required to measure the leak rate of 1×10^{-20} by considering device design with a membrane diameter of 3000 µm and a thickness of 10 µm

Parmeters	Values	Units
Membrane diameter	3000	µm
Membrane Thickness	10	µm
Deflection at 1 atm	673.73	µm
Required minimum gap height	675	µm
Pressure-deflection sensitivity	673.73	nm/mbar
Minimum detectable leak rate for one second	2.05×10^{-12}	mol/sec
Leak rate to be measured	1×10^{-20}	mol/sec
Time required for leak rate measurement	(2.05×10^{-12}) / (1×10^{-20}) = 2×10^{3}	days

The decrease in thickness for the larger diameter does not lead to a substantial improvement in the detection of small leak rates, since it results in an increased demand for gap height.

Case 3: Instead of having an increased diameter, in this case, the diameter is reduced to 1000 µm with the same thickness of 10 µm.

Table 7.3: Time required to measure the leak rate of 1×10^{-20} by considering device design with a membrane diameter of 1000 µm and a thickness of 10 µm

Parmeters	Values	Units
Membrane diameter	1000	µm
Membrane Thickness	10	µm
Deflection at 1 atm	8.3	µm
Required minimum gap height	9	µm
Pressure-deflection sensitivity	8.3	nm/mbar
Minimum detectable leak rate for one second	2.65×10^{-13}	mol/sec
Leak rate to be measured	1×10^{-20}	mol/sec
Time required for leak rate measurement	(2.65×10^{-13}) / (1×10^{-20}) = 307	days

When the diameter is reduced by a factor of 3 while maintaining the same thickness, there is a substantial decrease in the required gap height by a factor of 75. As a consequence, there has been a decrease in the amount of time needed to detect the anticipated leak rate.

Case 4: As a final case, the diameter is reduced by a factor of 10 to 100 µm, and the thickness is reduced by a factor of 10 to 1 µm.

Table 7.4: Time required to measure the leak rate of 1×10^{-20} by considering device design with a membrane diameter of 100 µm and a thickness of 1 µm

Parmeters	Values	Units
Membrane diameter	100	µm
Membrane Thickness	1	µm
Deflection at 1 atm	830	nm
Required minimum gap height	900	nm
Pressure-deflection sensitivity	0.83	nm/mbar
Minimum detectable leak rate for one second	2.65×10^{-15}	mol/sec
Leak rate to be measured	1×10^{-20}	mol/sec
Time required for leak rate measurement	(2.65×10^{-15}) / (1×10^{-20}) = 3	days

Finally, with the diameter and thickness reduced. The minimum gap height requirement is reduced even further. If the device design is feasible for fabrication, then it is possible to determine the leak rate of order 10^{-20} mol/sec with a minimal amount of days of deflection measurements.

2. Automated deflection measurements using DHM:

During the experiments with leak channels, we encountered that the rate of deflection reduction was so fast that it could not be easily measured by following the steps described in the section.4.2 every time. In such case, we explored an option in DHM - *sequence*, which is available under the *Mode* bar (Fig.4.4) of the main window of *Koala* software. Within the *sequence* menu, by selecting the 'acquisition' option, the hologram files can be recorded using the standard camera attached in DHM with a frame rate below 15 frames per second and can be saved along with the 'timestamp' by specifying the appropriate directory.

The saved hologram files can be retrieved and reconstructed to obtain intensity images, and wrapped or unwrapped phase images using *sequence-reconstruction-to-disk* option. This option is also available within the *sequence* menu. The reconstructed intensity and phase measurements will be based on current settings defined in *Koala*, i.e. it will be based on what option we set for laser wavelength and objective settings, digital tilt, and phase offset adjustment. Therefore, to obtain the correct measurements, ideal options need to be set before recording the hologram images. For the ideal options, section.4.2 can be referred to. Once the text files for unwrapped phase images are obtained, the directory containing all these files can used in MATLAB to obtain all the deflection values in one go. A source code sample is attached in part-B of Appendix.C.

3. Other possible PCM test structure:

To assess the applicability of our derived formula for the calculation of leak rates (eq.3.9) in this project, we used cavities with circular membranes that were fabricated using a special process flow (Section.4.6). However, in the early stages of the project, we tested some samples that were not accurately designed (as described in the section.3) and were prepared using an existing process flow (Fig.7.1). These are cavities containing rectangular membranes of varying dimensions (shown in mask layout Fig.7.2). FIB-SEM images of their cross-sections revealed that the membranes were not precisely flat but had extra material on the edges (Fig.7.3).

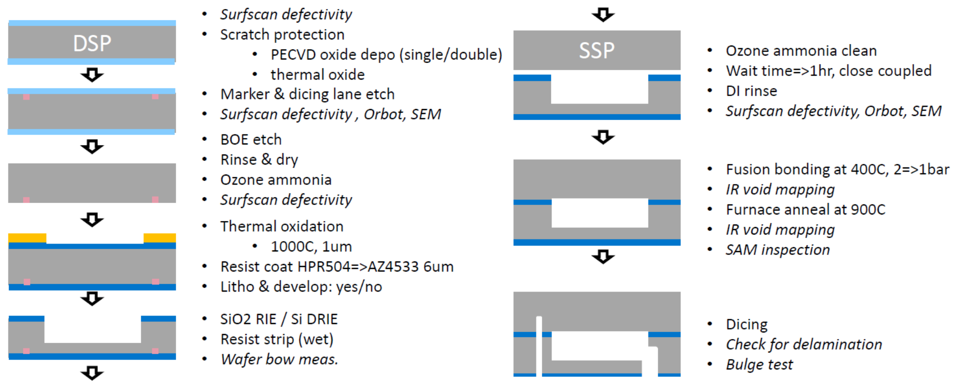

Figure 7.1: Existing process flow

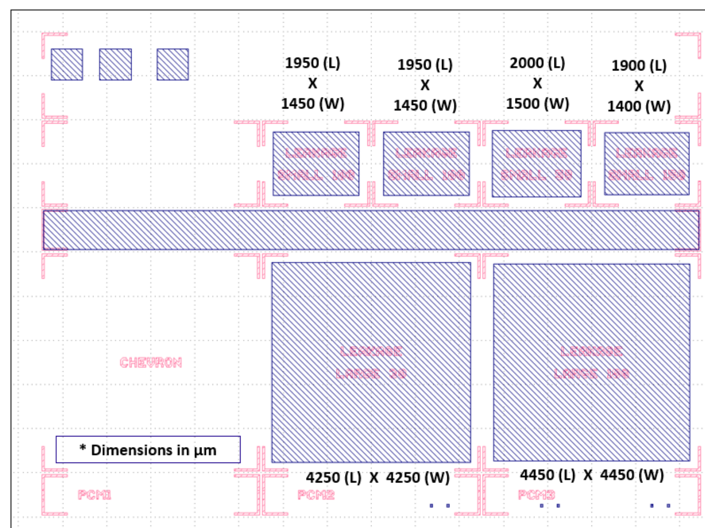

Figure 7.2: Mask layout of membranes fabricated using existing process flow

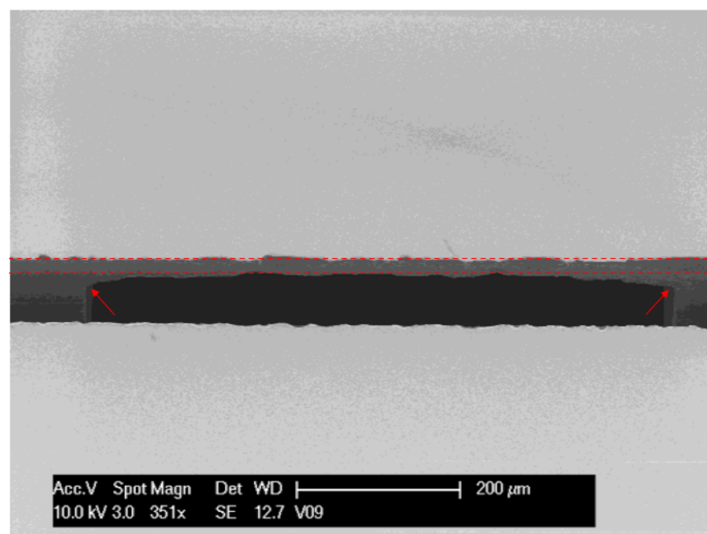

Figure 7.3: FIB-SEM image of membrane cross section

The pressure-deflection characterization test of corresponding samples showed that the deflection responses are linear with respect to changing external pressures along with the presence of residual deflection indicated by intercept in the fitting equation, as shown in Fig.7.4, Fig.7.5 and Fig.7.6. Due to the linear pressure-deflection response demonstrated by these test structures (which can be easily fabricated using the existing process flow), they can also serve as viable options for conducting leak testing. When these cavities exhibit leakage, the sensitivity values obtained from the characterization test may be substituted in equation 7.1 to calculate the leak rate. The only difficulty would be obtaining the correct value for effective volume; however, by substituting an approximate value, the order of leak rate that occurred could be understood.

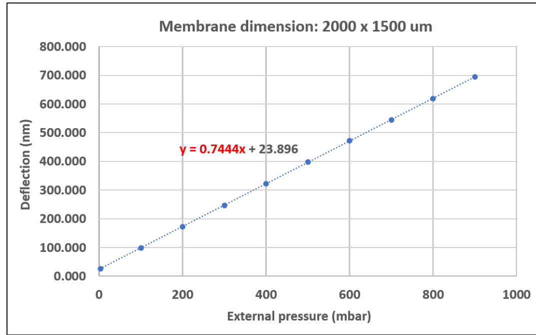

Figure 7.4: Pressure-deflection curve of the membrane having dimension of 2000 x 1500 (in um)

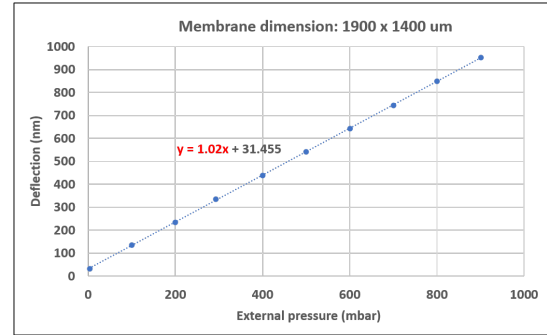

Figure 7.5: Pressure-deflection curve of the membrane having dimension of 1900 x 1400 (in um)

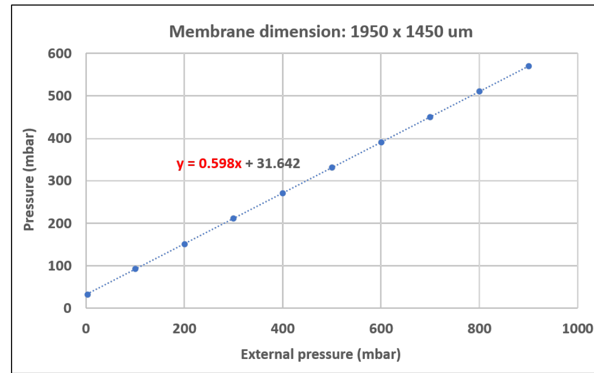

Figure 7.6: Pressure-deflection curve of the membrane having dimension of 1950 x 1450 (in um)

$$(-\frac{dZ}{dt}) = (\frac{dN_{in}}{dt})(\frac{RT}{V_{eff}}) \underbrace{(\frac{A}{K})}_{sensitivity} \tag{7.1}$$

References

[1] H. Greenhouse and O. E. P. HERMETICITY, *Noyes publications*, 2000.

[2] F. N. Sinnadurai, “Handbook of microelectronics packaging and interconnection technologies,” *(No Title)*, 1985.

[3] S. Costello *et al.*, “Towards new hermeticity test methods for mems,” Ph.D. dissertation, Heriot-Watt University, 2011.

[4] M. Esashi, “Wafer level packaging of mems,” *Journal of Micromechanics and Microengineering*, vol. 18, no. 7, p. 073 001, 2008.

[5] D. Li, X. Cui, M. Du, Y. Zhou, and F. Lan, “Effect of combined hydrophilic activation on interface characteristics of si/si wafer direct bonding,” *Processes*, vol. 9, no. 9, p. 1599, 2021.

[6] Q.-Y. Tong and U. Gösele, “Semiconductor wafer bonding: Recent developments,” *Materials Chemistry and physics*, vol. 37, no. 2, pp. 101–127, 1994.

[7] D. Kähler, F. Lofink, and W. Reinert, “Hermeticity tests,” in *Handbook of silicon based MEMS materials and technologies*, Elsevier, 2020, pp. 833–843.

[8] M. Knudsen, *The kinetic theory of gases: some modern aspects*. Methuen & Company Limited, 1934.

[9] W. Perkins and D. Begeal, “Diffusion and permeation of he, ne, ar, kr, and d2 through silicon oxide thin films,” *The Journal of Chemical Physics*, vol. 54, no. 4, pp. 1683–1694, 1971.

[10] F. J. Norton, “Helium diffusion through glass,” *Journal of the American Ceramic Society*, vol. 36, no. 3, pp. 90–96, 1953.

[11] L. C. Luther and W. J. Moore, “Diffusion of helium in silicon, germanium, and diamond,” *The Journal of Chemical Physics*, vol. 41, no. 4, pp. 1018–1026, 1964.

[12] S. Mack, H. Baumann, and U. Gösele, “Gas development at the interface of directly bonded silicon wafers: Investigation on silicon-based pressure sensors,” *Sensors and Actuators A: Physical*, vol. 56, no. 3, pp. 273–277, 1996.

[13] “Bond reliability testing for wafer-level packaged mems devices.” (2011), [Online]. Available: `https://www.memsjournal.com/2011/10/bonding-reliability-testing-for-wafer-level-packaged-mems-devices.html`.

[14] Q. Li, H. Goosen, F. V. Keulen, J. V. Beek, and G. Zhang, “Assessment of testing methodologies for thin-film vacuum mems packages,” vol. 15, Jan. 2009, pp. 161–168. DOI: `10.1007/s00542-008-0651-y`.

[15] S. Ruthberg, “Graphical solution for the back pressurization method of hermetic test,” *IEEE Transactions on Components, Hybrids, and Manufacturing Technology*, vol. 4, pp. 217–224, 2 1981, ISSN: 01486411. DOI: `10.1109/TCHMT.1981.1135792`.

[16] M. Nese, R. W. Bernstein, I.-R. Johansen, and R. Spooren, “New method for testing hermeticity of silicon sensor structures,” *Sensors and actuators A: physical*, vol. 53, no. 1-3, pp. 349–352, 1996.

[17] D. Lellouchi, J. Dhennin, X. Lafontan, D. Veyrie, J.-F. Le Neal, and F. Pressecq, “A new method for the hermeticity testing of wafer-level packaging,” *Journal of micromechanics and microengineering*, vol. 20, no. 2, p. 025 031, 2010.

[18] P. F. Bernath, *Spectra of atoms and molecules*. Oxford university press, 2020.

[19] N. Peica, “Vibrational spectroscopy and density functional theory calculations on biological molecules,” Ph.D. dissertation, Universität Würzburg, 2006.

[20] S. Karlen, J. Gobet, T. Overstolz, J. Haesler, and S. Lecomte, “Quantitative micro-raman spectroscopy for partial pressure measurement in small volumes,” *Applied Spectroscopy*, vol. 71, pp. 2707–2713, 12 Dec. 2017, ISSN: 19433530. DOI: `10.1177/0003702817724410`.

[21] F. Gueissaz, "Ultra low leak detection method for mems devices," in *18th IEEE International Conference on Micro Electro Mechanical Systems, 2005. MEMS 2005.*, IEEE, 2005, pp. 524–527.

[22] M. Lee, D. Davidovikj, B. Sajadi, *et al.*, "Sealing graphene nanodrums," *Nano letters*, vol. 19, no. 8, pp. 5313–5318, 2019.

[23] R. J. Dolleman, S. J. Cartamil-Bueno, H. S. van der Zant, and P. G. Steeneken, "Graphene gas osmometers," *2D Materials*, vol. 4, no. 1, p. 011 002, 2016.

[24] W. E. Newell, "Miniaturization of tuning forks: Integrated electronic circuits provide the incentive and the means for orders-of-magnitude reduction in size.," *Science*, vol. 161, no. 3848, pp. 1320–1326, 1968.

[25] J.-C. Souriau, L. Castagné, G. Parat, *et al.*, "Implantable device including a mems accelerometer and an asic chip encapsulated in a hermetic silicon box for measurement of cardiac physiological parameter," in *2014 IEEE 64th Electronic Components and Technology Conference (ECTC)*, IEEE, 2014, pp. 1198–1203.

[26] P. Van der Wel, J. Stulemeijer, J. Bielen, *et al.*, "Hermeticity testing of capacitive rf mems switches," in *2008 IEEE International Reliability Physics Symposium*, IEEE, 2008, pp. 691–692.

[27] G. Elger, L. Shiv, N. Nikac, F. Muller, R. Liebe, and M. Grigat, "Optical leak detection for wafer level hermeticity testing," in *IEEE/CPMT/SEMI 29th International Electronics Manufacturing Technology Symposium (IEEE Cat. No. 04CH37585)*, IEEE, 2004, pp. 326–331.

[28] F. Gueissaz, "Ultra low leak detection method for mems devices," 2005, pp. 524–527. DOI: `10.1109/memsys.2005.1453982`.

[29] D. Veyrie, D. Lellouchi, J. Roux, F. Pressecq, A. Tetelin, and C. Pellet, "Ftir spectroscopy for the hermeticity assessment of micro-cavities," *Microelectronics Reliability*, vol. 45, no. 9-11, pp. 1764–1769, 2005.

[30] F. Santagata, J. Creemer, E. Iervolino, and P. Sarro, "Tube-shaped pirani gauge for in situ hermeticity monitoring of sin thin-film encapsulation," *Journal of Micromechanics and Microengineering*, vol. 22, no. 10, p. 105 025, 2012.

[31] J. E. Zekry, D. S. Tezcan, V. Cherman, *et al.*, "Design, fabrication and testing of wafer-level thin film vacuum packages for mems based on nanoporous alumina membranes," *Sensors and Actuators A: Physical*, vol. 189, pp. 218–232, 2013.

[32] D. Stroehle, "On the penetration of gases and water vapour into packages with cavities and on maximum allowable leak rates.," IEEE, 1977, pp. 101–106. DOI: `10.1109/irps.1977.362778`.

[33] S. P. Koenig, L. Wang, J. Pellegrino, and J. S. Bunch, "Selective molecular sieving through porous graphene," *Nature nanotechnology*, vol. 7, no. 11, pp. 728–732, 2012.

[34] S. Timoshenko, S. Woinowsky-Krieger, *et al.*, *Theory of plates and shells*. McGraw-hill New York, 1959, vol. 2.

[35] C. Young Warren and G. Budynas Richard, "Roark's formulas for stress and strain," *McGraw Hill Company*, 1989.

[36] K. Yasutake, J. Murakami, M. Umeno, and H. Kawabe, "Mechanical properties of heat-treated cz–si wafers from brittle to ductile temperature range," *Japanese Journal of Applied Physics*, vol. 21, no. 5A, p. L288, 1982.

[37] J. Ren, M. Ward, P. Kinnell, R. Craddock, and X. Wei, "Plastic deformation of micromachined silicon diaphragms with a sealed cavity at high temperatures," *Sensors*, vol. 16, no. 2, p. 204, 2016.

[38] J. Vanhellemont, A. K. Swarnakar, and O. Van der Biest, "Temperature dependent young's modulus of si and ge," *ECS Transactions*, vol. 64, no. 11, p. 283, 2014.

[39] J. Patel and A. Chaudhuri, "Macroscopic plastic properties of dislocation-free germanium and other semiconductor crystals. i. yield behavior," *Journal of Applied Physics*, vol. 34, no. 9, pp. 2788–2799, 1963.

[40] F. Charrière, J. Kühn, T. Colomb, *et al.*, "Characterization of microlenses by digital holographic microscopy," *Applied Optics*, vol. 45, no. 5, pp. 829–835, 2006.

[41] B. Kemper and G. Von Bally, "Digital holographic microscopy for live cell applications and technical inspection," *Applied optics*, vol. 47, no. 4, A52–A61, 2008.

[42] S. De Nicola, P. Ferraro, A. Finizio, *et al.*, "Surface topography of microstructures in lithium niobate by digital holographic microscopy," *Measurement Science and Technology*, vol. 15, no. 5, p. 961, 2004.

[43] F. Dubois, N. Callens, C. Yourassowsky, M. Hoyos, P. Kurowski, and O. Monnom, "Digital holographic microscopy with reduced spatial coherence for three-dimensional particle flow analysis," *Applied optics*, vol. 45, no. 5, pp. 864–871, 2006.

[44] N. Verrier, C. Fournier, and T. Fournel, "3d tracking the brownian motion of colloidal particles using digital holographic microscopy and joint reconstruction," *Applied optics*, vol. 54, no. 16, pp. 4996–5002, 2015.

[45] P. Langehanenberg, L. Ivanova, I. Bernhardt, *et al.*, "Automated three-dimensional tracking of living cells by digital holographic microscopy," *Journal of biomedical optics*, vol. 14, no. 1, pp. 014 018–014 018, 2009.

[46] B. Rappaz, E. Cano, T. Colomb, *et al.*, "Noninvasive characterization of the fission yeast cell cycle by monitoring dry mass with digital holographic microscopy," *Journal of biomedical optics*, vol. 14, no. 3, pp. 034 049–034 049, 2009.

[47] T. Colomb, E. Cuche, F. Charrière, *et al.*, "Automatic procedure for aberration compensation in digital holographic microscopy and applications to specimen shape compensation," *Applied optics*, vol. 45, no. 5, pp. 851–863, 2006.

[48] Author(s), *Title of the web page*, 2023. [Online]. Available: `https://www.lynceetec.com/reflection-dhm/#tab-2`.

[49] E. Cuche, P. Marquet, and C. Depeursinge, "Simultaneous amplitude-contrast and quantitative phase-contrast microscopy by numerical reconstruction of fresnel off-axis holograms," *Applied optics*, vol. 38, no. 34, pp. 6994–7001, 1999.

[50] T. Colomb, J. Kühn, F. Charrière, C. Depeursinge, P. Marquet, and N. Aspert, "Total aberrations compensation in digital holographic microscopy with a reference conjugated hologram," *Optics express*, vol. 14, no. 10, pp. 4300–4306, 2006.

[51] A. S. Brand, "Phase uncertainty in digital holographic microscopy measurements in the presence of solution flow conditions," *Journal of Research of the National Institute of Standards and Technology*, vol. 122, p. 1, 2017.

[52] Author(s), *Title of the web page*, 2023. [Online]. Available: `https://www.lynceetec.com/phase-microscopy/#tab-2`.

[53] X. Lai, H. Lin, Q. Chen, Y. Ge, C. Su, and K. Wei, "Performance of the 1d standard polynomials fitting method for total phase aberration compensation in digital holographic microscopy," *Optik*, vol. 223, p. 165 586, 2020.

[54] M. A. Schofield and Y. Zhu, "Fast phase unwrapping algorithm for interferometric applications," *Optics letters*, vol. 28, no. 14, pp. 1194–1196, 2003.

[55] L. L. Garcı a, A. G. Arellano, and W. Cruz-Santos, "A parallel path-following phase unwrapping algorithm based on a top-down breadth-first search approach," *Optics and Lasers in Engineering*, vol. 124, p. 105 827, 2020.

[56] M. Gallis and J. Torczynski, "Direct simulation monte carlo-based expressions for the gas mass flow rate and pressure profile in a microscale tube," *Physics of Fluids*, vol. 24, no. 1, 2012.

[57] E. H. Kennard *et al.*, *Kinetic theory of gases*. McGraw-hill New York, 1938, vol. 483.

[58] A. Agrawal and S. Prabhu, "Survey on measurement of tangential momentum accommodation coefficient," *Journal of Vacuum Science & Technology A*, vol. 26, no. 4, pp. 634–645, 2008.

[59] M. A. Gallis, J. Torczynski, and D. Rader, "A computational investigation of noncontinuum gas-phase heat transfer between a heated microbeam and the adjacent ambient substrate," *Sensors and Actuators A: Physical*, vol. 134, no. 1, pp. 57–68, 2007.

[60] J. R. Torczynski and M. A. Gallis, "Dsmc-based shear-stress/velocity-slip boundary condition for navier-stokes couette-flow simulations," in *AIP Conference Proceedings*, American Institute of Physics, vol. 1333, 2011, pp. 802–807.

[61] J. M. Anderson, M. W. Moorman, J. R. Brown, *et al.*, "Isothermal mass flow measurements in microfabricated rectangular channels over a very wide knudsen range," *Journal of Micromechanics and Microengineering*, vol. 24, no. 5, p. 055 013, 2014.

[62] M. v. Smoluchowski, "On the kinetic theory of transpiration and diffusion of diluted gases," *Annals of Physics*, vol. 338, no. 16, pp. 1559–1570, 1910.

[63] P. Clausing, "The flow of highly rarefied gases through tubes of arbitrary length," *Journal of Vacuum Science and Technology*, vol. 8, no. 5, pp. 636–646, 1971.

[64] A. Van Wieringen and N. Warmoltz, "On the permeation of hydrogen and helium in single crystal silicon and germanium at elevated temperatures," *physica*, vol. 22, no. 6-12, pp. 849–865, 1956.

A

Uncertainty in measured diameters of membranes

Table A.1: Uncertainty in measured diameters

Sample	2000 µm	1600µm	1400µm	1300µm	1100µm	900µm
1	2001.667	1602.09	1403.253	1301.921	1101.568	901.552
2	1999.308	1599.851	1402.818	1300.218	1104.011	904.015
3	2004.24	1603.835	1402.794	1297.193	1101.338	899.314
4	2000.456	1604.555	1401.183	1304.246	1100.674	902.842
5	2002.971	1599.118	1403.999	1303.274	1100.957	900.273
6	2003.608	1600.514	1401.481	1299.334	1102.886	899.263
7	1999.36	1601.997	1398.984	1305.051	1105.502	901.693
8	2002.793	1598.257	1402.759	1305.977	1099.628	898.257
9	2003.905	1600.822	1400.614	1301.93	1097.092	903.62
10	2000.412	1600.439	1399.334	1305.142	1101.667	902.37
Standard deviation (µm)	**1.79**	**1.89**	**1.60**	**2.71**	**2.20**	**1.87**

B

Pressure-deflection measurements for random error estimation

Table B.1: Pressure-deflection measurements obtained from day-1 to day-8 for membrane diameter: **2000 μm**

External Pressure (mbar)	Deflection (nm) Day-1	Deflection (nm) Day-3	Deflection (nm) Day-5	Deflection (nm) Day-8	**Standard deviation (nm)**
1000.500	2072.00	2074.30	2066.00	2070.40	3.50
900.250	1861.50	1862.90	1855.60	1859.80	3.16
799.875	1648.20	1654.16	1645.10	1647.70	3.83
700.025	1436.50	1440.63	1433.10	1436.30	3.09
600.600	1225.40	1225.70	1222.60	1225.90	1.55
500.575	1012.50	1011.90	1009.60	1010.70	1.29
400.525	799.62	813.07	797.24	799.30	**7.25**
300.525	586.96	586.23	585.32	587.31	0.88
200.475	373.28	372.65	372.29	373.88	0.70
100.575	161.93	160.19	160.70	162.63	1.12

Table B.2: Pressure-deflection measurements obtained from day-1 to day-8 for membrane **diameter: 1600 μm**

External Pressure (mbar)	Deflection (nm) Day-1	Deflection (nm) Day-3	Deflection (nm) Day-5	Deflection (nm) Day-8	**Standard deviation (nm)**
1000.500	882.73	892.06	882.47	891.36	6.11
900.250	798.26	802.44	802.83	807.27	3.68
799.875	708.49	712.60	712.83	716.20	3.16
700.025	613.66	622.65	622.96	625.95	5.31
600.600	523.51	533.03	533.65	537.35	5.90
500.575	438.21	442.35	443.05	447.92	3.98
400.525	348.34	352.09	352.90	357.57	3.79
300.525	252.97	262.00	262.90	266.33	5.70
200.475	167.43	171.77	173.00	176.06	3.58
100.575	77.22	81.42	82.92	86.27	3.76

Table B.3: Pressure-deflection measurements obtained from day-1 to day-8 for membrane **diameter: 1400 μm**

External Pressure (mbar)	Deflection (nm) Day-1	Deflection (nm) Day-3	Deflection (nm) Day-5	Deflection (nm) Day-8	**Standard deviation (nm)**
1000.500	539.13	539.929	539.17	542.64	1.66
900.250	485.74	485.955	485.92	489.33	1.73
799.875	432.06	432.418	432.14	435.45	1.63
700.025	378.09	378.967	378.21	381.80	1.73
600.600	324.46	325.190	324.42	328.11	1.75
500.575	270.41	271.074	270.44	273.84	1.63
400.525	216.72	216.76	217.03	219.91	1.54
300.525	162.97	162.57	163.35	166.21	1.66
200.475	109.05	109.35	109.57	112.66	1.68
100.575	56.30	55.72	57.47	59.30	1.58

Table B.4: Pressure-deflection measurements obtained from day-1 to day-8 for membrane **diameter: 1300 μm**

External Pressure (mbar)	Deflection (nm) Day-1	Deflection (nm) Day-3	Deflection (nm) Day-5	Deflection (nm) Day-8	**Standard deviation (nm)**
1000.500	399.79	402.38	400.94	402.78	1.37
900.250	359.96	361.81	360.47	361.93	0.98
799.875	319.32	320.95	319.92	321.28	0.91
700.025	282.49	280.30	279.24	281.12	1.37
600.600	238.19	239.74	238.64	241.01	1.26
500.575	197.45	198.75	197.76	200.64	1.44
400.525	163.12	157.84	157.13	160.08	2.70
300.525	115.91	117.28	116.48	119.16	1.41
200.475	75.20	77.15	76.08	78.27	1.33
100.575	41.31	42.38	37.67	39.35	2.09

Table B.5: Pressure-deflection measurements obtained from day-1 to day-8 for membrane **diameter: 1100 μm**

External Pressure (mbar)	Deflection (nm) Day-1	Deflection (nm) Day-3	Deflection (nm) Day-5	Deflection (nm) Day-8	**Standard deviation (nm)**
1000.500	208.50	210.80	207.80	215.34	3.41
900.250	187.41	189.37	186.61	193.88	3.26
799.875	166.10	167.92	165.45	172.65	3.26
700.025	144.91	146.84	144.33	151.50	3.25
600.600	123.71	125.68	123.17	130.23	3.21
500.575	102.39	104.16	102.09	108.73	3.07
400.525	81.12	82.99	80.88	87.43	3.03
300.525	59.74	61.62	59.57	66.06	3.02
200.475	38.33	40.06	38.26	44.60	2.97
100.575	16.93	20.43	17.16	23.08	2.93

C

Source code for actual deflection calculation

```
1
2 %% Set up the import Options - Here lines 4 to 23 can be set using the import options tool in
      MATLAB. Set the "column delimiters" as specified in line 10 and select the unwrapped
     data values by providing the range of columns and rows in "Range".
3
4 clear;
5 clf;
6 opts = delimitedTextImportOptions("NumVariables", 801);
7
8 % Specify range and delimiter
9
10 opts.Delimiter = ["\t", " ", ",", ";"];
11
12 % Specify column names and types
13 opts.VariableNames = [];
14 opts.VariableTypes = [];
15
16 % Specify file-level properties
17 opts.ExtraColumnsRule = "ignore";
18 opts.EmptyLineRule = "read";
19
20 % Specify variable properties
21 opts = setvaropts(opts, "VarName801", "WhitespaceRule", "preserve");
22 opts = setvaropts(opts, "VarName801", "EmptyFieldRule", "auto");
23 opts.DataLines = [5, Inf];
24
25 % Import the data
26
27 Phaseunwrap = readtable("%%%%", opts);
28 (% - Specify the file location where the unwrapped data file is present)
29
30 data= double(table2array(Phaseunwrap));
31 size=800;
32 dataclean = data(1:size,1:size); (% Size refers to no.of.rows and columns in which the
     unwrapped data is present)
33
34 % Optionally import the header lines with parameters that contain the conversion factor.
35 opts = delimitedTextImportOptions("NumVariables", 5);
36 opts.DataLines = [1, 4];
37
38 pixelsize = 2.43322e-06;
39 conversionfact=5.29981e-08;
40 (% pixelsize and conversionfact values are present in default in the unwrapped text file)
41
42 dataclean = dataclean*conversionfact;
43 heightdiff = (max(max(dataclean))-min(min(dataclean)))/1e-9
44
```

```
45 x = linspace(-0.5*size*pixelsize,0.5*size*pixelsize,size);
46 y = linspace(-0.5*size*pixelsize,0.5*size*pixelsize,size);
47 [X,Y] = meshgrid(x,y);
48 
49 %contourf(X,Y,dataclean)
50 
51 figure(1)
52 colormap(jet(256))
53 surf(X.*(1e6),Y.*(1e6),dataclean*(1e9),'FaceColor','interp','EdgeColor','none')
54 
55 % Fit a quadratic polynomial to the lowest area where the maximum deflection is present
56 
57 fitxmin=(size/2)-50;
58 fitxmax=(size/2)+50;
59 fitymin=(size/2)-50;
60 fitymax=(size/2)+50;
61 [X,Y] = meshgrid(x(fitxmin:fitxmax),y(fitymin:fitymax));
62 zfit=dataclean(fitxmin:fitxmax, fitymin:fitymax);
63 Zdata=zfit(:);
64 fitsurface=fit([X(:) Y(:)], Zdata,'poly22');
65 
66 p00=fitsurface.p00;
67 p10=fitsurface.p10;
68 p20=fitsurface.p20;
69 p11=fitsurface.p11;
70 p01=fitsurface.p01;
71 p02=fitsurface.p02;
72 
73 figure(3) % - Plot of ROI containing the deflected surface with the fitted surface
74 
75 plot(fitsurface,[X(:) Y(:)],Zdata)
76 hold on
77 
78 % %find the minimum dZ/dx=0 and dZ/dy=0, where Z is the fitting polynomial equation = Z =p00
    + p01 x+ p10 y+ p20 x^2 + p02 y^2 + p11 xy
79 
80 xmin=(2*p02*p10-p01*p11)/(p11^2-4*p02*p20);
81 ymin=(-p10*p11+2*p01*p20)/(p11^2-4*p02*p20);
82 zmin=fitsurface(xmin,ymin);  (%- This provide the maximum value of deflection)
83 
84 % Fit the 4 corners for the correction of flatness
85 
86 fitminc=1;
87 fitmaxc=10;
88 
89 [X1,Y1] = meshgrid(x(fitminc:fitmaxc),y(fitminc:fitmaxc));
90 zfit1=dataclean(fitminc:fitmaxc, fitminc:fitmaxc);
91 [X2,Y2] = meshgrid(x(size-fitmaxc:size-fitminc),y(fitminc:fitmaxc));
92 zfit2=dataclean(size-fitmaxc:size-fitminc, fitminc:fitmaxc);
93 [X3,Y3] = meshgrid(x(fitminc:fitmaxc),y(size-fitmaxc:size-fitminc));
94 zfit3=dataclean(fitminc:fitmaxc, size-fitmaxc:size-fitminc);
95 [X4,Y4] = meshgrid(x(size-fitmaxc:size-fitminc),y(size-fitmaxc:size-fitminc));
96 zfit4=dataclean(size-fitmaxc:size-fitminc, size-fitmaxc:size-fitminc);
97 
98 Xc = [X1 X2;X3 X4];
99 Yc = [Y1 Y2;Y3 Y4];
100 zfitc = [zfit1 zfit3;zfit2 zfit4];
101 
102 figure(5)  % - Plot of ROI containing the tilted surface with the fitted surface
103 plot(fitsurfacec,[Xc(:) Yc(:)],zfitc(:))
104 
105 flat=fitsurfacec(xmin,ymin);  % - This is gives the value of minimum deflection value at the
    x and y coordinates where the maximum deflection is present
106 
107 deflection1=(zmin-flat)*(1e9)  % Final calculation of deflection in nm
108 
109 % actual deflection - Since in our case oxide is present on top of the membrane, every time
    oxide thickness needs to be subtracted from the final deflection to obtain the actual
    deflection.
110 
111 oxide thickness = 142;          % substitute the oxide thickness here
```

```
112
113 deflection2=abs(deflection1)- oxide thickness; % - This gives the actual deflection value
```

A. Oxide thickness measurement:

Oxide thickness is measured at 2 points as shown below in two images (Fig.C.1 and .C.2). These values are then averaged to obtain the mean oxide thickness.

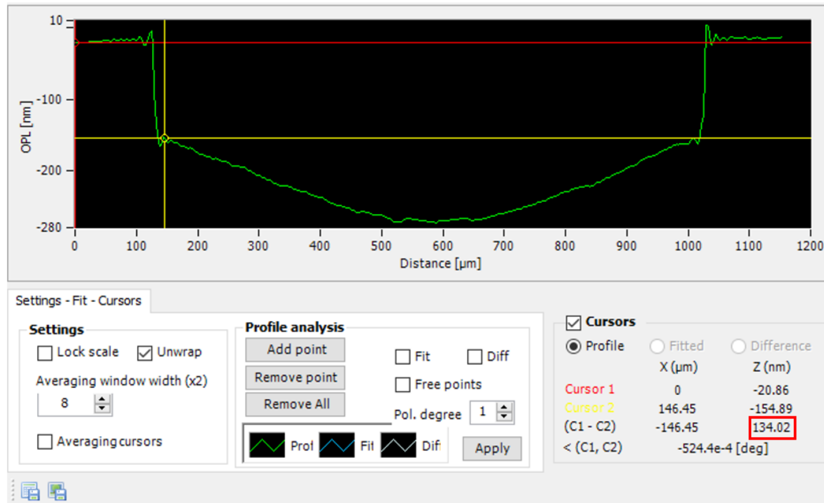

Figure C.1: Oxide thickness at point-1

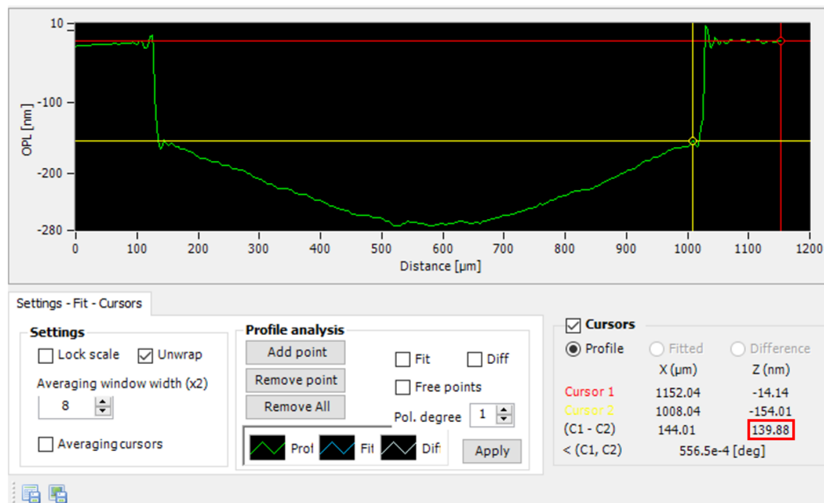

Figure C.2: Oxide thickness at point-2

B. Source code for deflection calculation based on unwrapped phase obtained using mode-sequence option:

```
% specify the folder path as in your case

folder='D:\Experiments\Isolated pressure sensors\Leak channel Study\Wafer 850 new\Die-1\
    Vacuum\2000\2023.06.23 13-53-47\Phase\Float\Txt\';

 % Get a list of all text files in the folder

files = dir(fullfile(folder, '*.txt'));

for i = 1:length(files)

file = files(i);
filename = fullfile(folder, file.name);

%% Set up the import Options - Here lines 4 to 23 can be set using the import options tool in
     MATLAB. Set the "column delimiters" as specified in line 10 and select the unwrapped
    data values by providing the range of columns and rows in "Range".

clear;
clf;
opts = delimitedTextImportOptions("NumVariables", 801);

% Specify range and delimiter

opts.Delimiter = ["\t", " ", ",", ";"];

% Specify column names and types
opts.VariableNames = [];
opts.VariableTypes = [];

% Specify file-level properties
opts.ExtraColumnsRule = "ignore";
opts.EmptyLineRule = "read";

% Specify variable properties
opts = setvaropts(opts, "VarName801", "WhitespaceRule", "preserve");
opts = setvaropts(opts, "VarName801", "EmptyFieldRule", "auto");
opts.DataLines = [5, Inf];

% Import the data

Phaseunwrap = readtable("%%%%", opts);
(% - Specify the file location where the unwrapped data file is present)

data= double(table2array(Phaseunwrap));
size=800;
dataclean = data(1:size,1:size); (% Size refers to no.of.rows and columns in which the
    unwrapped data is present)

% Optionally import the header lines with parameters that contain the conversion factor.
opts = delimitedTextImportOptions("NumVariables", 5);
opts.DataLines = [1, 4];

pixelsize = 2.43322e-06;
conversionfact=5.29981e-08;
(% pixelsize and conversionfact values are present in default in the unwrapped text file)

dataclean = dataclean*conversionfact;
heightdiff = (max(max(dataclean))-min(min(dataclean)))/1e-9

x = linspace(-0.5*size*pixelsize,0.5*size*pixelsize,size);
y = linspace(-0.5*size*pixelsize,0.5*size*pixelsize,size);
[X,Y] = meshgrid(x,y);

%contourf(X,Y,dataclean)

```

```
64 figure(1)
65 colormap(jet(256))
66 surf(X.*(1e6),Y.*(1e6),dataclean*(1e9),'FaceColor','interp','EdgeColor','none')
67
68 % Fit a quadratic polynomial to the lowest area where the maximum deflection is present
69
70 fitxmin=(size/2)-50;
71 fitxmax=(size/2)+50;
72 fitymin=(size/2)-50;
73 fitymax=(size/2)+50;
74 [X,Y] = meshgrid(x(fitxmin:fitxmax),y(fitymin:fitymax));
75 zfit=dataclean(fitxmin:fitxmax, fitymin:fitymax);
76 Zdata=zfit(:);
77 fitsurface=fit([X(:) Y(:)], Zdata,'poly22');
78
79 p00=fitsurface.p00;
80 p10=fitsurface.p10;
81 p20=fitsurface.p20;
82 p11=fitsurface.p11;
83 p01=fitsurface.p01;
84 p02=fitsurface.p02;
85
86 figure(3) % - Plot of ROI containing the deflected surface with the fitted surface
87
88 plot(fitsurface,[X(:) Y(:)],Zdata)
89 hold on
90
91 % %find the minimum dZ/dx=0 and dZ/dy=0, where Z is the fitting polynomial equation = Z =p00
       + p01 x+ p10 y+ p20 x^2 + p02 y^2 + p11 xy
92
93 xmin=(2*p02*p10-p01*p11)/(p11^2-4*p02*p20);
94 ymin=(-p10*p11+2*p01*p20)/(p11^2-4*p02*p20);
95 zmin=fitsurface(xmin,ymin);  (%- This provide the maximum value of deflection)
96
97 % Fit the 4 corners for the correction of flatness
98
99 fitminc=1;
100 fitmaxc=10;
101
102 [X1,Y1] = meshgrid(x(fitminc:fitmaxc),y(fitminc:fitmaxc));
103 zfit1=dataclean(fitminc:fitmaxc, fitminc:fitmaxc);
104 [X2,Y2] = meshgrid(x(size-fitmaxc:size-fitminc),y(fitminc:fitmaxc));
105 zfit2=dataclean(size-fitmaxc:size-fitminc, fitminc:fitmaxc);
106 [X3,Y3] = meshgrid(x(fitminc:fitmaxc),y(size-fitmaxc:size-fitminc));
107 zfit3=dataclean(fitminc:fitmaxc, size-fitmaxc:size-fitminc);
108 [X4,Y4] = meshgrid(x(size-fitmaxc:size-fitminc),y(size-fitmaxc:size-fitminc));
109 zfit4=dataclean(size-fitmaxc:size-fitminc, size-fitmaxc:size-fitminc);
110
111 Xc = [X1 X2;X3 X4];
112 Yc = [Y1 Y2;Y3 Y4];
113 zfitc = [zfit1 zfit3;zfit2 zfit4];
114
115 figure(5)  % - Plot of ROI containing the tilted surface with the fitted surface
116 plot(fitsurfacec,[Xc(:) Yc(:)],zfitc(:))
117
118 flat=fitsurfacec(xmin,ymin);  % - This is gives the value of minimum deflection value at the
       x and y coordinates where the maximum deflection is present
119
120 deflection1=(zmin-flat)*(1e9)  % Final calculation of deflection in nm
121
122 % actual deflection - Since in our case oxide is present on top of the membrane, every time
       oxide thickness needs to be subtracted from the final deflection to obtain the actual
       deflection.
123
124 oxide thickness = 142;          % substitute the oxide thickness here
125
126 deflection2=abs(deflection1)- oxide thickness; % - This gives the actual deflection value
127
128 % Store the output value of actual deflection
129 outputValues(i) = deflection2;
130 end
```

D

Reliability checking of pressure controller and readout

Before conducting the pressure-deflection experiment, first the reliability of the pressure controller was inspected. The pressure regulator used for this experiment works based on closed-loop control. Pressure is controlled by the use of two solenoid valves. One valve functions as the inlet control (here it is the vacuum line) and the other as the exhaust (gas supply line). The inlet valve operates proportionally to the input voltage supplied via the control circuit from the power supply. The exhaust solenoid is a standard ON/OFF solenoid and allows excess gas to be vented from the system. The pressure output is measured by an internal pressure transducer and provides a feedback signal to the PID control circuit. This feedback signal is compared with the command signal input. A difference between the two signals causes one of the valves to open, allowing flow in or out of the system. Low pressure allows the valve for the vacuum line to open and high pressure allows the valve for the gas supply line to open. Finally, the output pressure is displayed in the form of digital output voltage on the pressure readout unit. The formula to convert the output voltage to pressure is as follows:

$$Output\ pressure = Pressure\ range \quad \frac{V_{out} - V(lowerlimit)}{V(upperlimit) - V(lowerlimit)} \tag{D.1}$$

Where output pressure corresponds to the pressure inside the chamber (in mbar) and the pressure range is 1000 mbar. For 1000 mbar, V (upper limit) is 10 V and for 0 mbar, the V (lower limit) is 0 V, hence V (upper limit)-V (lower limit)=10 V. Therefore, the equation can be represented as follows:

$$Output\ pressure \quad (mbar) = 1000mbar \ \ (\frac{V_{out}}{10V}) \tag{D.2}$$

The accuracy of the pressure controller is checked by connecting the other end of the vacuum chamber with the manometer (Fig.D.1).

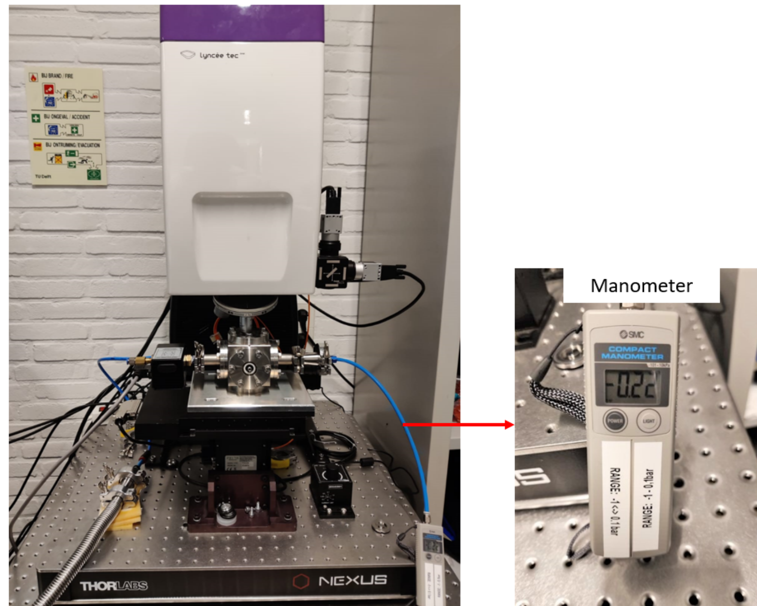

Figure D.1: Experimental setup attached with manometer for testing the accuracy of pressure controller

Table.D.1 shows the comparison of readout from the pressure regulator unit and manometer for input voltages varying from 9 to 1 V. Manometer provides its readout in the form of differential pressure: ΔP = P(inside the chamber)-P(outside the chamber). To obtain the atmospheric pressure, a voltage readout was recorded without setting any input voltage. At 0 manometer reading, the recorded voltage readout was 10.324 V which corresponds to 1.0324 bar. This value was used for P(outside the chamber) to calculate P(inside the chamber) measured by the manometer. By varying pressure levels, it could be observed that output pressures accurately match with the manometer readings up to the first two decimal points. This made sure that the pressure controller is reliable for the planned experiments.

Table D.1: Comparison of readout from pressure regulator and manometer

Input voltage (V)	Input pressure (bar)	Voltage readout (V)	**Pressure readout (bar)**	Manometer readout (bar)	**Output pressure from manometer (bar)**
9	0.9	9.009	**0.9009**	-0.13	**0.90**
8	0.8	8.009	**0.8009**	-0.23	**0.80**
7	0.7	7.010	**0.7010**	-0.33	**0.70**
6	0.6	6.013	**0.6013**	-0.43	**0.60**
5	0.5	5.013	**0.5013**	-0.53	**0.50**
4	0.4	4.008	**0.4008**	-0.63	**0.40**
3	0.3	3.010	**0.3010**	-0.73	**0.30**
2	0.2	2.009	**0.2009**	-0.83	**0.20**
1	0.1	1.012	**0.1012**	-0.93	**0.10**

Having investigated the accuracy of the pressure controller relative to the manometer measurements. In the next step, random uncertainty in the pressure readouts was analyzed. For this, again the same setup (Fig.D.1) input voltages were varied from 10 V to 1 V. For each input voltage, 5 readings were taken for voltage readouts and calculated the standard deviation. All these values are summarized in Table.D.2. Based on the results, it could be observed that we were able to achieve the value from the pressure readout well matching with set pressure only with minimal uncertainty in pressure lying around 0.5 mbar.

Table D.2: Uncertainty in pressure values

Set voltage (V)	**Set Pressure (mbar)**	Voltage readout (V)	Pressure readout (mbar)	**Standard deviation (mbar)**
10	**1000**	10.005	1000.5	**0.230**
		10.007	1000.7	
		10.008	1000.8	
		10.006	1000.6	
		10.002	1000.2	
9	**900**	8.997	899.7	**0.503**
		8.999	899.9	
		9.006	900.6	
		9.008	900.8	
		8.998	899.8	
8	**800**	7.997	799.7	**0.518**
		7.996	799.6	
		7.998	799.8	
		8.004	800.4	
		8.008	800.8	
7	**700**	6.997	699.7	**0.453**
		6.999	699.9	
		7.003	700.3	
		7.008	700.8	
		6.998	699.8	
6	**600**	6.005	600.5	**0.336**
		6.010	601.0	
		6.013	601.3	
		6.007	600.7	
		6.012	601.2	
5	**500**	5.000	500	**0.416**
		4.997	499.7	
		5.004	500.4	
		5.008	500.8	
		5.003	500.3	
4	**400**	4.004	400.4	**0.503**
		3.999	399.9	
		3.997	399.7	
		3.998	399.8	
		4.009	400.9	
3	**300**	3.007	300.7	**0.512**
		3.009	300.9	
		3.004	300.4	
		2.997	299.7	
		2.999	299.9	
2	**200**	2.011	201.1	**0.554**
		2.010	201.0	
		1.998	199.8	
		2.003	200.3	
		2.009	200.9	
1	**100**	1.005	100.5	**0.377**
		1.002	100.2	
		1.000	100	
		1.010	101.0	
		1.004	100.4	

E

Measurement of deflections for outgassing and air leakage

Table E.1: Deflection of membranes - 2000 μm

Days	Deflection (nm)
Day-1	2072.00
Day-3	2074.30
Day-5	2066.00
Day-8	2070.40

Table E.2: Deflection of membranes - 1600 μm

Days	Deflection (nm)
Day-1	882.73
Day-3	892.06
Day-5	882.47
Day-8	891.36

Table E.3: Deflection of membranes (in nm) under atmospheric pressure - for 1400 μm

Days	Deflection (nm)
Day-1	539.13
Day-3	539.93
Day-5	539.17
Day-8	542.64

Table E.4: Deflection of membranes (in nm) under atmospheric pressure - for 1300 μm

Days	Deflection (nm)
Day-1	399.79
Day-3	402.38
Day-5	400.94
Day-8	402.94

Table E.5: Deflection of membranes (in nm) under atmospheric pressure - for 1100 μm

Days	Deflection (nm)
Day-1	208.50
Day-3	210.80
Day-5	207.80
Day-8	215.34